DROPLET IMPACT HYDRODYNAMICS ON CURVED SURFACES

Doctoral Thesis

by

GARGI KHURANA

(2016MEZ0006)

DEPARTMENT OF MECHANICAL ENGINEERING

INDIAN INSTITUTE OF TECHNOLOGY ROPAR

September, 2022

DROPLET IMPACT HYDRODYNAMICS ON CURVED SURFACES

A Thesis Submitted
In Partial Fulfillment of the Requirements
for the Degree of

DOCTOR OF PHILOSOPHY
by
GARGI KHURANA
(2016MEZ0006)

DEPARTMENT OF MECHANICAL ENGINEERING
INDIAN INSTITUTE OF TECHNOLOGY ROPAR
September, 2022

© Indian Institute of Technology Ropar — 2022

All rights reserved

DECLARATION OF ORIGINALITY

I hereby declare that the work which is being presented in the thesis entitled **Droplet Impact Hydrodynamics on Curved Surfaces** has been authored by me. It presents the result of my own independent investigation/research conducted during the time period from July, 2016 to April, 2022 under the supervision of Dr. Purbarun Dhar, Assistant Professor, IIT Kharagpur and Dr. Devranjan Samanta, Assistant Professor, IIT Ropar. To the best of my knowledge, it is an original work, both in terms of research content and narrative, and has not been submitted or accepted elsewhere, in part or in full, for the award of any degree, diploma, fellowship, associateship, or similar title of any university or institution. Further, due credit has been attributed to the relevant state-of-the-art and collaborations with appropriate citations and acknowledgements, in line with established ethical norms and practices. I also declare that any idea/data/fact/source stated in my thesis has not been fabricated / falsified/ misrepresented. All the principles of academic honesty and integrity have been followed. I fully understand that if the thesis is found to be unoriginal, fabricated, or plagiarized, the Institute reserves the right to withdraw the thesis from its archive and revoke the associated Degree conferred. Additionally, the Institute also reserves the right to appraise all concerned sections of society of the matter for their information and necessary action (if any). If accepted, I hereby consent for my thesis to be available online in the Institute's Open Access repository, inter-library loan, and the title & abstract to be made available to outside organizations.

Signature Gargi..

Name: Gargi Khurana

Entry Number: 2016MEZ0006

Program: PhD

Department: Mechanical Engineering

Indian Institute of Technology Ropar

Rupnagar, Punjab 140001

Date: 27th September 2022

CERTIFICATE

This is to certify that the thesis entitled **Droplet Impact Hydrodynamics on Curved Surfaces**, submitted by **Gargi Khurana (2016MEZ0006)** for the award of the degree of **Doctor of Philosophy** of Indian Institute of Technology Ropar, is a record of bonafide research work carried out under our guidance and supervision. To the best of my knowledge and belief, the work presented in this thesis is original and has not been submitted, either in part or full, for the award of any other degree, diploma, fellowship, associateship or similar title of any university or institution. In our opinion, the thesis has reached the standard fulfilling the requirements of the regulations relating to the Degree.

Signature of the Supervisor

Dr. Purbarun Dhar
Mechanical Engineering Department
Indian Institute of Technology Kharagpur
Kharagpur, West Bengal 721303
Date: 27th September 2022

Signature of the Supervisor

DSamanta.

Dr. Devranjan Samanta
Mechanical Engineering Department
Indian Institute of Technology Ropar
Rupnagar, Punjab 140001
Date: 27th September 2022

ACKNOWLEDGMENT

Undertaking Ph.D. has been a truly life changing experience for me and would not have possible without the support and guidance that I received from many people. Firstly, it is an honor to express my sincere gratitude towards my supervisors **Dr. Purbarun Dhar** and **Dr. Devranjan Samanta** for their patience, motivation, unconditional support and immense knowledge. They have been the back bone in molding my academic career. Their work ethics, hardwork and humble attitude would be my source of inspiration throughout my life. I thank them for providing independent research ambience, their valuable inputs and timely supports at every phase of my research career at IIT Ropar.

I warmly thank my Doctoral committee members, **Dr. Himanshu Tyagi**, **Dr. Rakesh Kumar Maurya**, **Dr. Subash Chandra Martha** and **Dr. Navin Kumar** for their valuable suggestions and encouragement throughout the course. I also express my sincere regard to **Prof. Suman Chakraborty** of IIT Kharagpur (external examiner during comprehensive seminar) for his insightful comments and encouragement that enabled me to widen my research from various perspectives. I am very much thankful to **Indian Institute of Technology Ropar** for providing necessary infrastructure and financial support. I am also grateful to **Ministry of Human Resources and Development**, Government of India, for providing scholarship to conduct this research work.

I would like to acknowledge **Mr. Nilamani Sahoo** for helping me in conducting the experiments. I am grateful to the workshop staff for supporting me in building the experimental setup. I also thank all my lab mates and friends for making this academic journey light, bright and joyful.

The present work would not have been possible without the love and unconditional support of my family. I acknowledge my parents, **Ms. Anu Khurana** and **Mr. Harish Khurana** for their sacrifices and blessings.

Gargi Khurana

LAY SUMMARY

Droplet impacting on the solid surface and its consequent wetting and spreading dynamics is an interesting physical phenomenon. This fluid dynamic process results in numerous morphological outcomes which find vital applications in improving efficiencies of droplets and spraying systems employed in agriculture and industries. The physics and mechanisms become more intriguing and insightful when the surface geometrical features and material properties provide additional constraints to droplet spreading behavior post impact. In this thesis, post-impingement morphology and dynamics of spreading of the droplet are investigated on different curved surfaces. The studies are performed experimentally followed by theoretical processing and investigation in order to understand the hydrodynamics in detail. The effects of surface dimensions, shape and thermodynamic properties are probed along with impact conditions.

The present thesis mainly focuses on the quantitative determination of the influence of these parameters on the post-impact spreading of the liquid on the target surface and the phenomenological description of the outcomes. The impingement outcomes have been quantified three dimensionally by employing the following variables, i.e., the spreading factor, the wetting fraction, non-dimensional film thickness at the pole and jet velocity. The observations suggest that the spreading and wetting perimeter increase though the liquid film thickness decrease on increasing impact Weber number and increasing target convexity. Whereas opposite trend is noted on increasing the target concavity. Interestingly, spreading along the longitudinal axis is more prominent in concave structures than convex ones, even resulting in jetting phenomenon in some cases. The reason is attributed to the gravity force which assists the extension of the impacted droplet in the transverse direction for convex surfaces whereas opposes for concave surfaces. Moreover, theoretical modelling has also been proposed for the quantification of maximum spreading and temporal evolution of liquid film thickness as well as jet velocity on different target surfaces. The experimental measurements are noted to be in good agreement with the analytically predicted values.

ABSTRACT

Droplet impact, dynamics, wetting, and spreading behavior on solid surfaces impose rich and interesting physics, in addition to extensive understanding of processed employing droplets and sprays. The physics and mechanisms become more interesting and insightful when the geometry and wettability of the surface provide additional constraints to the fluid dynamics. Post-impingement morphology and dynamics of water droplets on various curved surfaces, having dimensions comparable to that of the droplet, have been explored in the thesis. Top and side views of the impaction phenomenon have been captured using the high-speed imaging technique. The surface concavity or convexity, target-to-droplet size ratio, surface wettability and impact Weber number are systematically varied in order to note interesting outcomes. The focus of the thesis is the quantitative determination of the influence of these parameters on the post-impact spreading of the liquid on the target surface and the phenomenological description of their outcomes. The post-collision hydrodynamics have been quantified along the azimuthal and axial direction, employing various variables, namely, the spreading factor, the wetting fraction, non-dimensional film thickness at the pole and axial jetting velocity. The observations indicate that the spreading factor and the wetting fraction increase but film thickness at the pole decrease with increasing impact Weber number and increasing target convexity. Whereas opposite variations are found true for the increasing target concavity.

The observations also revel the occurrence of axial jetting hydrodynamic phenomenon in concave surfaces unlike on convex surfaces. This is because gravity force assists the extension of impacted droplet in the azimuthal direction for increasing convexity of the target whereas opposes for increasing concavity of the target. Further, analytical expressions for maximum wetting fraction, maximum spread angle, temporal evolution of liquid film thickness and jet velocity have been produced on different target geometries. The findings of the thesis may be applied in cooling, coating, spray painting and wetting of intricate structures and complexly designed engineering components.

Keywords: Droplets, droplet impact, cylindrical, spherical, grooves, hydrophilic, superhydrophobic, hydrodynamics, lamella dynamics, diameter ratio, spreading factor, film thickness, wetting fraction Weber number, Capillary number, jet

LIST OF PUBLICATIONS

List of Journal Publications from the thesis

- **Khurana, G.**, Sahoo, N., & Dhar, P. (2019). Post-collision hydrodynamics of droplets on cylindrical bodies of variant convexity and wettability. *Physics of Fluids*, *31*(2), 022008. *(Editor's Pick Article)*
- **Khurana, G.**, Sahoo, N., & Dhar, P. (2019). Phenomenology of droplet collision hydrodynamics on wetting and non-wetting spheres. *Physics of Fluids*, *31*(7), 072003.
- Agrawal, S., **Khurana, G.**, & Dhar, P. (2021). Droplet collision and jet evolution hydrodynamics in wetting modulated valley configurations. *Physics of Fluids*, *33*(4), 042008.
- **Khurana, G.**, Agrawal, S., Samanta, D., & Dhar, P. (2022). Droplet post-impact regimes on concave contours. (communicated)

List of Journal Publications outside the thesis

- Jaiswal, V., Harikrishnan, A. R., **Khurana, G.**, & Dhar, P. (2018). Ionic solubility and solutal advection governed augmented evaporation kinetics of salt solution pendant droplets. *Physics of Fluids*, *30*(1), 012113.
- Dhar, P., **Khurana, G.**, Anilakkad Raman, H., & Jaiswal, V. (2019). Superhydrophobic surface curvature dependence of internal advection dynamics within sessile droplets. *Langmuir*, *35*(6), 2326-2333.
- Sahoo, N., **Khurana, G.**, Harikrishnan, A. R., Samanta, D., & Dhar, P. (2020). Post impact droplet hydrodynamics on inclined planes of variant wettabilities. *European Journal of Mechanics-B/Fluids*, *79*, 27-37.
- Paul, A., **Khurana, G.**, & Dhar, P. (2021). Substrate concavity influenced evaporation mechanisms of sessile droplets. *Physics of Fluids*, *33*(8), 082003.

Conference Proceedings

- **Khurana, G.**, Sahoo, N., & Dhar, P. (September 2018). Droplet wetting dynamics post-impact on cylindrical bodies. *12th European Fluid Mechanics Conference* (EFMC), Vienna, Austria.
- **Khurana, G.**, & Dhar, P. (December 2018). Impact dynamics of droplets on cylindrical targets. Proceedings of the *7th International and 45th National Conference on Fluid Mechanics and Fluid Power* (FMFP), IIT Bombay, India.
- **Khurana, G.**, & Dhar, P. (September 2019). Hydrodynamics of droplet impact on concave target bodies. *4th International conference on Droplet*, Durham, United Kingdom.
- **Khurana, G.**, & Dhar, P. (December 2019). Droplet impact hydrodynamics on spherical bodies. *25th National and 3rd International Heat and Mass Transfer Conference*, IIT Roorkee, India.

CONTENTS

Chapter 1 Introduction 1

1.1 Overview 1

1.2 Wetting and Contact Angle 2

1.3 Various Outcomes of Droplet Impact on Solid Surfaces 3

1.4 Organization of Thesis 4

Chapter 2 Literature Review 7

2.1 Overview 7

2.2 Investigations on the Impact of a Droplet on a Rigid Flat Surfaces 7

2.3 Spreading and Recoil Dynamics on Superhydrophobic Surfaces 9

2.4 Phenomenology of Droplet Impact on Non-Planar Surfaces 11

2.5 Objectives of Thesis 13

Chapter 3 Post-Impact Hydrodynamics of Droplets on Cylindrical Bodies 15

3.1 Introduction 15

3.2 Materials and Methodologies 16

3.3 Results and Discussions 19

- 3.3.1 Hydrophilic Surfaces 20
- 3.3.2 Superhydrophobic Surfaces 29

3.4 Mathematical Formulation 33

3.5 Closure 41

Chapter 4 Post-Impaction Droplet Hydrodynamics on Spherical Surfaces 45

4.1 Introduction 45

4.2 Experimental Methods 45

4.3 Results and Discussions 47

  4.3.1 Hydrophilic Surfaces 48

  4.3.2 Superhydrophobic Surfaces 53

4.4 Mathematical Modelling 56

4.5 Closure 61

Chapter 5 Droplet Collision and Jet Evolution Hydrodynamics in Valley Configurations 63

5.1 Introduction 63

5.2 Experimental Techniques 63

5.3 Results and Discussions 66

  5.3.1 Hydrophilic Surfaces 67

  5.3.2 Superhydrophobic Surfaces 71

  5.3.3 Post-Impact Jetting Along the Axis of “V” Grooves 74

5.4 Closure 83

Chapter 6 Droplet Post-Impact Regimes on Curved Concave Contours 85

6.1 Introduction 85

6.2 Materials and Methodologies 85

6.3 Results and Discussions 87

- 6.3.1 Dynamics in Hydrophilic Surfaces 88
- 6.3.2 Dynamics in Superhydrophobic Surfaces 92
- 6.3.3 Post-Impact Axial Jetting Phenomenon 96

6.4 Closure 104

Chapter 7 Conclusions and Scope 107

7.1 Conclusions 107

7.2 Future Scope of the Work 109

LIST OF TABLES

Table 3.1 The liquid-gas and solid-liquid components of surface energy and static contact angle for cylindrical targets of variant wettability. 18

Table 4.1 The liquid-gas and solid-gas components of surface energy and static contact angles for spherical surfaces. 47

Table 5.1 Dimensions of the "V" grooves. 'D' represents the width and 'H' represents the depth of the groove. 65

Table 5.2 Surfaces tensions for the liquid-gas and solid-gas interfaces and static contact angle for the flat surfaces. 66

Table 6.1 Dimensions of the concave grooves. 'D' represents the width and ' H' represents the depth of the groove. 87

Table 6.2 Interfacial tensions for the liquid-gas and solid-gas interfaces and static contact angle for the flat surfaces. 88

LIST OF FIGURES

Figure 1.1 Practical applications of droplet impact. 1

Figure 1.2 Illustration of the contact angle formed by a liquid droplet resting on an ideal solid surface. 2

Figure 1.3 Different possible outcomes for droplet impacting dry solid surface. 3

Figure 2.1 Schematic representation of a droplet in the following wetting states (a) Wenzel state (b) Cassie-Baxter state 10

Figure 3.1 (A) Schematic of the experimental setup (a) Computer for data acquisition and control of the camera unit (b) High speed camera with a 105 mm macro lens assembly (c) Precision microliter droplet dispensing mechanism (d) Chromatography syringe with stainless steel needle (e) Cylindrical target body (f) Droplet dispenser unit controller (g) LED illumination unit with intensity controller. (B) SEM image of the SH coated surface. 17

Figure 3.2 Illustration of the transient (a) wetting fraction ω (b) non-dimensional liquid film thickness at the north pole h^* and (c) spreading factor γ. The letter p denotes the wetted perimeter of the cross section of the target, the letter h denotes liquid film thickness at the north pole of the target, the letter s denotes the total lateral spreading length, R_{cyl} symbolizes the radius of the target and D_d denotes the diameter of the pre-impact droplet. Three phases of spreading for droplet impact on 1.54 mm cylindrical target at 0.95 m/s ($We = 36$) are (d) inertial phase (e) viscous phase (f) gravity induced phase. 18

Figure 3.3 Post-impact deformation (front view), wetting and post-wetting lamella dynamics water droplet on hydrophilic cylindrical target surface (diameter 2.4 mm) at impact velocities of (a) 1.5 m/s, (b) 1.17 m/s, and (c) 0.95 m/s. The associated and the time frames have been illustrated. The magnitude of scale bar (bottom right) is 2.4 mm. Scale bar is same for all images. The array illustrates the role of the impact We. 21

Figure 3.4 Front view of post-impact images of droplet onto hydrophilic cylindrical target surfaces of diameters a) 1.54 mm, b) 2.4 mm, and c) 4 mm at 0.95 m/s impact velocity (impact $We = 36$). The magnitude of scale bar is equal to 2.4 mm (in bottom right image). Scale bar is same for all images. The array illustrates the role of D^*. 23

Figure 3.5 Temporal variation of wetting fraction on hydrophilic cylindrical target surfaces of different D^* at (A) $We = 36$. Inset: Front view post impact images depicting maximum wetting fraction for (a) $D^* = 0.531, \tau = 2.37$; (b) $D^* = 0.828, \tau = 2.64$; and (c) $D^* = 1.379, \tau = 3$; (B) $We = 89$. Inset: Front view post impact images depicting maximum wetting fraction for (a) $D^* = 0.531$, $\tau = 3.31$; (b) $D^* = 0.828, \tau = 3.45$; and (c) $D^* = 1.379$, $\tau = 3.45$. The magnitude of scale bar (in inset (c)) is equal to 4mm. The scale bar is the same for all the inset images. 25

Figure 3.6 Temporal variation of film thickness at the north pole of the hydrophilic cylindrical target surface of different D^* (A) We=36 (B) We=89. 27

Figure 3.7 (A) Temporal variation of spreading factor on hydrophilic cylindrical target surfaces of different D^* for $We = 36$. Inset: Front view post impact images at $\tau = 1.63$ for (a) $D^* = 0.51$ (b) $D^* = 0.828$ and (c) $D^* = 1.379$. (B) Temporal variation of spreading factor on hydrophilic cylindrical target surface (diameter 2.4mm) at different impact We. Inset: Front view post impact images at $\tau = 3.9$ at impact We (a) 36 (b) 54 and (c) 89. The magnitude of scale bar is equal to 2.4 mm. The scale bar is same for all images. 28

Figure 3.8 Comparison of front view post impact images of droplet onto cylindrical target of different wettability having target diameter 4 mm at 1.5 m/s impact velocity ($We = 89$): (a) SH surface (b) Hydrophilic surface. Comparison of impact for target diameter 2.4mm at 0.95m/s impact velocity ($We = 36$): (c) SH surface (d) Hydrophilic surface. The magnitude of scale bar is equal to 4mm (bottom right). The scale bar is same for all images. 30

Figure 3.9 Top view images taken at different times for the impact of a water droplet at 1.5 m/s ($We = 89$) onto a 4 mm diameter cylindrical target of different wettability (a) hydrophilic surface (b) SH surface. The magnitude of scale bar is equal to 4 mm. The scale bar is same for all images. 31

Figure 3.10 Temporal variations of (a) wetting fraction (b) spreading factor (c) non-dimensional film thickness at the north pole of the cylindrical target for different wettability. Comparison of top view post impact images for target diameter 1.54 mm and 1.17 m/s impact velocity ($We = 54$) for (d) Hydrophilic surface (e) SH surface. The magnitude of scale bar is equal to 1.54 mm. The scale bar is same for all images. 32

Figure 3.11 Analytical description of the film flow on the cylindrical target during evolution of the film. The similarity of the simplified geometry considered can be observed from figure 3.3, $We = 36$, 3.06 ms, and figure 3.9 (a), 2.78 ms. 34

Figure 3.12 Comparison of experimental (Ex) and theoretical (Th) film thickness evolution of water droplets at the north pole for (a) $We = 36$ on hydrophilic surface, (b) $We = 89$ on hydrophilic surface, (c) $We = 36$ on a SH surface, and (d) $We = 89$ on a SH surface. 38

Figure 3.13 Comparison of experimental (Expt) and theoretical (Theo) values of $2\theta_{max}$ for various impact conditions on Hydrophillic and Superhydrophobic cylindrical targets. 42

Figure 4.1 (A) Schematic of the experimental setup (a) computer for data acquisition and camera control (b) high speed camera with a 105 mm macro lens (c) digitized microliter droplet dispenser (d) microliter syringe with stainless steel needle (e) spherical body (f) droplet dispenser and backlight illumination controller (g) LED backlight (B) SEM image of the coated SH coated. 46

Figure 4.2 Postcollision morphology of droplets on hydrophilic sphere (diameter 2.4 mm) at impact velocities of (a) 0.94 m/s, (b) 1.17 m/s and (c) 1.5 m/s. The associated We and the time frames are mentioned. The scale bar (bottom right) represents 2.4 mm. Scale bar is same for all images. The array illustrates the role of the impact We. 48

Figure 4.3 Postimpact deformation of droplet impacted at 0.94 m/s velocity (impact $We = 36$) on hydrophilic spheres of diameters (a) 4.7 mm (b) 3.2 mm and (c) 2.4 mm. The associated D^* and the time frames are mentioned. The scale bar is equal to 2.4 mm (in bottom 49 right). Scale bar is same for all images. The array illustrates the role of D^*.

Figure 4.4 Postcollision behavior of droplets on different large hydrophilic spheres at different impact velocities (a) target diameter = 9.5 mm, impact velocity = 0.94 m/s; (b) target diameter = 9.5 mm, impact velocity = 1.17 m/s; (c) target diameter = 6.95 mm, impact velocity = 0.94 m/s; (d) target diameter = 6.95 mm, impact velocity = 1.17 m/s. The associated D^*, impact We and the time frames are mentioned. The scale bar is of 6.95 mm. 50

Figure 4.5 (A) Temporal variation of the spreading factor on hydrophilic spheres of different D^* at 0.94 m/s impact velocity ($We = 36$). Inset: Postimpact images at $\tau = 1.98$ for (a) $D^* = 2.48$ (b) $D^* = 1.68$ and (c) $D^* = 0.86$. The magnitude of scale bar is 6.95 mm, 4.7 mm and 2.4 mm, respectively for (a)-(c). (B) Temporal variation of the spreading on spheres of hydrophilic and superhydrophobic surfaces at 0.94 m/s impact velocity ($We = 36$). Inset: Postimpact images at $\tau = 1.603$ for 2.4 mm diameter sphere with (a) hydrophilic and (b) superhydrophobic surface. The magnitude of scale bar is 2.4 mm. The uncertainties associated are within ∓7%. 51

Figure 4.6 Comparison of the experimental data with proposed analytical model for temporal variation of h^* on hydrophilic spheres under the following conditions (A) $D^* = 0.86, We = 34$ and $D^* = 1.143, We = 34$; (B) $D^* = 0.86, We = 34$ and $D^* = 0.86, We = 88$; (C) $D^* = 1.68, We = 34$ and $D^* = 2.48$, $We = 34$; and (D) $D^* = 2.48, We = 34$ and $D^* = 2.48$, $We = 88$. The inset shows the liquid film morphology at $\tau = 1.42$ on hydrophilic sphere of $D^* = 0.86$. 52

Figure 4.7 Postcollision deformation (front view) on SH spheres (2.4 mm) at impact velocities (a) 0.94 m/s, (b) 1.17 m/s and (c) 1.5 m/s. The We and time frames have been mentioned. The scale bar (bottom right) is of 2.4 mm. The array illustrates the role of the We. 54

Figure 4.8 Top view postimpact images for impact velocity 1.17 m/s ($We = 52$) on 4.7 mm diameter spheres with (a) hydrophilic surface (b) SH surface. The scale bar is equal to 4.7 mm. 54

Figure 4.9 Comparison of the experimental data with available analytical model for variation of h^* on spherical targets under the following conditions (A) $D^* = 0.86$, $We = 34$ (SH surface) and $D^* = 1.143$, $We = 34$ (SH surface); (B) $D^* = 0.86$, $We = 34$ (SH surface) and $D^* = 0.86$, $We = 88$ (SH surface); (C) $D^* = 1.68$, $We = 34$ (SH surface) and $D^* = 2.48$, $We = 34$ (SH surface); (D) $D^* = 2.48$, $We = 52$ (SH surface) and $D^* = 2.48$, $We = 52$ (Hydrophilic surface). 55

Figure 4.10 (a) Schematic depicting maximum spread angle ($2\theta_{outer}$ and $2\theta_{inner}$) for big and small spheres. (b) and (c) are the side and top view images for hydrophilic spheres ($D^* = 1.68$) at maximum spread ($We = 34$). (d) and (e) are same for $D^* = 0.86$ ($We = 34$). The magnitude of scale bar is 4.7 mm. 57

Figure 4.11 Comparison of experimental and theoretical values of maximum spread angle for various impact conditions on hydrophilic and SH (a) big spheres (b) small spheres 62

Figure 5.1 (A) Schematic of the experimental setup (a) data acquisition computer system, showing the front view of a typical "V" groove with droplet impact (b) high speed camera (c) precision droplet dispenser (d) chromatography glass micro-syringe with a stainless-steel needle (e) substrate ("V" groove or valley configuration) (f) backlight illumination source (g) droplet dispensing and backlight illuminating system controller. (B) Illustration of transient spreading parameters used in the analyses (white region represents the liquid droplet): (a) spreading width (b) south-pole height (c) wetting perimeter along the groove walls. 64

Figure 5.2 Temporal evolution of the post-impact droplet (front view) on the "V" groove with D^* = 0.8 and H^* = 0.4 for three different We, (a) We = 30, (b) = 50, and (c) = 80. Scale bar shown in the top right corner represents 1.85 mm and is same for all the images. The red line indicates the shape of the groove. 67

Figure 5.3 Temporal evolution of the post-impact droplet (front view) for We = 30 on grooves with fixed D^* = 1.6 and three different H^*, (a) H^* = 0.4, (b) H^* = 0.6, and (c) H^* = 0.8. The scale bar shown in the top right corner represents 1.7 mm length and is same for all the images. 68

Figure 5.4 Temporal evolution of the post-impact droplet (front view) for $We = 30$ on grooves with fixed H^* = 0.4, and three different D^*, (a) D^* = 0.8, (b) D^* = 1.6, and (c) D^* = 2.4. The scale bar shown in the top right corner represents 1.85 mm length and is same for all the images. 69

Figure 5.5 Variation of (a) non-dimensional south-pole height (h^*) and (b) non-dimensional spreading width (γ) with non-dimensional time (τ) for different grooves and impact We for same hydrophilic substrates. 70

Figure 5.6 Temporal evolution of the post-impact droplet (front view) on a groove (D^{*} = 0.8 and H^{*} = 0.4) for two different combinations of impact We and wettability. (a) We =30; hydrophilic (HP) surface (b) We = 30; SHS (c) We = 80; HP surface (d) We = 80; SHS. The scale bar at the top right corner represents 1.85 mm and is same for all the images. 72

Figure 5.7 Variation of the non-dimensional height of post-impact droplet at the north-pole with the non-dimensional time on the both HP and SH grooves with dimensions (a) D^{*} = 1.6; H^{*} = 0.4 (b) D^{*} = 2.4; H^{*} = 0.8. 73

Figure 5.8 Variation of the non-dimensional spreading width of the post-impact droplet with the non-dimensional time on both HP and SHS grooves with dimensions (a) D^{*} = 1.6; H^{*} = 0.4 (b) D^{*} = 2.4; H^{*} = 0.8. 74

Figure 5.9 Evolution of the jet flow from the post-impact droplet (top view) along the groove (D^{*} = 2.4 and H^{*} = 0.8) at two different We and wettability. (a) We = 30; HP surface (b) We = 30; SH surface (c) We = 80; HP surface (d) We = 80; SH surface. The scale bar shown in the top right corner represents 3.24 mm length and is same for all the images. The yellow thin lines indicate the position of the tip of the evolving jet. 75

Figure 5.10 Variation of the velocity of the tip of the jet with the non-dimensional time for two different impact We on the both HP and SHS grooves with dimensions (a) D^{*} = 1.6; H^{*} = 0.4 (b) D^{*} = 2.4; H^{*} = 0.8. 76

Figure 5.11 Schematic (front view and top view) of the post-impact droplet during jetting phase. The characteristic and geometric parameters considered in the model have been illustrated with proper labels. The dashed-dotted line represents the line of symmetry for the jetting behavior. 79

Figure 5.12 Comparison of the experimental (*Ex*) jet velocity against the theoretical (*Th*) predictions for different combinations of the “V” groove and wettability, for (a) D^*=1.6; H^*=0.4; HP (b) D^*=2.4; H^*=0.8; HP (c) D^*=1.6; H^*=0.4; SH (d) D^*=2.4; H^*=0.8; SH. 82

Figure 6.1 (A) Schematic of the experimental setup (a) data acquisition computer system, showing the front view just before the impact of the droplet on the substrate (b) high speed camera (c) precision droplet dispenser mechanism (d) chromatography glass micro-syringe with a stainless-steel needle (e) substrate (concave groove) (f) backlight illumination source (g) droplet dispensing and backlight illuminating system controller. (B) Illustration of transient spreading parameters and representative of the target surface (concave groove): (i) spreading width, *s* (ii) south-pole film thickness, *h* (iii) jet velocity, V_{jet} (iv) schematic representing groove dimensions. 86

Figure 6.2 Temporal evolution of the post-impact droplet (front view) on the concave grooves having dimensions $D^* = 2.14$ and $H^* = 1.07$, for three different We: (a) $We = 33$ (b) $We = 51$ and (c) $We = 83$. The scale bar shown in the top right corner represents 3 mm and is same for all the images. The red curve indicates the profile of the groove. 89

Figure 6.3 Temporal evolution of the post-impact droplet (front view) for *We* = 33 on concave grooves with fixed $D^* = 2.14$ and three 90 different H^*: (a) H^* = 1.07 (b) = 0.71 and (c) = 0.43. The scale bar shown in the top right corner represents 3 mm length and is same for all the images.

Figure 6.4 Temporal evolution of the post-impact droplet (front view) for *We* = 33 on concave grooves with fixed $H^* = 0.71$, and three different D^*: (a) D^* = 0.89, (b) = 1.57 and (c) = 2.14. The scale bar shown in the top right corner represents 3mm length and is same for all the images. 90

Figure 6.5 Temporal variations of (a) and (c) non-dimensional south-pole film thickness (h^*) and (b) and (d) non-dimensional spreading width (γ), for different hydrophilic grooves at different impact We. 91

Figure 6.6 Temporal evolution of the post-impact droplet (front view) on a concave groove (D^* = = 2.14 and H^* = = 1.07) for two different combinations of impact We and wettability. (a) We = 33, hydrophilic surface (HP) (b) We = 33, superhydrophobic surface SHS (c) We = 83, HP surface (d) We = 83, SHS. The scale bar at the top right corner represents 3mm and is same for all the images . 93

Figure 6.7 Temporal variation of the non-dimensional south-pole film thickness of post-impact droplet on both hydrophilic (HP) and superhydrophobic (SH) concave grooves with dimensions (a) D^* = 2.14, H^* = 1.07 (b) D^* = 1.57, H^* = 0.71 (c) D^* = 2.14, H^* = 0.71. 94

Figure 6.8 Temporal variation of the non-dimensional spreading width of post-impact droplet on both hydrophilic (HP) and superhydrophobic (SH) concave grooves with dimensions (a) D^* = 2.14; H^* = 1.07 (b) D^* = 1.57; H^* = 0.71 (c) D^* = 2.14; H^* = 0.71. 95

Figure 6.9 Top view images taken at different time instants for the impact of a water droplet onto a concave groove (D^* = 2.14 and H^* = 1.07) for two different combinations of impact We and wettability. (a) We = 33, hydrophilic (HP) surface (b) We = 33, SHS (c) We = 83, HP surface (d) We = 83, SHS. The scale bar at the top right corner represents 3 mm and is same for all the images. The yellow lines indicate the tip of the axial jet. 96

Figure 6.10 Top view images taken at different time instants for the impact of a water droplet on concave grooves with fixed D^* = 2.14 and three different H^*: (a) H^* = 1.07 (b) = 0.71 and (c) = 0.43. The scale bar shown represents 3 mm length and is same for all the images. The yellow lines indicate the tip of the axial jet. 97

Figure 6.11 Top view images taken at different time instants for the impact of a water droplet on concave grooves with fixed H^* = 0.71, and three different D^*: (a) D^* = 0.89, (b) = 1.57 and (c) = 2.14. The scale bar shown in the bottom right corner represents 3mm length and is same for all the images. The yellow lines indicate the tip of the axial jet. 98

Figure 6.12 Temporal variation of the jet velocity for two different impacts We on the both HP and SHS concave grooves with dimensions (a) D^* = 2.14, H^* = 1.07 (b) D^* = 1.57, H^* = 0.71 (c) D^* = 2.14, H^* = 0.71. 99

Figure 6.13 Schematic (front view and top view) of the post-impact droplet during the jetting phase. The characteristic and geometric parameters considered in the model have been illustrated with proper labels. The dashed-dotted line represents the line of symmetry. 100

Figure 6.14 Comparison of the experimental (*Ex*) jet velocity against the theoretical (*Th*) predictions for different combinations of the concave grooves and wettability, for (a) $D^{*} = 2.14$, $H^{*} = 1.07$, HP (b) $D^{*} = 2.14$, $H^{*} =1.07$, SHS (c) $D^{*} = 1.57$, $H^{*} = 0.71$, HP (d) $D^{*} = 1.57$, $H^{*} = 0.71$, SHS (e) $D^{*} = 2.14$, $H^{*} = 0.71$, HP (f) $D^{*} = 2.14$, $H^{*} = 0.71$, SHS. 106

Chapter 1

Introduction

1.1 Overview

Droplet impact on solid surfaces has been an area of interest for researchers since a very long time. It is of fundamental and practical importance. Droplet impact is relevant in nature and in the industry. In nature, droplet impacts cause soil erosion, hollows stone surfaces, cause landslide and brings the smell of earth during rain. In industry, droplet impact plays an increasing role in inkjet printing, in fabrication of microelectronics using soldering, cleaning, coating and cooling of engineering components [1-7]. It is noteworthy to understand the spreading dynamics of impacted droplets in designing and modelling of fire extinguishing, anti-icing, fuel injectors and pesticide spraying systems for better and efficient results [8-16].

Fire suppression sprinkler
De-icing system
Spay painting
Spay cooling
Inkjet printing
Pesticide spraying
pump
piezo element
ink
nozzle
charge electrode
image signal
deflector
ink droplet
recycling gutter
paper

Figure 1.1 Practical applications of droplet impact.

1.2 Wetting and Contact Angle

Wetting is the ability of a liquid to remain in contact with a solid surface, resulting from intermolecular forces when the two are brought together. When a liquid droplet is placed on an ideally smooth horizontal surface, in equilibrium position it forms a cap structure as shown in the figure 1.2. This resulting shape is bounded by interfacial or surface forces, to attain the minimum surface energy state. The angle formed between the solid-liquid interface and liquid-gas interface is termed as the contact angle. When the contact angle is small, the liquid spreads on the surface, and when the contact is large, the liquid beads up on the surface. For hydrophilic and hydrophobic surfaces, the contact angle is specifically less and more than 90 degrees respectively. In case contact angle is more than 150 degrees, the surfaces are considered to be superhydrophobic surfaces [17-19]. In 1805, Sir Thomas Young described that the contact angle of an ideal surface i.e., flat, homogeneous, isotropic and rigid by the famous Young's equation:

$$\cos \theta_Y = \frac{\sigma_{sg} - \sigma_{sl}}{\sigma_{lg}} \tag{1.1}$$

where σ_{sg}, σ_{sl} and σ_{lg} represent the solid-gas, solid-liquid and liquid-gas interfacial tensions respectively, and θ_Y is Young's contact angle [20-22].

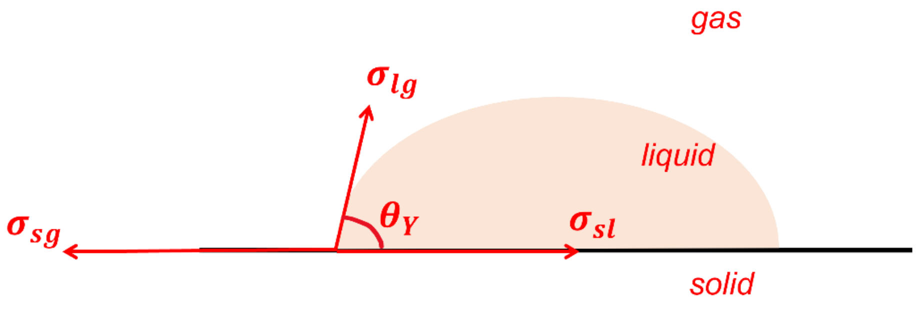

Figure 1.2 Illustration of the contact angle formed by a liquid droplet resting on an ideal solid surface.

The Young's equation is applicable for ideal surfaces, whereas in reality the surfaces are rough and heterogenous. Therefore, many metastable states of a droplet on a real solid surface exist and the measured contact angles are sometimes not equal to θ_Y [23]. In fact, wetting phenomenon is not just a static state. Therefore, a fixed value of static contact angle is not adequate for real surfaces. During the movement of the three-phase contact line, the contact angle formed is termed as dynamic contact angle. The contact angles formed by increasing and decreasing the liquid are termed as the advancing θ_a and receding contact angles θ_r. The difference between the advancing and receding contact angles is called the contact angle hysteresis. The heterogeneity and roughness of the real surfaces creates barriers for the liquid motion resulting in hysteresis, making the Young's equation misleading. However, experimental advancing contact angle is expected to be a better approximation in such cases [24-27].

1.3 Various Outcomes of Droplet Impact on a Solid Surface

When a drop of liquid strikes a dry solid surface, a variety of outcomes are possible. A large number of experiments are performed by scientists to study the morphological outcomes using high-speed digital photography [28-30]. The outcome of droplet hitting a surface is governed by numerous factors, namely, liquid properties, surface properties, droplet size, surface geometry, surrounding medium and impact velocity [31,32]. Post-impact, the droplet can either deposit, splash or bounce (see figure 1.3). Deposition and bouncing crucially depends on the wettability of the surface. Splashing arises from the radial separation of tiny droplets from the thin liquid sheet [1].

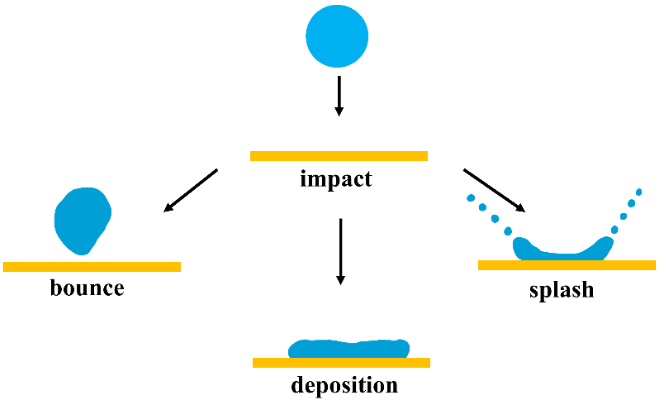

Figure 1.3 Different possible outcomes for droplet impacting dry solid surface.

Further, the temporal evolution of the liquid droplet post impact has been studied by Rioboo et al. [28]. The investigation suggests that, on plotting the spreading curve for the impaction process, four phases are clearly visible. The first stage called the kinematic phase, in which contact diameter grows according to the power law in time. Wettability of the substrate is not influential in this early phase. Only impact velocity and initial diameter play an important role in this stage.

The next comes the spreading phase where other liquid and surface properties play a role in the evolution. Maximum spreading is achieved by the end of this phase. The spreading phase is followed by the relaxation phase, which may have different outcomes, depending on the receding contact angle value. Finally in the equilibrium phase, the lamella attains a constant diameter or for highly wetting surfaces, continues to increase steadily.

In recent times, there is a significant focus on development of superhydrophobic surfaces by combining hydrophobicity with surface roughness [33,34]. Superhydrophobic surfaces consists of nanoscale pillars on microscale domes resulting in hierarchically double-scale structures. Due to development in nanoscale fabrication technology, generating a surface with tailored wettability is possible. Droplet impinging on the superhydrophobic surfaces has applications in self-cleaning, ice resisting and corrosion protection surfaces. Therefore, probing the underlying physics of droplet impact on such surfaces is useful [35-38].

1.4 Organization of Thesis

- Chapter 1 gives an introductory overview about the field of droplet impact and its applications. Wetting and contact angle are briefly explained followed by the discussion on different possible outcomes of droplet colliding a solid surface.
- Chapter 2 presents a comprehensive review of the relevant studies available in literature. Further, gaps in previous studies have been identified and the main objectives of the thesis have been formed.

- Chapter 3 presents an experimental and theoretical investigatory study on hydrodynamics of a single droplet impact on cylindrical surface. Various paraments like impact velocity, cylindrical surface dimensions and wettability are varied. The chapter also includes two theoretical models for better understanding.
- Chapter 4 describes the comprehensive experimental and the subsequent theoretical investigation of post-impaction hydrodynamics of droplet impingement on spherical target surfaces. The size of the spherical surfaces considered range from smaller to larger than the droplet size. Moreover, the wettability and impact conditions have also been varied and their impact studied in detail.
- Chapter 5 elaborates post-impaction hydrodynamics of droplet on concave "V" shaped surfaces. The asymmetric groove geometry makes the hydrodynamics three-dimensional. An interesting phenomenon of axial jetting is introduced. This chapter also presents the temporal variation of various morphological parameters namely, spreading width, south-pole film thickness and jet velocity. A semi-analytical model to predict the jet velocity evolution has also been proposed.
- Chapter 6 illustrates the post-impingement morphology and dynamics of droplets on concave curved surfaces. The chapter elaborates the transient spreading behaviour of droplet on substrates of varied dimensions and wettability in detail. Lastly, a theoretical formalism for temporal evolution of axial jet velocity for such target surface has also been derived.
- Chapter 7 summarizes the conclusions of the entire thesis report. Further possible scope for future studies have also been suggested.

Chapter 2

Literature Review

2.1 Overview

Droplet impact dynamics has been studied extensively by many researchers for its intrinsic beauty, scientific curiosity and variety of applications. The important role played by the dynamic droplet-substrate interaction in many natural, industrial and agricultural processes has ignited experimental and theoretical research all over the world. The field of droplet impact hydrodynamics is a fluid dynamics phenomenon of a single droplet striking a surface and its consequent behaviour. Droplet impingement and the resulting fluid flow on the solid surface is a complex process which involves three components: the solid surface, the liquid and the surrounding vapour [39,40]. The complexity of the phenomenon increases due to the fact that it is a nonlinear dynamical process [41-43]. Therefore, it is no surprise that the outcome of this hydrodynamic interaction is diverse and interesting. It depends on the combined effect of the droplet size, liquid properties, surface properties, target surface geometry and impact conditions [41,44-47]. This chapter presents a critical review of the earlier studies available in the area of droplet impacts on solid surfaces. Important studies defining the basics of droplet collisions have been investigated thoroughly. Further, based on the literature survey, the main objectives of the thesis have been formed and presented.

2.2 Investigations on the Impact of a Droplet on a Rigid Flat Surface

In 1876, Worthington reported the pioneering systematic study in the area of droplet impacts on solid surfaces [47]. However, despite more than a century of research, the rapid dynamics of this intriguing phenomenon could not be unravelled until the recent development of high-speed high-resolution video technology [1]. The fundamental understanding of droplet impingement process is important in a variety of applications, such as inkjet printing, rapid spray cooling, crop pesticide spraying, fire suppression sprinkling, fuel injecting system and solder-drop dispensing unit [2-5,48-51]. Most research works available in the field of droplet impact focus on flat surfaces. Several comprehensive reviews by Yarin [39], Rein [41] and Josserand [1] discuss the hydrodynamics, wetting and spreading regimes on flat surfaces of variant wettability or surface morphologies, such as roughness or texture. The main non-dimensional numbers involved in the post-impact droplet dynamics are Weber number, Reynolds number and Capillary number [1]. The experiments conducted by Rioboo et al. revealed six different outcomes of droplet impact on a dry flat surface namely, deposition, prompt slash, corona splash, receding break-up, partial rebound, complete rebound [28].

Experimental and theoretical reports by reported investigations on maximum spreading diameter, temporal evolution of spreading and recoil dynamics [52,53]. Most of the analytical models developed were focussed on energy conservation principle to predict the maximum spreading factor along the surface [54-59]. Others used dynamic contact angle and its temporal variations to estimate the spreading correctly [60,61]. Mao et al. additionally predicted the tendency of the droplet to rebound as a function of maximum spread and static contact angle [62]. Another parameter besides the spreading factor considered is the spreading time [63-65]. Wang et al. [66] and Lin et al. [67] conducted experiments on horizontal flat surfaces and estimated spreading time using universal scaling law. In an interesting study by Latka et al. [68], drop splashing at high capillary numbers was found to be independent of liquid-surface combinations. Riboux and Gordillo derived an expression of the splash threshold velocity of a droplet impinging on a smooth dry surface as function of droplet size, properties of the two fluids involved and the mean free path of the molecules of the surrounding gas medium [69].

Murshed and Nieto de Castro [70] presented a report on the spreading characteristics of nanofluid droplets impinging a solid substrate. The outcomes suggested that on increasing the volume fraction of nanoparticles in the droplet, larger spreading diameters are noted. The reason was attributed to the better in-layer structuring for higher volume-fractioned nanofluid which promotes the spreading of droplet on the surface. On similar lines, droplet impact phenomenology during Leidenfrost effect have been experimentally studied to understand the effect of vapour cushioning on the droplet impact behaviour. Different regimes and outcomes, such as explosive boiling, hovering, levitation and trampolining, vertical jetting, etc. were reported [71,72]. Coalescence process of conducting polymer droplets on a solid substrate have also been examined in reports. The findings suggest that the equilibrium spreading length of the coalesced droplets decreases with the solution concentration and spacing of the droplets. It was also found that hydrophilicity of the substrate affects the maximum spreading length but it has no influence on the equilibrium droplet diameter after coalescence [73].

2.3 Spreading and Recoil Dynamics on Superhydrophobic Surfaces

Recently, a new functional surface has attracted the attention of scientists and researchers. These high energy surfaces observe static contact angles more than 150 degrees [74]. Due to their water repellent nature, they are termed as superhydrophobic surfaces. Superhydrophobic or non-wetting surfaces find application in many fields, such as water management in fuel cells, in icing mitigation and in corrosion resistant surfaces [75-79].

The spreading dynamics has been observed and modelled by various researchers in an attempt to interpret the collisional deformation of the droplet on these types of surfaces [38]. Wenzel and Cassie-Baxter state of models were introduced to elucidate the state of water on solid surfaces (see fig. 2.1) [80,81]. In the Cassie-Baxter state, the droplet simply sits on the top of the structured surface acquiring a nearly spherical shape whereas in the Wenzel state, the droplet sinks in the microstructures and conform to the solid surface. Larger contact angles and easily rolling shapes of droplets are associated with the Cassie-Baxter model.

Structured superhydrophobic surfaces have been reported to increase the mobility of droplets by reducing the contact angle hysteresis and promoting shear free vapour-liquid interface over which liquid just slips [82-84]. Due to the vapour pockets formed at the solid-liquid interface, the outcome of droplet impact on such surfaces is a rebound (partial or complete) or shattering of the fluid film depending on the solid-liquid combination and impact conditions [85,86]. Rebound characteristics depend on the extent of energy dissipation during impaction and wetting transition within the structure. It has been observed with the increase in the impact velocity, kinetic energy spent on the droplet deformation increases therefore leaving less energy for bouncing. Therefore, for higher weber number partial rebounds and receding film breakups are prominent [87].

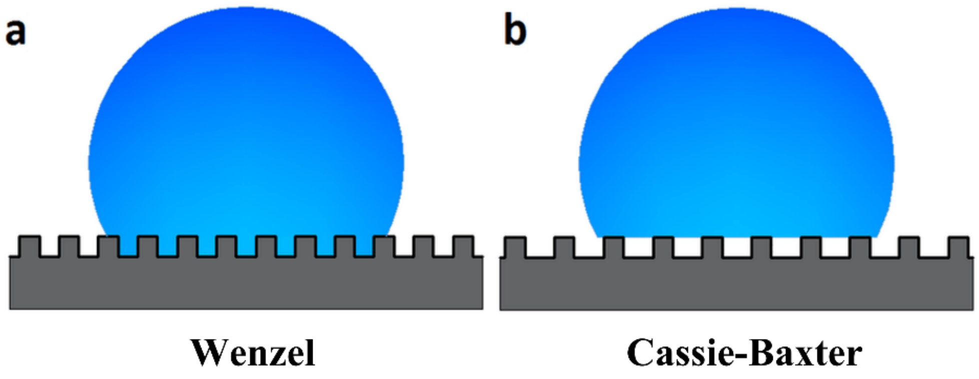

Figure 2.1 Schematic representation of a droplet in the following wetting states (a) Wenzel state [80] (b) Cassie-Baxter state [81]

In an experimental study by Richard and Quere [88], water droplets were observed to fully bounce like a balloon and thereafter oscillate on colliding with a superhydrophobic substrate. The study suggested that for solid substrates having contact angle close to 180 degrees, the kinetic energy of the impinging droplet gets converted to the surface energy without spreading. Yun [89] reported an experimental study providing insight into the shape-dependant dynamics of droplets on similar surfaces. He discovered that the contact time and the maximum bounce height reduce by at least 30% and 60%, respectively on replacing the spherical droplet by an elliptical one. The significance of wetting pressures in droplet impact and spreading phase on structured superhydrophobic surfaces have been critically examined through simulations by Murugadoss et al. [90]. Further, Chen and Lian [91] numerically studied the phenomenon of coalescence induced self-propelled droplet on similar substrates.

Sahoo et al. [92] carried out an investigation to elucidate the roles of surface wettability and inclination on the post-impact dynamics of droplets. They found that the maximum spreading diameter and spreading time decrease with increasing inclination and normal Weber number in case of superhydrophobic substrates whereas opposite was noted for hydrophilic substrates.

2.4 Phenomenology of Droplet Impact on Non-Planar Surfaces

Droplet hydrodynamics on solids having non-planar structures have started to garner interest momentum among researchers recently. Surface having complex and intricate geometries are more likely to be encountered in manufacturing of precision utilities useful in fields of science, technology and agriculture as compared to flat surfaces. Therefore, such non-planar complex geometrical surfaces may have to undergo one or many operations comprising of spray coating, cooling and painting in order to be prepared for its desired operation. [2-5,10-12,93]

A few experimental and theoretical works are present in the field of droplet impact onto spherical target surfaces. Hardalupas et al. [94] performed an experimental study of liquid (ethanol and glycerol solutions in water) droplet impact onto small solid spheres having diameter ratios (target to droplet diameter) in the range of ~3.47–8.12, at high impact velocities. The study reported formation of finger like or inverted crown shaped structures upon impact, which subsequently disrupt due to capillarity. The study also concluded that the onset of splashing is favored by an increase in surface curvature.

Next, Bakshi et al. [95] reported the spatial and temporal variation of the film thickness on spherical target surfaces for liquid (water and isopropanol) droplet impact at low velocities. The diameter ratios considered in the study ranged from ~0.68 to 8.8. The experimental results indicated three temporal phases of the film dynamics, namely, the initial drop deformation phase, the inertia dominated spreading phase, and the viscosity dominated phase. The effect of the impact Reynolds number and diameter ratio was studied, and it was found that in the first two stages, the non-dimensional temporal variation of film thickness for different values of Reynolds number collapses onto a single master curve, indicating independent behavior from the Reynolds number at lower impact velocity regimes. Additionally, the transition to the third phase is observed to occur earlier for lower Reynolds number conditions. An analytical expression for film thickness at the north pole of the target surface has also been proposed for the inertia dominated phase. Further next, Mitra et al. [96] reported a theoretical and experimental study of subcooled droplet of three different liquids, impacting on spherical brass targets in the temperature range of 20–250 degrees Celsius. Droplet spread factor was investigated over a range of Weber numbers, and the maximum spread was found to be in agreement with the Chandra and Avedisian [60] model. The study reported wetting contact for surfaces at room temperature, whereas at elevated temperature regimes, wetting is arrested due to the formation of a thin vapor cushion at the interface of surface and liquid (the Leidenfrost effect). Additionally, the droplet contact time was found to decrease with an increase in the impact Weber number.

Banitabaei and Amirfazli [97] studied the effect of impact velocity and wettability of the particle on the morphology of droplet impacting on to small spherical particles (diameter ratio more than 1). The study included the temporal variation of various post-impact geometrical parameters, viz. the film thickness, and lamella height and lamella base diameter. It was found that the lamella formation is only possible when a droplet impacts on a hydrophobic particle of some appropriate diameter ratio and impact velocity. Further next, numerical and theoretical modelling of droplet impact on spherical body was performed by Dalgamoni and Yong [98] through axisymmetric lattice Boltzmann method (LBM). It was noted that the maximum spread factor increased with a reduction in surface wettability whereas it remained almost unaffected with the change in target-to-droplet size ratio. Although, the receding phase of the droplet dynamics showed remarkable distinction on altering both surface wettability and size ratios. They interestingly showed that rebound can be observed for droplet impacts on hydrophilic targets if impact Weber is large enough.

Hung and Yao [99] experimentally investigated impact of micrometer sized water droplets on cylindrical wires. Disintegration and dripping were reported as the outcome by parametrically varying wire size and impact velocity. It was found that higher impact velocity and smaller wire size favors disintegration mode. Dripping was further classified into momentum induced and gravity induced modes. Sher et al. [100] studied the factors that affect the amount of liquid trapped upon a dry horizontal wire. A non-dimensional criterion for critical eccentricity value at which mass of liquid trapped is maximum, was reported. Jin et al. [101] noted that the radius of the cylindrical surface had more influence on the maximum spreading diameter in the azimuthal direction than in the axial direction. Liu et al. [102] adopted the coupled level set and volume-of-fluid (VOF) method to simulate impact process on tubular geometries for different hydrophobicity and impact velocities. It was found that with increasing contact angle, the spreading diameter decreases while the height of the liquid film at the center increases. Hydrodynamics of droplets upon impact has also been simulated using the lattice Boltzmann method, and four stages, namely, moving, spreading, nucleating, and dripping, were reported for curved surfaces.

In another motivating experimental research by Lorenceau and Quere [103], behaviour of a drop deposited on a conical fibre was examined. It was shown that for wetting liquids such a droplet shifts towards the lower curvature region. The driving force was found to be a gradient of Laplace pressure. Rajesh et al. [104] presented the dynamics of single droplet impact on curved superheated surfaces. They performed experiments to elucidate the effect a superheated asymmetric curvature on the collision dynamics. Milli-metric water droplets were impacted on superheated cylindrical convex and concave surfaces. It was inferred that the maximum spread factor and residence time of the impacted droplet were affected significantly by the convex and concave substrate profile and impact Weber number whereas surface superheat had negligible effect. Similar set of experiments of non-Newtonian droplet impact on cylindrical targets revealed that the gravity and shear induced drainage may interplay with the local rheology. This gives rise to regimes such as long-lasting filament formation, pearling instability, and formation of beads-on-a string structures, etc. from the draining lamella [105].

2.5 Objectives of Thesis

From the literature survey, it has been deduced that the impact hydrodynamics on non-planar surface features would be rich in its physics. Additionally, it also has important applications in pesticide spraying and coating of complex geometry objects, turbine blades, microscale machine components, and automotive parts. Therefore, studying the spreading mechanisms on non-planar target surfaces of different wettability, curvature and sizes would be relevant for academic as well as industrial purpose. The droplet post-impact regimes on such geometries are expected to be interesting and non-trivial under different impact conditions. Therefore, the specific thesis objectives have been formulated as follows:

2.5 Objective of Thesis

1. To investigate the post-collision hydrodynamics of droplets on cylindrical target surfaces of variant wettability and convexity.
2. To interpret the post-impact droplet spreading characteristics and resulting lamella formation on wetting and non-wetting spherical target bodies.
3. To understand droplet collision spreading and jet evolution hydrodynamics in valley configurations of variant wettability.
4. To study post impact phenomenology of droplet on concave contoured surfaces of variant dimensions and wettability.

Chapter 3

Post-Impact Hydrodynamics of Droplets on Cylindrical Bodies

3.1 Introduction

Post-impact hydrodynamics of droplets on cylindrical shaped bodies have applications in quenching of hot metal bars and rolls by spray cooling, de-icing of aircrafts by chemical formula spraying, applying thin corrosion resistant coating on automobile parts and in producing objects by additive manufacturing [106-108]. A few studies are found in literature discussing the outcomes of droplet impact on cylindrical shaped objects having convex profile. In 1998, Hung and Yao [99] presented the pioneering work in the field of impaction of water droplets on thin cylindrical wires. This experimental study broadly revealed two typical modes of impaction outcomes namely, disintegration and dripping. The study also examined the effects of droplet velocity, wire size and surface tension on the impingement outcomes. They concluded that disintegration is observed in the case of high incoming droplet velocity or small wire diameter whereas dripping drops were observed for low velocity or large wire diameter. Thereafter, dynamics of single droplet impact on superheated cylindrical surfaces were investigated by Rajesh et al. [104] in an experimental study. They found the maximum spread factor of impacted droplet on convex surfaces to be notably higher compared to that on concave and flat surfaces. They also found that the contact time for impinged droplet on convex profile was remarkably less than on flat surface. Moreover, the effect of surface superheat in the film boiling regime was found to be insignificant on maximum spread factor and contact time.

Furthermore, a few numerical studies have also been done in this area by some research groups but none of the available works discuss the post-collision droplet morphology and spreading characteristics of liquid film in detail [102,109,110]. The present chapter aims to explore the post-impact features of droplet on hydrophilic and superhydrophobic (SH) cylindrical surfaces having convex profile. Experimental investigation has been performed for target surfaces having dimeters similar to that of the droplet. The spreading dynamics, wetting behavior, film drainage behavior at the north pole of the cylindrical target, and the lamella dynamics beyond the south pole have been probed and discussed.

3.2 Materials and Methodologies

A custom arranged experimental setup has been used to study post-collision hydrodynamics on cylindrical targets and figure 3.1 illustrates its schematic. A 250 µl chromatography syringe (with a stainless steel 22G gauge needle), attached to a digitally controlled, precision drop dispenser mechanism (Holmarc Opto-Mechantronics Pvt. Ltd., India) having least count of 0.1 µl is employed to generate water droplet which falls freely from a desired height onto the cylindrical target (polished stainless-steel rods of various diameters). A high-speed camera (Photron, UK) mounted with a G-type AF-S macro lens of constant focal length 105 mm (Nikkor, Nikon) is used to capture the impact phenomena at 3600 frames per second (at 1024 x 1024 pixels resolution). Every impact case has been conducted for two camera settings, to obtain the dynamics from both top and front views. In the case of front view, the camera is placed coaxially with the cylindrical target as shown in the figure 3.1.

For the top view, the camera is placed vertically and orthogonally to the axis of the target surface. A brightness controlled white LED (light emitting diode) backlight (Holmarc Opto-mechatronics, India) is used for illumination and is placed such that camera, the target and the centre of the backlight are in a straight line.

The diameter of the water droplet before impact is maintained as ~ 2.8 ± 0.1 mm. It is determined by dispensing a fixed volume of water by the digitized dispenser and also verified by weighing the dispensed droplet using a precision electronic balance (Shimadzu ATX, Japan, least count ~ 0.1 mg). The height of the tip of the needle from the cylindrical target body is varied to provide different droplet impact velocities of ~ 0.95 m/s, ~ 1.17 m/s and ~ 1.5 m/s (all values are accurate to within ± 5 %). The velocities have been determined from image processing of the droplet during its free fall moments before impact. It was ensured that droplet impacts exactly at the centreline of the cylindrical target by continuous monitoring of the experiment result on the computer screen and repeatedly positioning the target body accordingly using trial and error method.

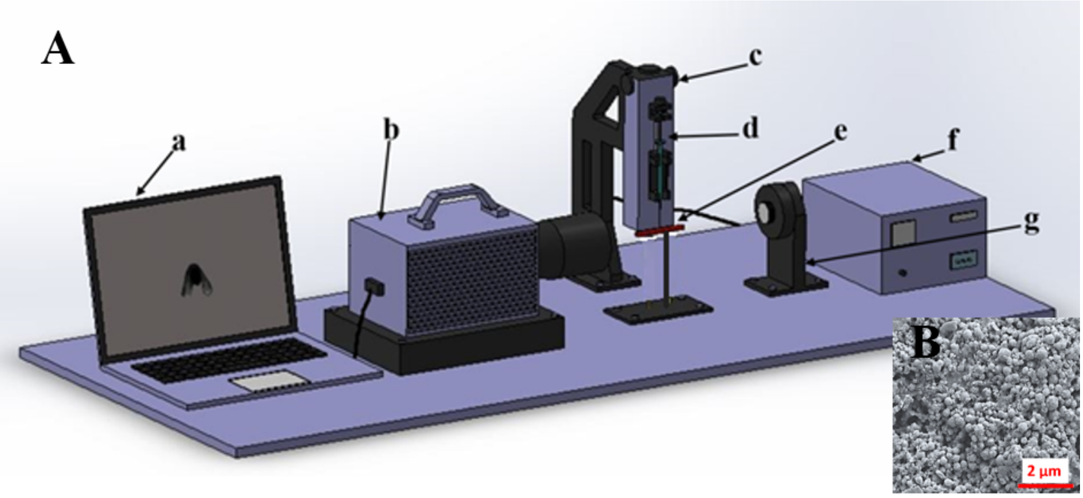

Figure 3.1 (A) Schematic of the experimental setup (a) Computer for data acquisition and control of the camera unit (b) High speed camera with a 105 mm macro lens assembly (c) Precision microliter droplet dispensing mechanism (d) Chromatography syringe with stainless steel needle (e) Cylindrical target body (f) Droplet dispenser unit controller (g) LED illumination unit with intensity controller. (B) SEM image of the SH coated surface.

The target surfaces used for the experiments are stainless steel rods of diameters 1.54 mm, 2.4 mm and 4 mm (diameters are ensured using digital Vernier callipers), which are cleaned with acetone and then dried in hot air oven. Another set of similar rods is spray-coated with a commercial superhydrophobic (SH) concoction (Ultra Tech International Inc., USA) to produce SH rods. The coating thickness ranges in few microns, and hence does not affect the diameter of the rods. The scanning electron microscopy (SEM) image of the coated surface has been illustrated in the inset of figure 3.1.

The images of the collisional events are post processed using the open-source software ImageJ software to quantify various parameters, viz. wetting fraction, spread factor and film thickness at the north pole of the target surface. Illustrations of these parameters have been provided in and defined in figure 3.2. In order to ensure the repeatability of the experiments, each impact was repeated thrice on three randomly selected regions on the target bodies. All experiments were performed at temperature 27 ± 5°C and relative humidity of 55 ± 5%. The static contact angle of water on stainless steel and SH targets were found to be 45° and 135° respectively. The contact angle hysteresis was measured well within 6°, which was in agreement with the literature [111]. The contact angle measurements were performed using a contact angle goniometer (Holmarc Opto-Mechatronics Ltd., India). Additionally, typical values of the surface energies (the liquid-gas and solid-liquid components) for the hydrophilic and SH targets have been tabulated in table 3.1. In table 3.1, the value of σ_{sg} for stainless-steel is deduced using Young's equation ($\sigma_{sg} = \sigma_{sl} + \sigma_{lg} \cos cos\, \theta_c$). By assuming that the σ_{sg} value remains the same for the SH surface, σ_{sl} for the SH surface is deduced.

Table 3.1 The liquid-gas and solid-liquid components of surface energy and static contact angle for cylindrical targets of variant wettability

Cylindrical target	σ_{sl} **(J/m^2)**	σ_{lg} **(J/m^2)**	**Contact angle (θ_c)**
Stainless steel	0.18[a]	0.07286	45 ± 4°
SHS	0.2726	0.07286	135 ± 4°

[a] Reference [112]

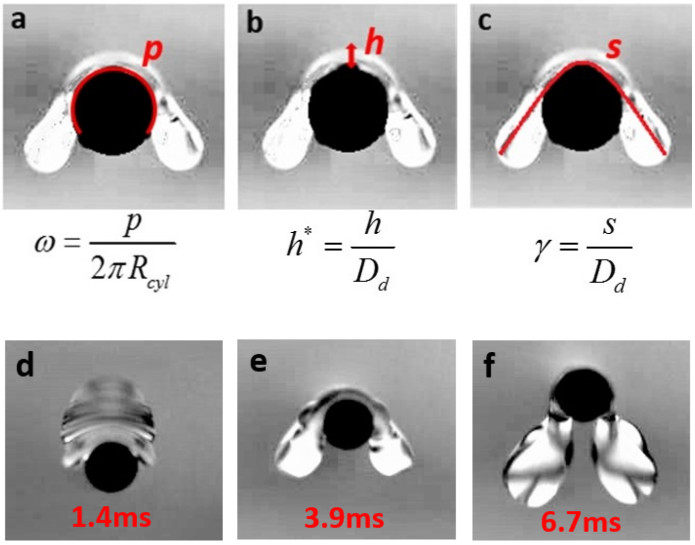

$$\omega = \frac{p}{2\pi R_{cyl}} \qquad h^{*} = \frac{h}{D_d} \qquad \gamma = \frac{s}{D_d}$$

Figure 3.2 Illustration of the transient (a) wetting fraction ω (b) non-dimensional liquid film thickness at the north pole h^{*} and (c) spreading factor γ. The letter p denotes the wetted perimeter of the cross section of the target, the letter h denotes liquid film

thickness at the north pole of the target, the letter s denotes the total lateral spreading length, R_{cyl} symbolizes the radius of the target and D_d denotes the diameter of the pre-impact droplet. Three phases of spreading for droplet impact on 1.54 mm cylindrical target at 0.95 m/s ($We = 36$) are (d) inertial phase (e) viscous phase (f) gravity induced phase.

3.3 Results and Discussion

Experimental images provide an insight to the distribution of liquid film on a cylindrical target at different times after the droplet impaction process. The experimental results have been presented in the form of temporal variations of three non-dimensional parameters, viz. the wetting fraction, the non-dimensional film thickness at the north pole and the spreading factor, which are illustrated in figure 3.2. The wetting fraction ω is expressed as the ratio of wetted perimeter of the cross section of the cylindrical target to the total perimeter of the cross section of the cylindrical target. Non-dimensional liquid film thickness at the north pole denoted by h^* is the ratio of height of liquid film thickness at the north pole to the initial droplet diameter [95]. Spreading factor γ is expressed as the ratio of lateral post impact spreading length to the initial droplet diameter. All these parameters are plotted against non-dimensional time τ represented as $\tau = \frac{tV}{D_d}$, where t is the time evolution from the instant of impact in sand V is the impact velocity in m/s and D_d is the diameter of the droplet before impact in m. The instant $\tau = 0$ corresponds to the moment the droplet just comes in contact with the target surface.

Measurements of p, h and s (figure 3.2) are done via image processing using the open-source processor ImageJ considering wire diameter as reference. In the present study, water droplet (~ 2.7-2.8 mm diameter) impact experiments are conducted on cylindrical targets of two wettability and three diameter ratios, at three impact velocities. The droplet size used is smaller than or similar to the typical capillary length scale for sessile water droplets (~ 2.9-3.0 mm). This ensures that the impact hydrodynamics near the target's north pole is dominated by the surface forces compared to the effects due to gravity. The diameter ratio D^* is defined as $D^* = \frac{2R_{cyl}}{D_d}$ where R_{cyl} is radius of cylindrical target. For all cases, the impact Weber number is defined as $We = \frac{\rho v^2 D_d}{\sigma}$,where ρ is the density of the liquid, v is the velocity at impact (determined from image processing), D_d is the diameter of the droplet at impact and σ is the surface tension of the liquid with respect to air. Throughout the study, the Weber number has been changed by varying the impact velocity of the droplet and D^* is changed by varying the values of R_{cyl}. The spreading behaviour is also governed by the associated capillary number and is defined as $Ca = \frac{\mu v}{\sigma}$.

3.3.1 Hydrophilic Surfaces

The post-impact dynamics have been qualitatively presented in the form of time series arrays. The arrays illustrated in figures 3.3 and 3.4 show the deformation dynamics, wetting behaviour and post-wetting lamella dynamics of a water droplet on a cylindrical surface. Figure 3.3 illustrates a sequence of the front view images at different times for water droplet impact on hydrophilic cylindrical targets (diameter 2.4 mm) with different impact Weber number. It is observed that with the wire diameter remaining constant, impact at higher velocities causes the wire to be completely engulfed by the droplet, whereas at lower velocities, the engulfing is only partial. While the target diameter and the wettability remain unchanged, the inertia of the impact governs the hydrodynamics. At lower We, ($We = 36$), the inertia of the droplet post impact is low and the spreading ceases within 5 ms, and the next stage of film drainage is evident from the array. Beyond 5 ms, the extent of spread remains same and the drainage of the film leads to formation of the lamella below the cylinder.

It is also noteworthy that the liquid film does not meet and coalesce at the south pole, and the two lamellae remain distinctly separated. On the contrary, the spreading is evident to continue in cases of higher We till the point the lamellae coalesce and the whole surface can be seen to be wetted (11.12 ms at $We = 54$ and 6.95 ms at $We = 89$). It is also evident that the regime of spreading and the governing We determines the nature and behaviour of the lamella post spreading. At high We, the lamellae on both ends coalesce due to the large inertial spreading regime and the single column of liquid exhibits capillary instability ($We = 89$, 9.17–15.01 ms). The column eventually breaks up into smaller constituent daughter droplets, characterized by typical necking (13.07 and 15.01 ms) which is similar in behaviour to the typical Plateau-Rayleigh instability of a liquid jet.

The noteworthy behaviour comes to the forefront in case of the moderate We impact. While the inertial spreading leads to coalesce of the film ($We = 54$, 11.12 ms), the lamellae do not coalesce. Instead, two distinct liquid columns appear, which fuses only at the end of the bulging phase, and detach as a single liquid mass due to capillary instability (13.07–15.01 ms). At even lower impact We, the inertial spreading is low and the film does not wet the whole periphery of the target. This causes the lamellae to evolve without wetting and coalescence disturbances, leading to the formation of symmetric bee-wing lamellae ($We = 36$, 9.17 ms). Since the periphery is not fully wetted, the lamellae remain well separated and detach off as independently (at the same time) without coalescence. The absence of lamella coalescence also ensures that the capillary instability before the detachment event is largely reduced in strength, and the two lamellae detach in the form of two minor droplets (15. 01 ms).

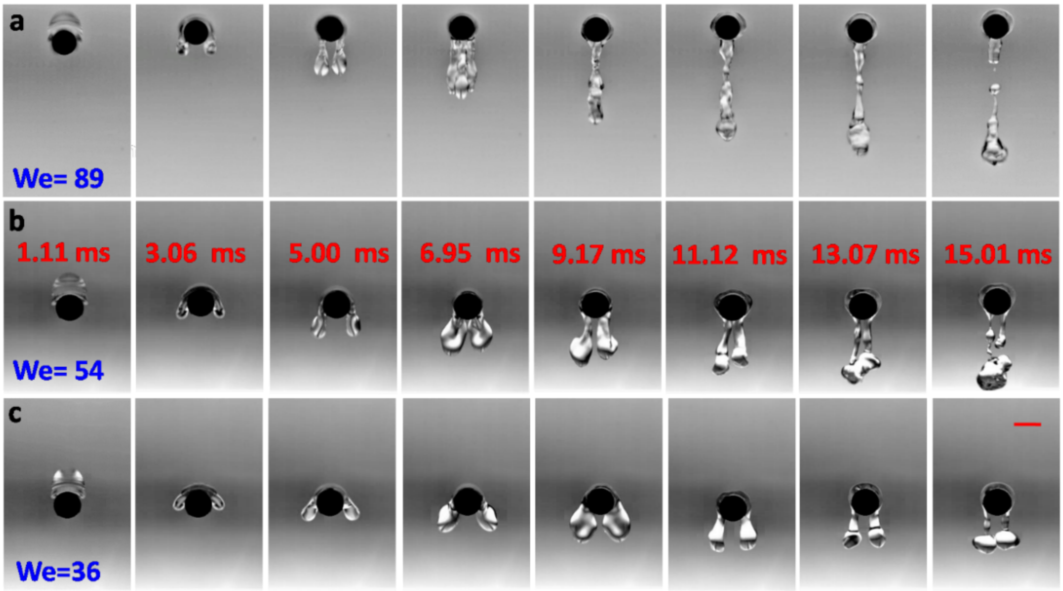

Figure 3.3 Post-impact deformation (front view), wetting and post-wetting lamella dynamics water droplet on hydrophilic cylindrical target surface (diameter 2.4 mm) at

impact velocities of (a) 1.5 m/s, (b) 1.17 m/s, and (c) 0.95 m/s. The associated and the time frames have been illustrated. The magnitude of scale bar (bottom right) is 2.4 mm. Scale bar is same for all images. The array illustrates the role of the impact We.

Another important physical mechanism which is noteworthy is the subsequent film replenishment due to wetting recoil. It can be observed in each case ($We = 89$, 11.12 ms; $We = 54$, 9.17 ms and $We = 36$, 9.17 ms) that the film of liquid near the north pole of the target depletes down to a minimum thickness, and then regains a thicker morphology. This is analogous to the phase at which the lamella development terminates and the lamella detachment phase initiates. During the lamella development regime, the weight of the growing lamella drains the film to a minimum. Beyond this point, the wetting tension between the film and the hydrophilic surface prevents further film drainage. At this juncture, the lamellae are forces to begin its detachment process due to capillary instability, caused by the interactions between the wetting tension at the target and the weight of the lamella. Once the major portion of the lamella begins to detach by necking or threading, the remaining mass of fluid shrouding the target experiences recoil due to capillarity at the neck, leading to partial replenishment of the film near the north pole. It is observable from all the cases that post-detachment of the lamellae leads to increment in thickness of the drained film.

The lamella formation and dynamics is observed to be a strong function of the impact conditions and the post impact structures are different in each case. It is this phase of droplet hydrodynamics where the role of gravity is appreciable since the droplet drips down near the south pole due to the dominant gravitational force over the capillary or interfacial forces. Figure 3.4 illustrates the hydrodynamics of the droplet on cylindrical targets of different diameter ratios (D^*) for evolving time. It is observed that increase in the D^* leads to drastic arrest of the post-impact lamella formation and its hydrodynamics. At low values of D^*, the droplet evolves into a full-fledged butterfly wing shaped lamella and the lamellae further coalesces before the droplet detaches off the southern region of the target, similar to a dripping fashion by forming a chain of microscale droplets. An increase in the D^* arrests the coalescence, and bulbous or ear-ring shaped lamella are generated before detachment. Additionally, the dripping behaviour post lamellae detachment is also arrested. At highest D^*, it can be observed that proto-lamella formation occurs, but the surface hydrophilicity wettability and target size arrests evolution of the spreading and lamella formation, causing the droplet to split up and form three static daughter droplets arranged around the periphery of the target. Figure 3.5 presents the plot of wetting fraction of cylindrical targets of different sizes against non-dimensional time. The wetting fraction ω represents the fraction of perimeter of cross section of the cylindrical substrate which in contact with liquid (illustrated in figure 3.2 (a)).

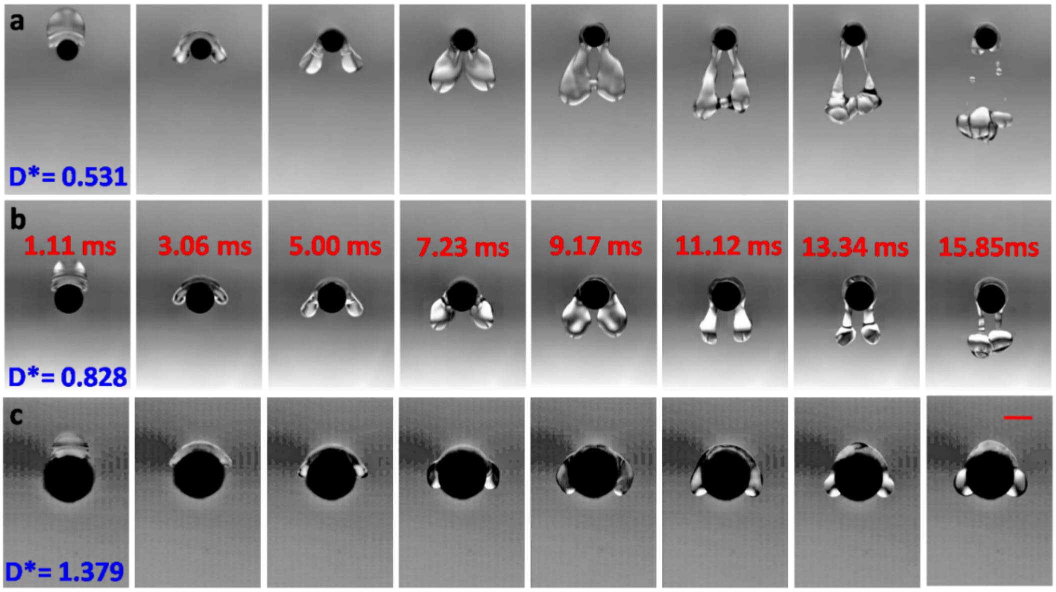

Figure 3.4 Front view of post-impact images of droplet onto hydrophilic cylindrical target surfaces of diameters a) 1.54 mm, b) 2.4 mm, and c) 4 mm at 0.95 m/s impact velocity (impact $We = 36$). The magnitude of scale bar is equal to 2.4 mm (in bottom right image). Scale bar is same for all images. The array illustrates the role of D^*.

In figure 3.5 (A), the wetting fraction for different D^* has been illustrated for impact $We = 36$. The wetting fraction is observed to increase up to a certain time period to attain a maximum value and thereafter decreases during the recoiling phase. Considering the highest value of D^*, it is observed that the wetting fraction attains a plateau, indicating that the droplet spreads and obtains a stable and stationary configuration on the target (as seen in inset (c)). As D^* reduces, the wetting fraction is throughout higher over the whole-time frame. Furthermore, the point of maximum wetting is also attained faster for lower values of D^* since at a fixed We, the engulfment process is faster at lower D^*. At lower D^*, the wetting process terminates into the lamellae formation and subsequent lamella detachment due to capillary instabilities.

As discussed earlier, lamella detachment is associated with capillary recoil, which suddenly pushes back the film of fluid away from the south pole of the droplet by some extent. This behaviour leads to a partial depletion of the wetted film near the south pole and has been described by a reduction in the effective wetting fraction in figure 3.5 (A). Since the capillary recoil is stronger for lower D^* (due to more vigorous capillary instabilities during the lamella detachment), the recoil observed after the wetting maxima is highest for the lowest D^*. Figure 3.5 (B) illustrates a plot similar to figure 3.5 (A) but for impact $We = 89$. In accordance with the above discussion, the wetting fraction is initially higher for lower D^*, but unlike for lower We, the maximum wetting fraction at high We for all D^* eventually becomes 1 and no visible recoil from the maximum is noticeable. This is caused by the higher inertia of impact, which causes the lamellae to coalesce due to inertial spreading. Unlike the capillary coalescence in the lower We cases, the inertial spreading induced coalescence leads to vigorous inertia-capillary instabilities in the fused lamellae (insets (a) and (b) of figure 3.5 (B)). The experimental values depicted in both the plots of figure 3.5 are within ±7 % uncertainty range.

The images corresponding to maximum wetting fraction for each case have been shown as insets in the respective plots. The largest target diameter, as observed in inset (c) of figure 3.5 (A), essentially prevents the drop from spreading towards the south pole, as the larger perimeter is capable of arresting the wetting due to surface shear. However, the same target, in the event of higher We, is unable to arrest the spreading due to the large inertial spreading regime at higher We. The phases of spreading can be essentially deduced from the time plots based on the effective slope of the wetting curve. Three phases of spreading namely, inertial phase, viscous phase and gravity induced phase corresponding to the line plot $D^* = 0.531$ of figure 3.5 (A) are shown in figures 3.2 (d-f). It can be observed that the curves in figure 3.5 (A) contain an initial small region of sharp slope, followed by a region of flattened slope, followed again by a minute region of sharp increasing slope before the peak wetting is reached. The initial region of sharp slope represents the typical inertial phase of spreading, and it can be observed that for a particular D^*, this region is steeper for higher We cases than lower We cases since higher We cases impose faster inertial spreading. The second region of the wetting curve with respect to time is characterized by a change in slope, from the steep initial regime to a smoother segment. This phase of spreading termed as viscous spreading phase is dominated by viscous resistance to the inertial spreading, and the liquid mass approaches the south pole with drastically reduced pace due to shear at the solid boundary. In the case of lower D^*, the viscous shear is not potent enough to arrest the motion like high D^*. Consequently, as the drop traverses towards the south pole, the gravity induced phase of spreading initiates. This third regime of steep slope is observed in the lower D^* cases just before obtaining the spreading maxima or coalescence at the south pole. In addition to the wetting behaviour, the height of the liquid film at the north pole of the target is an important parameter which has been considered in the literature [39,95,97] for spherical targets.

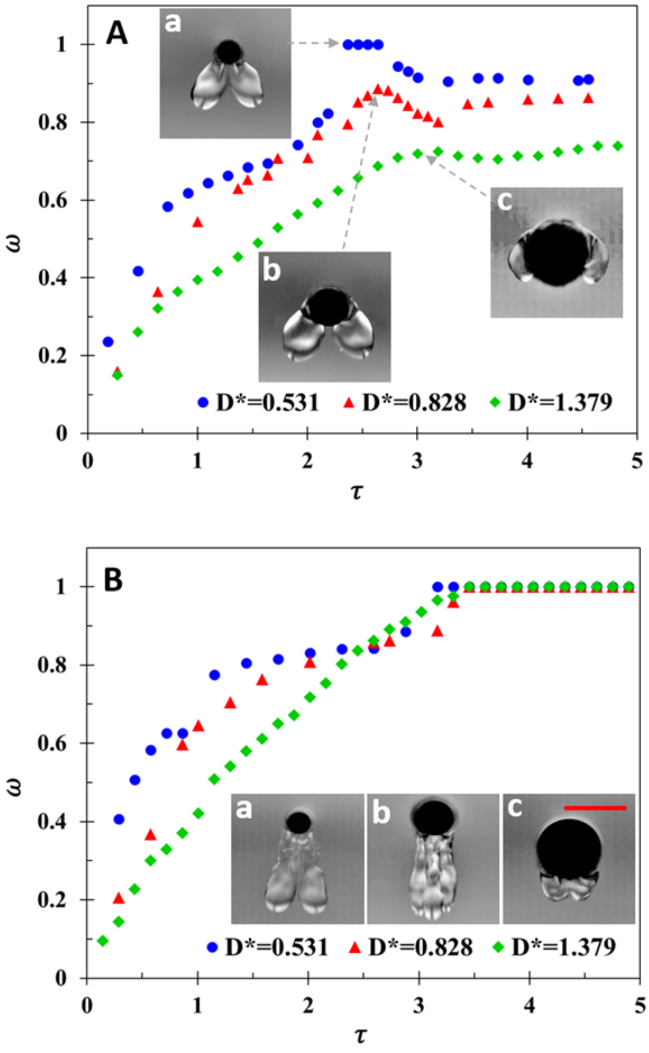

Figure 3.5 Temporal variation of wetting fraction on hydrophilic cylindrical target surfaces of different D^{*} at (A) $We = 36$. Inset: Front view post impact images depicting maximum wetting fraction for (a) $D^{*} = 0.531, \tau = 2.37$; (b) $D^{*} = 0.828, \tau = 2.64$; and (c) $D^{*} = 1.379, \tau = 3$; (B) $We = 89$. Inset: Front view post impact images depicting maximum wetting fraction for (a) $D^{*} = 0.531, \tau = 3.31$; (b) $D^{*} = 0.828$, $\tau = 3.45$; and (c) $D^{*} = 1.379, \tau = 3.45$. The magnitude of scale bar (in inset (c)) is equal to 4mm. The scale bar is the same for all the inset image

Figure 3.6 (A) and (B) illustrates the temporal behaviour of the non-dimensionalized film thickness at the north pole of the cylindrical target (described in figure 3.2 (b)). Sharp drainage of the film is observed in the regime $0 < \tau < 0.8$, for all the cases, which conforms to earlier observations on curved surfaces [97]. The report also suggested that the behaviour can be described using $h^{*} = 1 - t^{*}$ for spherical targets and assuming that the velocity just after the impact remains unchanged. However, it has been observed that for cylindrical targets, this equation does not hold true and a new expression has been derived from first principles at a later stage in the article. After the initial phase of rapid depletion, there is no appreciable change in the film thickness. From figure 3.6 (A) it is observed that the film thickness after the initial phase remains higher for larger values of D^*. This trend is just opposite of what is noted for wetting fraction. Since for higher D^*, the gravity induced film drainage phase near the south pole of the target is largely arrested, the effective thickness near the north pole remains higher. Additionally, for smaller D^*, the lamellae also drain a considerable amount of fluid away during detachment, leading to low values of h^*. As intuition suggests, the film thickness decreases for increasing impact We due to higher contribution due to inertia dominated spreading, which depletes the film at the north pole.

In figure 3.6 (B), a plot similar to 3.6 (A) has been discussed, but for higher We (=89). It is observable that the effect of D^* is largely diminished at higher impact velocities, for $t^* > 0.8$ whereas the trend in the initial deformation phase remains largely unchanged. The spreading factor (γ) is the final non-dimensional coefficient which has been employed to describe the post-impact hydrodynamics on curved surfaces. It is expressed as the ratio of post impact spreading length to initial droplet diameter (depicted in figure 3.2 (c)). The experimental data points marked in the plots of figure 3.6 are within ±7 % uncertainty range. The role of D^* on the spreading factor has been illustrated in figure 3.7 (A) and it is observed that the spreading factor increases with decreasing D^*. For curved systems, the spreading has been considered till the timeframe up to which the droplet does not distort to form the lamellae. The trends observed in figure 3.7 (A) are consistent, and the spreading curves converge towards the flat surface case, which is typically $D^* = \infty$. Two distinct regimes are observed in the spreading evolution, divided by $\tau \sim \sqrt{\frac{8}{3}}$ where, the curves are observed to converge and then further diverge [73].

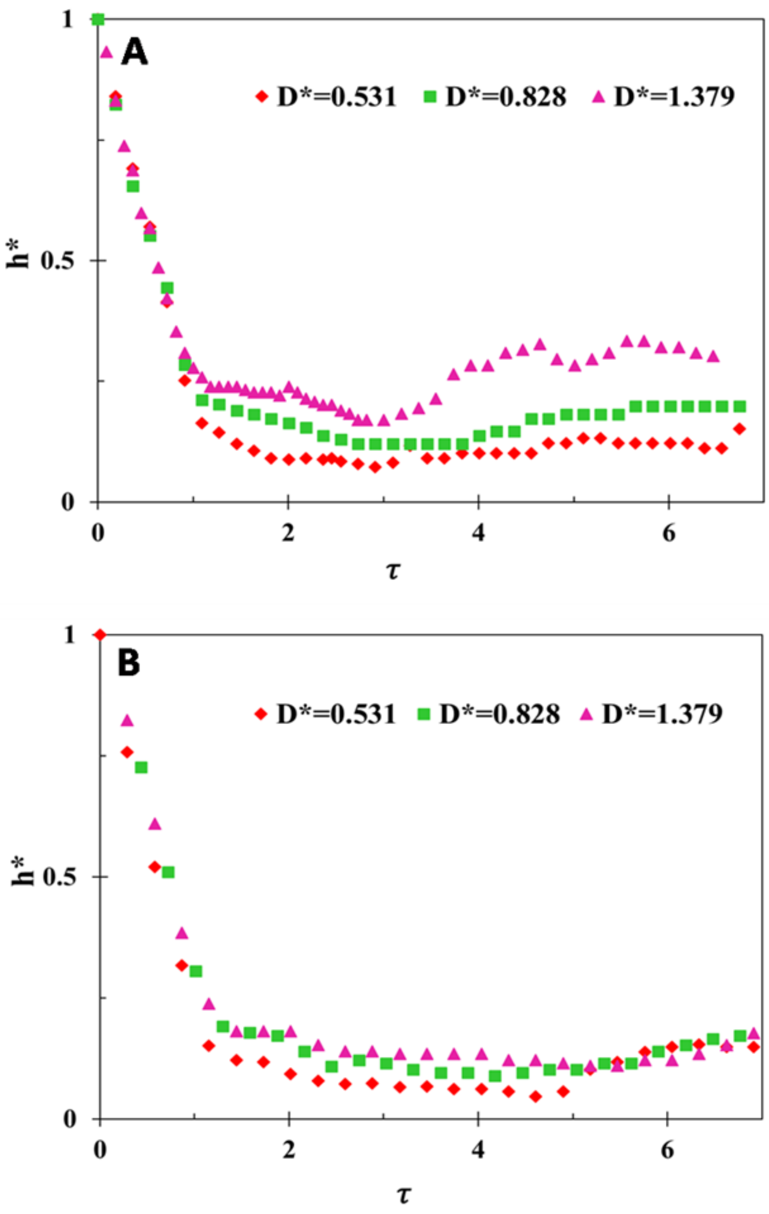

Figure 3.6 Temporal variation of film thickness at the north pole of the hydrophilic cylindrical target surface of different D^* (A) We=36 (B) We=89.

The insets of figure 3.7 (A) represent spreading event for all the curved surfaces at that particular instant. It is interesting to note that at this instant, the spreading for all the surfaces have equal spreading factor of ~ 2.45 and the inset figures show that the shape of the droplet at this instant is fairly self-similar irrespective of the D^*. A distinct behaviour is observed [60] in the time regime $\tau \sim \sqrt{\frac{8}{3}}$, where the spreading factor shows inverse proportionality to the value of D^*, whereas in the regime $\tau \sim \sqrt{\frac{8}{3}}$, the opposite is noted. It is indeed a very important and interesting observation. All the data in figure 3.7 is within ±7 % uncertainty range.

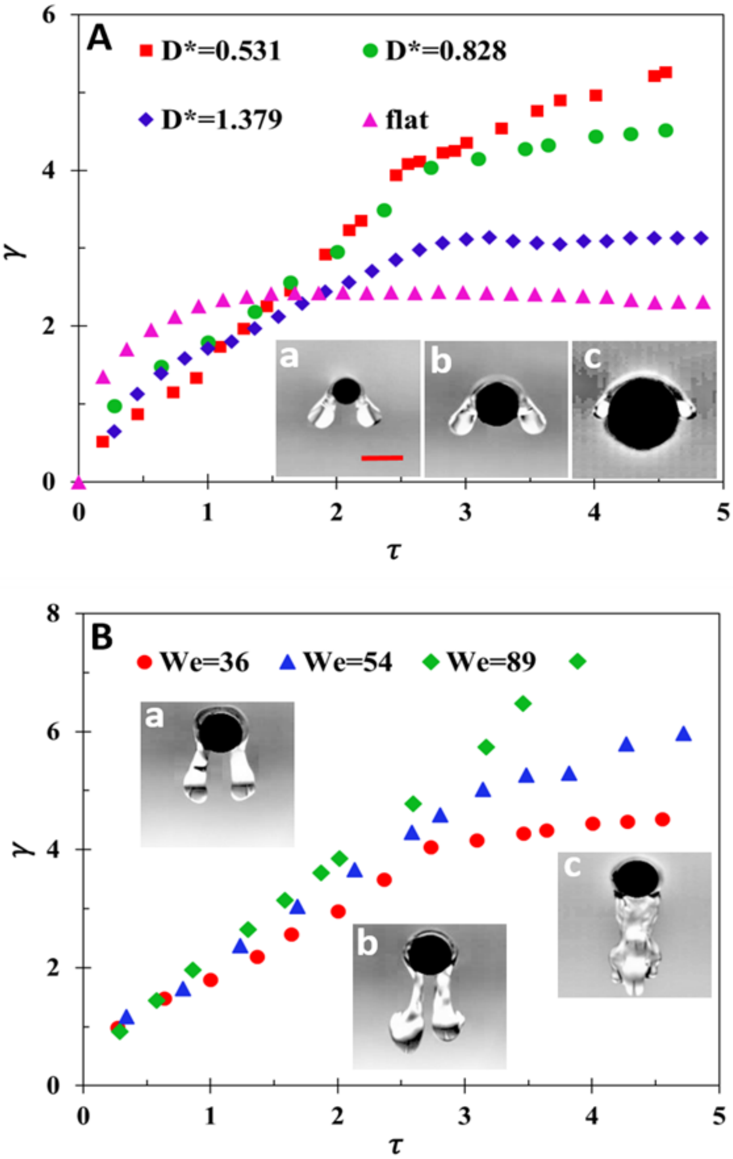

Figure 3.7 (A) Temporal variation of spreading factor on hydrophilic cylindrical target surfaces of different D^* for $We = 36$. Inset: Front view post impact images at $\tau = 1.63$ for (a) $D^* = 0.51$ (b) $D^* = 0.828$ and (c) $D^* = 1.379$. (B) Temporal variation of spreading factor on hydrophilic cylindrical target surface (diameter 2.4mm) at different impact We. Inset: Front view post impact images at $\tau = 3.9$ at impact We (a) 36 (b) 54 and (c) 89. The magnitude of scale bar is equal to 2.4 mm. The scale bar is same for all image

On a flat surface, the spreading event is only arrested by the viscous shear at the surface. In the case of curved surfaces, the initial inertial spreading is opposed not only by the viscous forces, but also by the curvature itself. For the same distance covered during spreading, the perimeter traversed is directly proportional to the diameter of the target. Accordingly, smaller D^* values exhibit lower values of spreading in the initial time regime. Beyond this however, the spreading on flat system arrests due to balance of visco-capillary forces and the inertia. However, on a curved surface, the curvature promotes gravity induced spreading, which largely overcomes the viscous resistance. Since smaller perimeters provide lesser viscous resistance, the gravity induced spreading is much faster for lower D^* targets.

Figure 3.7 (B) illustrates the role of impact We on the spreading hydrodynamics for a constant D^* in this case, the curves show a diverging behaviour, with the spreading enhancing with increasing We. The figures in the inset depict spreading at the same time instant for all We cases illustrating the extent of spreading as function of We. It is interesting to note that up to the timescale $\tau \sim \sqrt{\frac{8}{3}}$, the spreading remains nearly independent of the We. The role of the We initiates beyond this time, which signifies that the inertial regime of spreading is governed dominantly by the D^* compared to the We. It can also be qualitatively noted from figure 3.7 (B) that the spreading curves approach the flat case with a decreasing target curvature.

3.3.2 Superhydrophobic Surfaces

Similar experiments have been conducted on SH targets to understand the effect of wettability on the three geometrical parameters discussed. Figure 3.8 (a) shows a sequence of front-view post-impact images of droplet impact on an SH cylindrical target having 4 mm diameter and impact velocity of 1.5 m/s. The impact outcomes are compared with figure 3.8 (b), which correspond to the equivalent hydrophilic target for the same impact conditions. While coalescence is observed in the hydrophilic case, for SH surfaces, the droplet is repelled off the surface in conjunction with severe deformation and fragmentation. This repulsive fragmentation and deformation are due to the interplay of the capillary forces (much higher σ_{sl} of SH surfaces than hydrophilic surfaces) and the inertial forces. Comparative study of the arrays in 3.8 (a) and 3.8 (b) illustrates that the droplet on SH surface spreads along the surface, however largely without wetting the target, thereby forming elongated proto-lamellae (fourth image from the left in arrays in figures 3.8 (a) and 3.8 (c)).

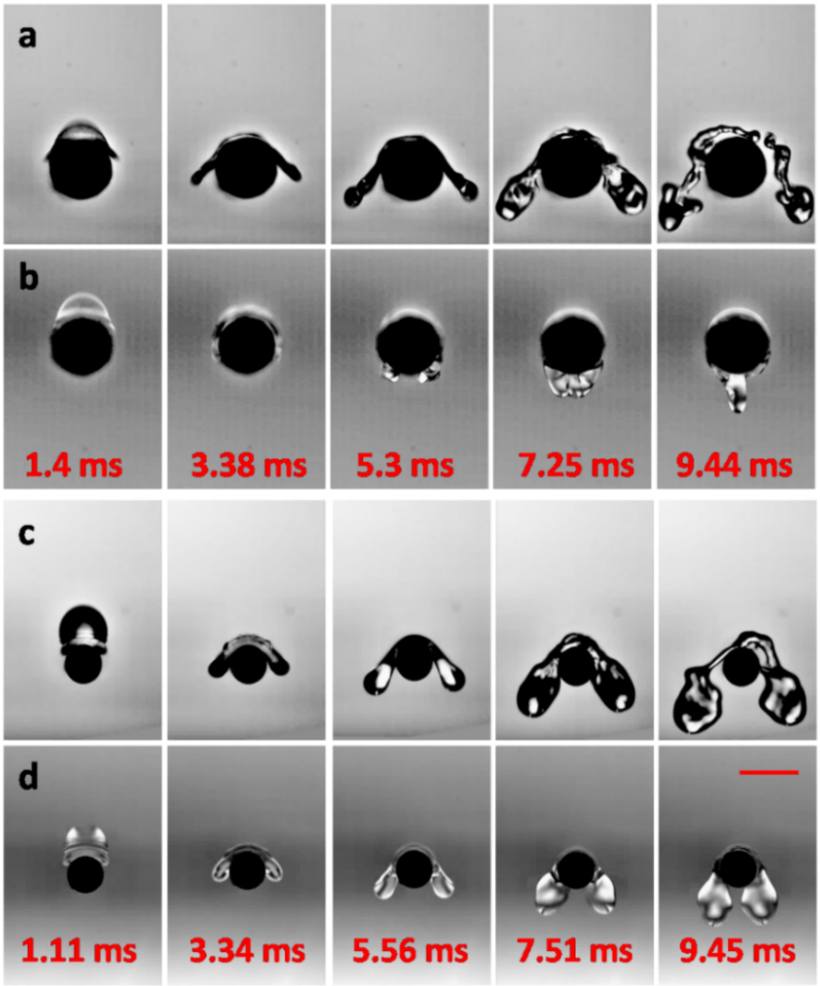

Figure 3.8 Comparison of front view post impact images of droplet onto cylindrical target of different wettability having target diameter 4 mm at 1.5 m/s impact velocity ($We = 89$): (a) SH surface (b) Hydrophilic surface. Comparison of impact for target diameter 2.4mm at 0.95m/s impact velocity ($We = 36$): (c) SH surface (d) Hydrophilic surface. The magnitude of scale bar is equal to 4mm (bottom right). The scale bar is same for all images.

However, the lamellae do not develop like the hydrophilic case, but the droplet deforms and contorts while being repelled off the surface, often leading to fragmentation (last image from left in the arrays in figures 3.8 (a) and 3.8 (c)). Also, in figure 3.8, large brightness and contrast contours (for the same amount of backlight illumination as the hydrophilic cases) in the droplet in the SH case during proto-lamella formation and repulsive ejection can be observed. Such optical contrast is indicative of the large degree of surface capillary instabilities during the lamella formation and ejection away from the surface, which is comparatively less in the hydrophilic counterpart.

Figure 3.9 shows the top view images of the droplet impingement process on hydrophilic and SH cylindrical surface of 4 mm diameter at 1.5 m/s. Top view structures and axial spread are very similar for different wettable targets. It can be seen that the spreading along the axial direction is arrested within the initial few microseconds (~2 ms) and the spread of the drop along the cylinder axis is absent thereafter. These top-view illustrations show that a rimmed edge is formed around the droplet during the spreading event, and capillary instability or capillary waves are visible during the film drainage phase, which are more prominent for SH targets.

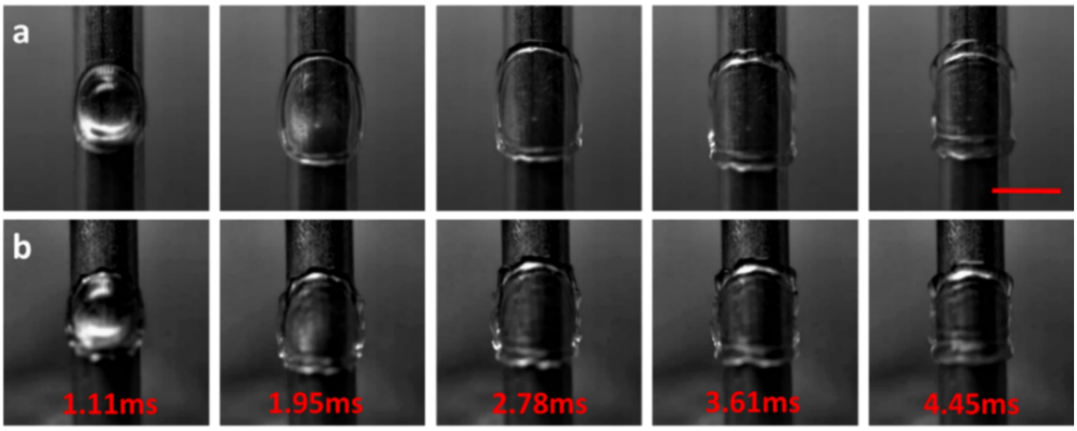

Figure 3.9 Top view images taken at different times for the impact of a water droplet at 1.5 m/s ($We = 89$) onto a 4 mm diameter cylindrical target of different wettability (a) hydrophilic surface (b) SH surface. The magnitude of scale bar is equal to 4 mm. The scale bar is same for all images.

When comparing the wetting fractions for different wettable targets it is found to be significantly less for SH targets compared to hydrophilic (figure 3.10 (A)) due to the high solid-liquid surface energy component of SH surfaces. On the contrary, the spreading factor and non-dimensional film thickness remain very similar for both wettability targets (figure 3.10 (B) and 3.10 (C)).

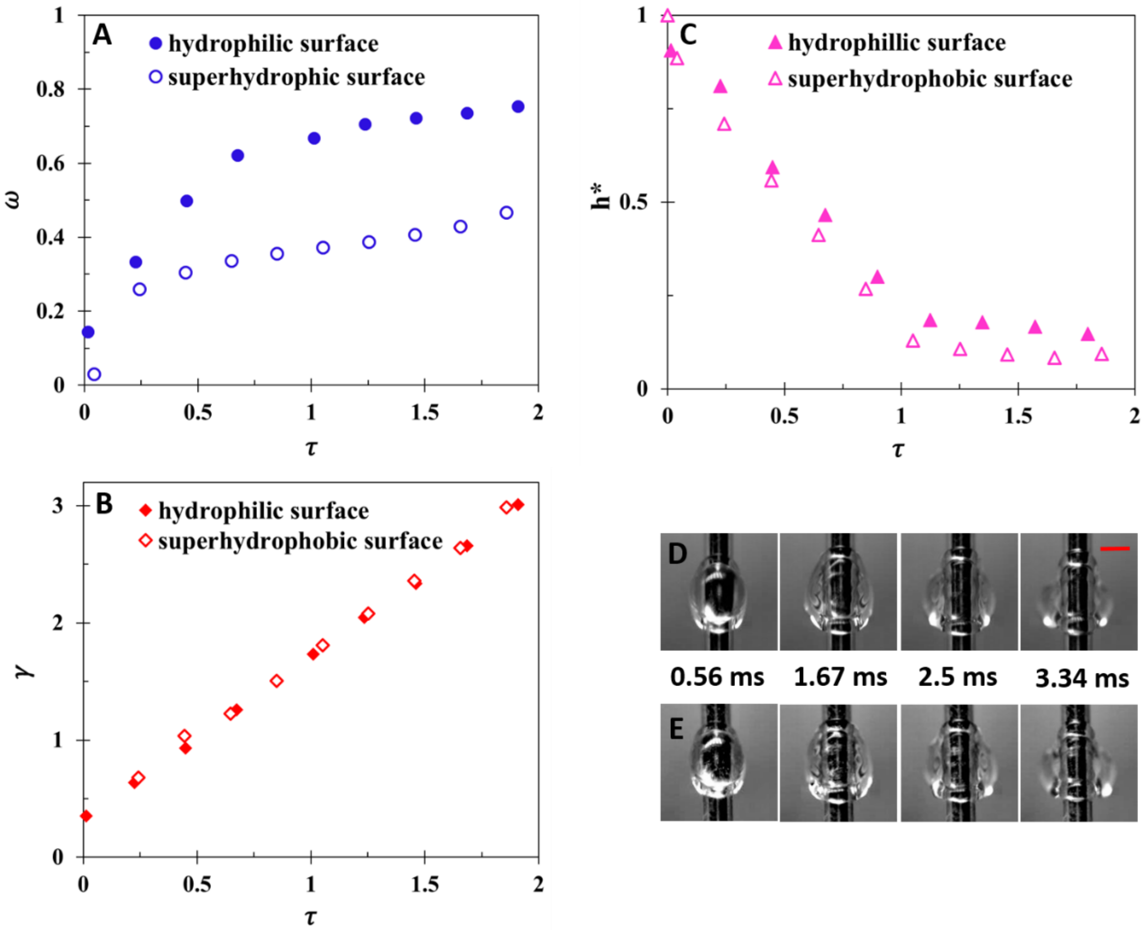

Figure 3.10 Temporal variations of (a) wetting fraction (b) spreading factor (c) non-dimensional film thickness at the north pole of the cylindrical target for different wettability. Comparison of top view post impact images for target diameter 1.54 mm and 1.17 m/s impact velocity ($We = 54$) for (d) Hydrophilic surface (e) SH surface. The magnitude of scale bar is equal to 1.54 mm. The scale bar is same for all images. All the data points are within ±7 % uncertainty range.

However, the phenomena of spreading without wetting creates significant differences compared to spreading with wetting, which can be further seen in the arrays in figure 3.8. Images shown in figure 3.10 (D) and 3.10 (E) compare the top view images of droplet impact on hydrophilic and SH cylindrical target of diameter 1.54 mm at 1.17 m/s, respectively. It is again noted that top view structures are independent of wettability of the target surface. Such observations signify that the major differences in hydrodynamics due to wettability is prominent only as the focus shifts towards the south pole of the target, and at the north pole and its vicinity, impact creates hydrodynamic events which are independent of wettability.

3.4 Mathematical Formulation

The present section discusses a mathematical formulation which has been deduced from first principles to model the hydrodynamics of the droplets post impact. The evolution of the non-dimensional film thickness at the north pole has been derived based on the analytical domain illustrated in figure 3.11. The film evolution process is considered to happen in accordance to the geometry specified in figure 3.11, with minimal flow along the direction of the cylinder axis. This phenomenon has been observed from top view analysis and it is observed that the lateral spread of the droplet during film evolution is negligibly small (figure.3.9). During the inertial spreading $0.4 < \tau < 2.9$, viscous resistance is neglected because the film thickness is significantly larger than the thickness of boundary layer [95]; hence, the major portion of the film spread maybe considered to be an inviscid flow. Also, since the role of gravity very close to the north pole is also negligible, therefore, no hydrodynamic force exists along the tangential direction, and the droplet is assumed to spread in the inertial regime.

The spread of the elemental region c with time can be expressed as [95]

$$\frac{dc}{dt} = u_t$$

(3.1)

$$\frac{du_t}{dt} = 0$$

(3.2)

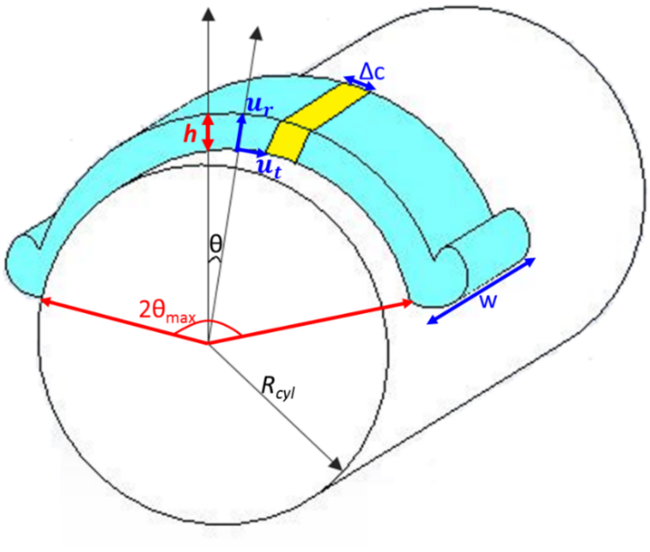

Figure 3.11 Analytical description of the film flow on the cylindrical target during evolution of the film. The similarity of the simplified geometry considered can be observed from figure 3.3, $We = 36$, 3.06 ms, and figure 3.9 (a), 2.78 ms.

where $c = R_{cyl}\theta$, u represents the velocity and subscripts t and r representing tangential and radial, respectively.

The equations are subjected to the initial conditions $c = c_0$ and $u_t = u_0(c_0)$ at $t = t_i$, where t_i is the time instant after which the flow can be considered as a film flow and the negligible viscous resistance can be employed. The generic solutions can be expressed as [95]

$$c = c_0 + u_0(c_0)(t - t_i) \text{ and } u_t = u_0(c_0) \tag{3.3}$$

Furthermore, considering a film element of infinitesimal length Δc as shown in figure 3.11, the analytical form of the system can be realized. The volume of this film element is

$\Delta V = wh\Delta c$, where w and h represent the width and thickness of the fluid element, respectively. The analysis assuming w to be constant throughout the film length (as it is noted that axial spread gets arrested within a short period thereafter) does not change significantly for both hydrophilic and SH targets (refer to figures 3.9, 3.10(d), and 3.10(e)). By applying conservation of mass to this film element, the evolution of the film can be expressed as [95]

$$h\Delta c = h_0(c_0)\Delta c_0 \tag{3.4}$$

where $h_0(c_0)$ is film thickness at instant $t = t_i$. At the limit of vanishing element size, $\Delta c_0 \rightarrow 0$, the generic expression in equation 3.4 can be expressed as

$$h\left(c_0, t\right) = h_0(c_0)\frac{dc_0}{dc} \tag{3.5}$$

From the typical solution expressed in equation 3.3, the equation 3.5 can be further written in the form

$$h\left(c_0, t\right) = \frac{h_0(c_0)}{1+\frac{du_0}{dc_0}(t-t_i)} \tag{3.6}$$

The solution for the differential equation maybe achieved employing the concept of remote asymptotic solution [95]. From the geometry, the tangential velocity immediately after impact conditions can be expressed as

$$u_t = U \sin sin\, \theta \tag{3.7}$$

Where U is the droplet impact velocity. At the vertical axis $(c_0 = 0)u_t = 0$, therefore the initial velocity and initial film thickness can be approximated as a linear function of c_0, expressible as

$$u_0 \approx Ac_0 \text{ and } h_0(c_0) \approx h_0(c_0 = 0) \tag{3.8}$$

Where A is a constant.

Upon combining equations (3.3), (3.5) and (3.8), the expressions for the temporally evolving film thickness and the tangential velocity is obtained as

$$h(t) = \frac{h_0}{1+A(t-t_i)} \tag{3.9}$$

$$u_t = \frac{AR_{cyl}\theta}{1+A(t-t_i)} \tag{3.10}$$

The very initial period, immediately after the impact of droplet on the substrate (in the inertial regime) is refferred to as the Early droplet derformation stage (time instants before t_i). The early deformation stage is a subphase of the inertial spreading regime. During this phase the film thickness at the north pole follows [95]

$$h = D_d - Ut$$

(3.11)

Hence, as discussed earlier (refer to figure 3.2 (d)), the inertial phase can be further subdivied to an early droplet deformation phase, followed by the true inertial phase [95]. In order to obtain the values of determine the parameters h_0, A and t_i, further analysis of the geometrical evolution is necessary. For regions very near the vertical axis ($c_0 = 0$), $u_t \approx U\theta$. Comparing equation 3.8 with this near-axis observation, it can be shown that

$$A = \frac{U}{R_{cyl}} \tag{3.12}$$

At $t = t_i$, the early droplet deformation phase comes to an end and the main part of inertial regime begins, where the flow can be considered as the film flow. At $t = t_i$, two different expessions for $\frac{dh}{dt}$ can be found from equations 3.9 and 3.11, respectively.

When equated (to establish the curve continuity condition), the expressions yield the values of constants t_i and h_0 as

$$h_0 = R_{cyl} \tag{3.13}$$

$$t_i = \frac{D_d - R_{cyl}}{U} \tag{3.14}$$

Upon substituting the expressions in equations 3.12-3.14 in equation 3.9 the final expression is obtained as

$$h(t) = \frac{R_{cyl}^2}{2R_{cyl} + Ut - D_d} \tag{3.15}$$

Hence, the expression for the non-dimensionalized film thickness at the north pole of the cylindrical target is

$$h^*(t) = \frac{R_{cyl}^2}{2R_{cyl}D_d + D_d^2\tau - D_d^2} \tag{3.16}$$

The theoretically deduced values of the film thickness have been compared in figure 3.12 against the experimentally observed values, for different We, D^* and wettability, and good agreement has been observed. In addition to modelling the film thickness evolution during the inertial spreading regime, a theoretical model to determine the maximum wetted angle ($2\theta_{max}$, represented in figure 3.11) on the cylindrical body has also been proposed. The maximum wetted angle ($2\theta_{max}$) can be defined as the angle corresponding to the maximum wetted perimeter of cross section of cylindrical target. Beyond this regime, the droplet may spread, however, without wetting contact at the surface.

Based on energy balance principle, the pre- and post-impact energies are considered to be conserved, and expressed as [113]

$$k.e_i + s.e_i = s.e_1 + s.e_2 + s.e_3 + s.e_4 + v_{dis} \tag{3.17}$$

The change in potential energy is neglected in equation 3.17 because of its small magnitude compared to other energy components [61,113] during spreading on a millimetric scale cylindrical wire. The pre-impact kinetic energy can be expressed as

$$k.e_i = \frac{1}{2}\left(\rho U^2\right)\left(\frac{\pi D_d^3}{6}\right) \tag{3.18}$$

Considering that the droplet before impact assumes a perfectly spherical shape (experiments reveal that the droplets are nearly spherical before impact; however, mild distortions are possible, which are neglected in the present case), the surface energy of the droplet pre-impact is expressed as

$$s.e_i = \pi D_d^2 \sigma_{lg} \tag{3.19}$$

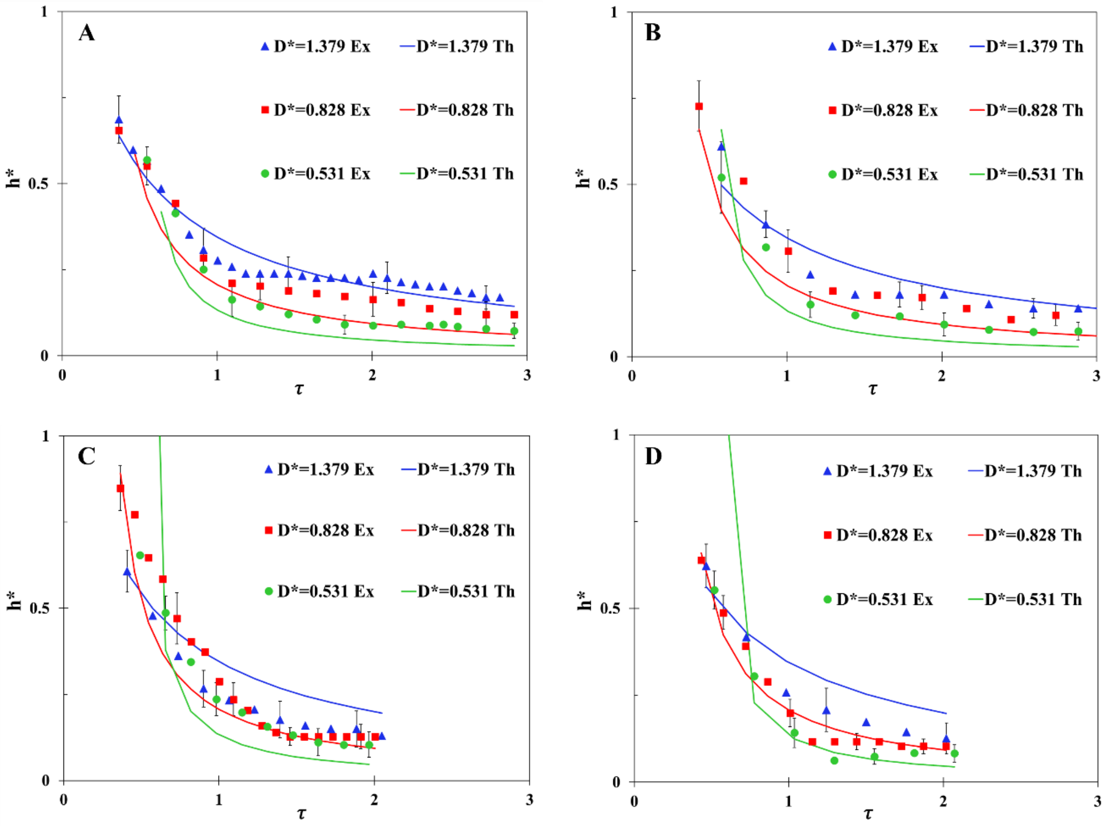

Figure 3.12 Comparison of experimental (Ex) and theoretical (Th) film thickness evolution of water droplets at the north pole for (A) $We = 36$ on hydrophilic surface, (B) $We = 89$ on hydrophilic surface, (C) $We = 36$ on SH surface, and (D) $We = 89$ on SH surface.

Post-impact, the energies are a sum of the variant surface energy components and the viscous dissipation work done by the droplet while spreading against the surface. The viscous dissipation work can be expressed as [113]

$$v_{dis} = \int_0^{t_c} \int_V \psi \, dV dt$$

(3.20)

The dissipative energy can be expressed as a function of the impact velocity and the analogous boundary layer thickness δ as [113]

$$\psi \approx \mu \left(\frac{U}{\delta} \right)^2 \tag{3.21}$$

Based on a boundary layer flow analogy over a flat plate (it is assumed that the spreading process is largely inertia driven such that the curvature effects do not give rise to pressure gradients. Moreover, the dimensions are very small), the boundary layer thickness can be scaled as

$$\delta \sim \frac{5R_{cyl}(2\theta_{max})}{\sqrt{Re}} \tag{3.22}$$

where $Re = \frac{\rho U R_{cyl}(2\theta_{max})}{\mu}$. The effective volume of the liquid under the action of the viscous dissipative work can be expressed as [113]

$$V_{dis} = R_{cyl}(2\theta_{max}) w \delta \tag{3.23}$$

where the width of the spreading liquid layer is of the form

$$w = \frac{\pi}{6} \frac{D_d^3}{R_{cyl}(2\theta_{max})h_{\frac{\theta}{2}}} \tag{3.24}$$

In equation 3.24, $h_{\frac{\theta_{max}}{2}}$ denotes the liquid film thickness at the time instant of maximum spreading at polar location $\frac{\theta_{max}}{2}$.The average time of spreading, during which the viscous forces are dominant can be scaled as

$$t_{spread} \sim \frac{R_{cyl}\theta_{max}}{U} \tag{3.25}$$

Integrating equation 3.20 with the expressions obtained from equations 3.21–3.25, the final form of the viscous dissipation work component can be expressed as

$$v_{dis} = \frac{\pi D_d^3}{6} \frac{U\mu R_{cyl}(2\theta_{max})}{2h_{\frac{\theta_{max}}{2}}\delta} \tag{3.26}$$

In addition to the viscous work, the components of surface and interfacial energies also play a governing role on the droplet hydrodynamics post impact. The component of surface energy due to the solid-liquid interface during the film drainage regime can be expressed as

$$s.e_1 = \frac{\pi D_d^3 \sigma_{sl}}{6h_{\frac{\theta_{max}}{2}}} \tag{3.27}$$

Likewise, the component of surface energy due to the liquid-gas interface during the film drainage regime is of the form

$$s.e_2 = \frac{\pi d^3 \sigma_{lg}}{6h_{\frac{\theta_{max}}{2}}} \tag{3.28}$$

In the spreading regime, the component of surface energy due to the liquid-gas interface is of the form

$$s.e_3 = \frac{\pi D_d^3 \sigma_{lg}}{3R_{cyl}(2\theta_{max})} \tag{3.29}$$

while the surface energy in the spreading regime due to the solid-liquid interface is expressed as

$$s.e_4 = 2R_{cyl}(2\theta)h_{\frac{\theta_{max}}{2}}\sigma_{lg} \tag{3.30}$$

Substituting all the energy components in equation 3.17, the net energy balance equation is

$$\frac{1}{2}\left(\rho U^2\right)\left(\frac{\pi D_d^3}{6}\right) + \pi d^2\sigma_{lg} = \frac{\pi D_d^3}{6h_{\frac{\theta_{max}}{2}}}\left(\sigma_{sl} + \sigma_{lg}\right) + \frac{\pi D_d^3\sigma_{lg}}{3R_{cyl}(2\theta_{max})} + 2R_{cyl}\left(2\theta_{max}\right)h_{\frac{\theta_{max}}{2}}\sigma_{lg} + \frac{\pi D_d^3}{6}\frac{U\mu R_{cyl}(2\theta_{m}}{2h_{\frac{\theta_{max}}{2}}\delta}$$

(3.31)

Non-dimensionalizing the expression with respect to the initial surface energy of the pre-impact droplet, the relationship between the spreading angle is obtained in terms of the governing Weber (We) and Capillary (Ca) numbers as

$$\frac{We}{12} + 1 = \frac{Ca}{12}\frac{R_{cyl}D_d(2\theta_{max})}{h_{\frac{\theta_{max}}{2}}\delta} + \frac{D_d}{6h_{\frac{\theta_{max}}{2}}}\left(1 + \frac{\sigma_{sl}}{\sigma_{lg}}\right) + \frac{D_d}{3R_{cyl}(2\theta_{max})} + \frac{2R_{cyl}\left(2\theta_{max}\right)h_{\frac{\theta_{max}}{2}}}{\pi D_d^2} \tag{3.32}$$

which can be further expressed as a quadratic function of $2\theta_{max}$ as

$$\left(\frac{Ca}{12}\frac{R_{cyl}D_d}{h_{\frac{\theta_{max}}{2}}\delta} + \frac{2R_{cyl}h_{\frac{\theta_{max}}{2}}}{\pi D_d^2}\right)2\theta_{max}^2 + \left(\frac{D_d}{6h_{\frac{\theta_{max}}{2}}}\left(1 + \frac{\sigma_{sl}}{\sigma_{lg}}\right) - \frac{We}{12} - 1\right)2\theta_{max} + \frac{D_d}{3R_{cyl}} = 0 \tag{3.33}$$

The equation 3.33 is solved and the theoretical values are compared with the experimentally observed values of $2\theta_{max}$ and have been illustrated in figure 3.13 for representative impact and wettability conditions. It is observed that for hydrophilic surfaces, the model performs better in case of higher D^* and lower We regimes, whereas for SH surfaces, the performance is better for higher D^* as well as higher We regimes. In case of lower D^*, the droplet undergoes rapid film drainage caused by the large curvature, which reduces the components of surface energies due to film drainage, thereby reducing the predictability of the model. On hydrophilic bodies, the high We regime leads to enhanced splashing component of surface energy, which is not accounted for in the model, and hence the deviations enhance for high We on hydrophilic surface. On the contrary, on SH surfaces, higher inertia ensures proper spread of the droplet before the capillary forces breaks the droplet up into daughter droplets. At lower We, the spread of the droplet is insufficient due to lower inertia, and hence the model performs poorly for low We regime on SH surfaces.

3.5 Closure

The study of droplet impact dynamics on cylindrical target surfaces can have pronounced effects in improving the spray-cooling and coating efficiency of turbine blades, microscale machine components and automotive parts. Additionally, the hydrodynamics on such curved target features are rich in physics therefore attract fundamental academic research. The present chapter experimentally investigates the post-impact hydrodynamics of water
droplets on cylindrical targets of different diameters and wettability. The post-impact hydrodynamics have been quantified employing dedicated non-dimensional variables, such as the wetting fraction, the spreading factor, and the non-dimensional film thickness at the north-pole of the target. The study involves variant impact We and hydrodynamic behavior such as wetting, spreading, film drainage and lamellae formation and behavior have been studied in depth using high speed photography, both from side and top views. It is observed that when the target diameter is increased with respect to the droplet size at

the same impact We, the wetting fraction and spread factor decrease, whereas the film thickness increases. Upon increasing the impact We, the effect of curvature on wetting fraction, spread factor and film thickness is observed to reduce. It is also observed that the maximum wetting fraction is attained faster for lower diameter ratios.

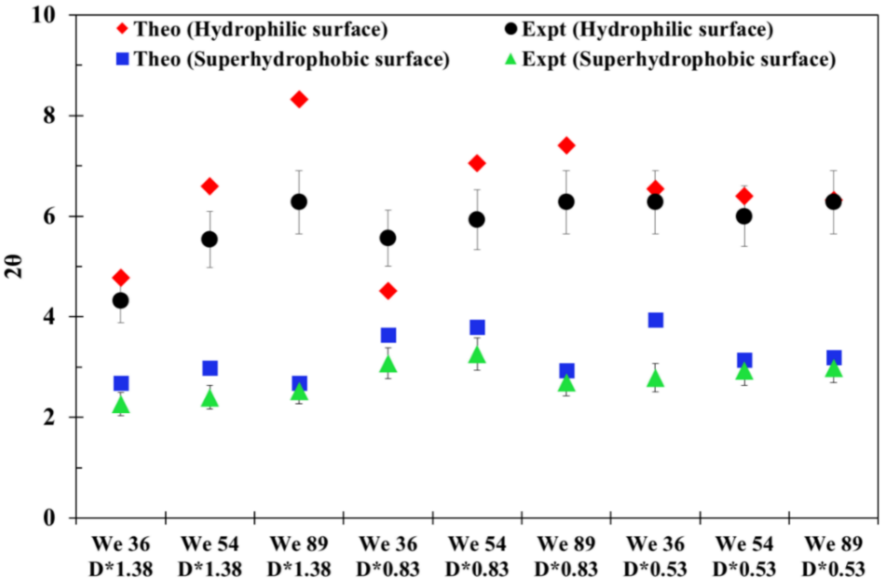

Figure 3.13 Comparison of experimental (Expt) and theoretical (Theo) values of $2\theta_{max}$ for various impact conditions on Hydrophillic and Superhydrophobic cylindrical targets.

Moreover, in the case of SH surfaces, the wetting fraction reduces significantly, whereas the spread factor remains comparable to that of hydrophilic surfaces. It is also shown that the diameter ratio and impact We has a direct influence on the lamellae shape, growth behavior, formation and break-off dynamics, as well as on its instability behavior during breakup mode. Additionally, an analytical expression for temporal evolution of the film thickness at the north pole of the target has been presented and good agreement is achieved with respect to experimental data. Having discussed the morphology of post impact droplet, a theoretical model based on energy conservation principle has also been proposed to predict the maximum wetting fraction on a given cylindrical target surface. The model predicts the spreading of the droplet over the curved surface in terms of the governing We and Ca. The model is observed to be able to predict the experimental results with appreciable accuracy, considering the highly dynamic and statistical nature of such impact and wetting phenomena. The present chapter thus sheds good insight on the hydrodynamics of droplets and post-impact events on cylindrical targets and illustrates the effects of diameter ratio, impact We and Ca and wettability on the post impact fluid dynamics.

Chapter 4

Post-Impaction Droplet Hydrodynamics on Spherical Surfaces

4.1 Introduction

The hydrodynamics of droplet impact has attracted the attention of the scientific community all over the world for its fundamental rich physics and intrinsic physical beauty. Understanding the droplet post-impingement dynamics on spherical surfaces is of importance in tablet coating and encapsulation processes, such as in detergents and pharmaceutical products, for spray coating or painting of complex shape components and so on [114-117]. A few studies are found in literature discussing the outcomes of droplet impact on spherical targets of varying dimensions and surface properties but none of them provide detailed investigation of post-impingement hydrodynamics [94,96,97,118]. In this chapter post-collision wetting and spreading dynamics are explored with side and top views of impaction phenomenon using a high-speed imaging technique. The morphological outcome of this impingement process has been quantitatively and temporally probed. The nature of the droplet not only during the impact but during the lamella phase toward the target's south-pole has also been studied. Furthermore, an analytical model, based on energy balance principle, has been proposed to quantify a maximum spread angle for various impact conditions. Although, such analytical models have already been developed in the earlier studies, none of them are established for target-to-droplet diameter ratios varying from less to more than 1. The current model is able to predict the hydrodynamics on a wide range of target-to-droplet diameter ratios. The proposed model has been noted to accurately predict the wetting and spreading behaviour for such complicated impact regimes.

4.2 Experimental Methods

The experimental setup used is illustrated in figure 4.1. Droplets (diameter ~2.8 mm) are generated using a 250 μl glass syringe (with a stainless steel 22G gauge needle), which is controlled by a precision drop dispenser mechanism (least count 0.1 μl). The diameter of the droplet is found by dispensing a fixed liquid volume by the dispenser and verified during image post-processing. The droplet is allowed to impact from desired heights to impart ~0.94 m/s, ~1.17 m/s, and ~1.5 m/s (accurate within ± 5 %). The impact dynamics is captured at 3600 frames per second (1024×1024 pixels resolution) by a high-speed camera (Photron, UK), with a G-type AF-S constant focal length (105 mm) macro lens (Nikkor, Nikon). To capture the front view, the camera is placed as shown in figure 4.1. For top view images, the camera is placed vertically, perpendicular to the front view position. A brightness controlled white LED (light emitting diode) backlight (Holmarc Opto-Mechatronics, India) is used for backlight illumination.

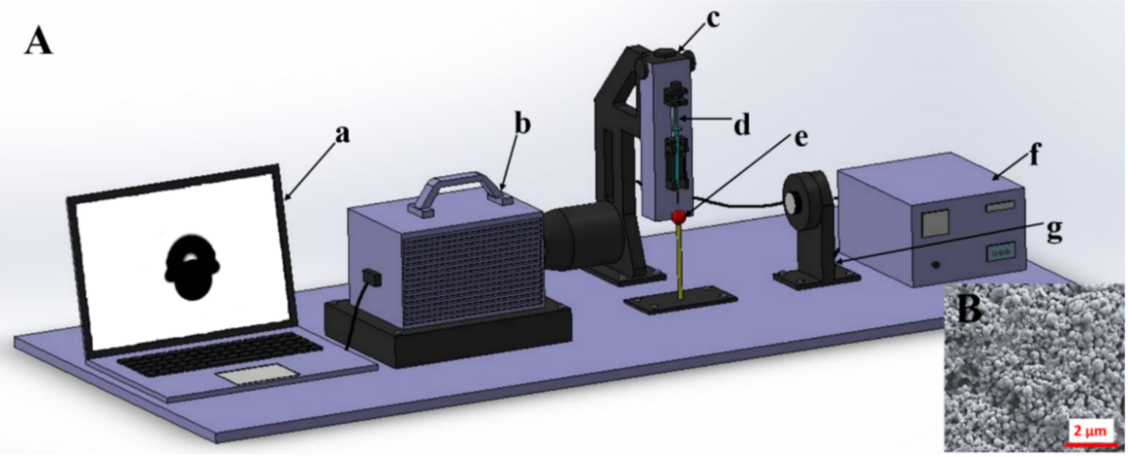

Figure 4.1 (A) Schematic of the experimental setup (a) computer for data acquisition and camera control (b) high speed camera with a 105 mm macro lens (c) digitized microliter droplet dispenser (d) microliter syringe with stainless steel needle (e) spherical body (f) droplet dispenser and backlight illumination controller (g) LED backlight (B) SEM image of the coated SH coated.

Deionized water has been used and the spheres are of 2.4, 3.2, 4.71, 6.95, and 9.5mm diameter (polished stainless-steel balls), which are cleaned with acetone and then dried in hot air oven. Another set of similar balls are then coated with a commercial superhydrophobic (SH) spray (Ultra Tech International, Inc., USA) to produce SH spheres. The scanning electron microscopy (SEM) image of the coated surface is illustrated in figure 4.1 (B). The images have been post-processed using the open-source code ImageJ quantify parameters, viz., liquid film thickness at the north-pole, spread factor and the maximum spreading angle. Several trials were performed to ensure impact of the droplet exactly at the north pole of the spheres. Each case was repeated twice on three different sample targets for repeatability. Temperature of 27 ± 3°C and relative humidity of 55% ± 5% conditions were maintained for all the experiments.

Table 4.1 shows the surface energy values and static contact angles of spherical targets. The superhydrophobic coating used for the experiments mainly contains butyl acetate and methyl isobutyl ketone, and σ_{sg} values of these have been adapted from manufacturer's datasheet [119,120]. From the data in Table 4.1, σ_{sl} for stainless steel and superhydrophobic surface (SHS) is deduced from $\sigma_{sg} = \sigma_{sl} + \sigma_{lg} \cos cos\, \theta_c$ (Young's equation).

Table 4.1 The liquid-gas and solid-gas components of surface energy and static contact angles for spherical surfaces.

Spherical target	σ_{sl} **(J/m^2)**	σ_{lg} **(J/m^2)**	**Contact angle (θ_c)**
Stainless steel	0.77[a]	0.0728	85° ± 3°
SHS	0.018[b]	0.0728	145° ± 3°

[a]Reference [121], [b]Reference [119,120]

4.3 Results and Discussions

The temporal variations of nondimensional liquid film thickness at the north pole of the target and the spread factor of the droplet exhibit film flow dynamics after the impact.

These hydrodynamic trends are presented against the non-dimensional time, $\tau = \frac{tV}{D_d}$ where t is the time evolution, V is the droplet impact velocity, and D_d is the droplet diameter just before impact. The maximum spread angle is also measured for all cases. The parameters measured, i.e., s (shown in inset figure 4.5), h (shown in inset figure 4.6), and 2θ, i.e., maximum spread angle (shown in figure 4.10) are illustrated for clarity. A diameter ratio has been defined as $D^* = \frac{2R_{sub}}{D_d}$, where R_{sub} is radius of the spherical target. The associated governing nondimensional numbers are the Weber, Reynolds and Capillary numbers, which are mathematically expressed as, $We = \frac{\rho V^2 D_d}{\sigma}$, $Re = \frac{\rho V D_d}{\mu}$, and $Ca = \frac{\mu V}{\sigma}$, where ρ is the density of the liquid, σ is the surface tension of the liquid, and μ is the dynamic viscosity of the liquid.

4.3.1 Hydrophilic Surfaces

Figure 4.2 illustrates the sequence of front view post-collision images on a 2.4 mm diameter hydrophilic sphere at three different impacts We. It is observed that for higher We, the droplet elongates more due to inertial draining than lower We cases. The effect of impact We is evident from this array. The lamella formed at ~3.89 ms is noted to be a strong function of impact We. Interesting shapes are acquired by the droplet, from a hat shape ($We = 34$), to a shape resembling a seasoning holder ($We = 52$), to a shape resembling a chess pawn ($We = 89$). This shows the inertial dependence on the postimpact spreading.

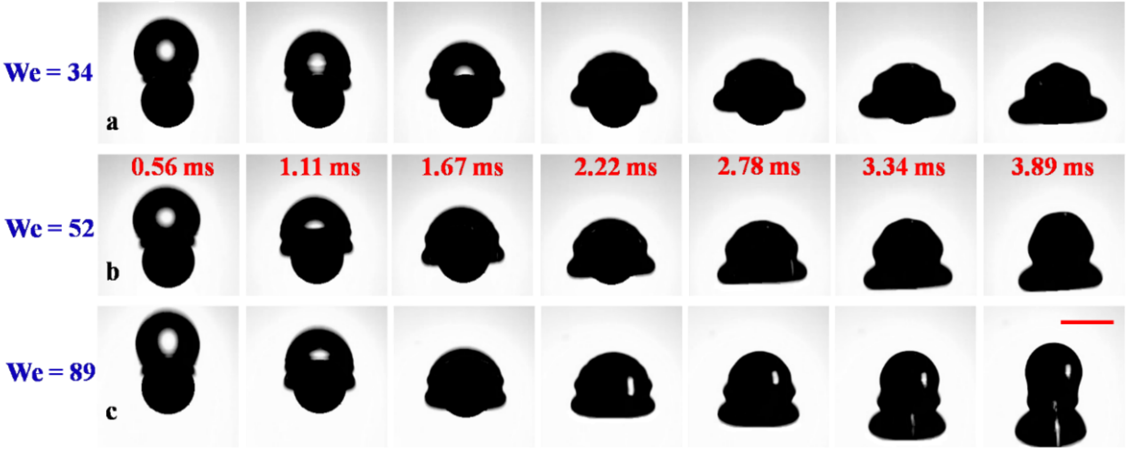

Figure 4.2 Postcollision morphology of droplets on hydrophilic sphere (diameter 2.4 mm) at impact velocities of (a) 0.94 m/s, (b) 1.17 m/s and (c) 1.5 m/s. The associated We and the time frames are mentioned. The scale bar (bottom right) represents 2.4 mm. Scale bar is same for all images. The array illustrates the role of the impact We.

Figure 4.3 illustrates the role of D^* on the hydrodynamics of the spreading droplet. Hydrophilic spheres having D^* values as 0.86, 1.14, and 1.68 are presented. It is observed that for lower D^*, the droplet completely engulfs the target sphere, whereas only partial engulfment was possible for higher D^*. It is also noted that the droplet evolves into a hat type structure for large values of D^* due to arrest of spread, whereas the liquid film flows over the target and forms a rim for lower D^*. When D^* is further increased, as depicted in figure 4.4, drastic arrest in the spreading characteristics is noted. For impact on large spheres, the hydrodynamics is quite similar to that of droplet impact on flat surfaces. The postimpact structure resembles a curved disk, and on acquires the curvature of the target sphere (which is absent in flat cases). The lamella formed spreads to larger extents at high We cases, leading to forming of thin wetting film at the north-pole of the sphere.

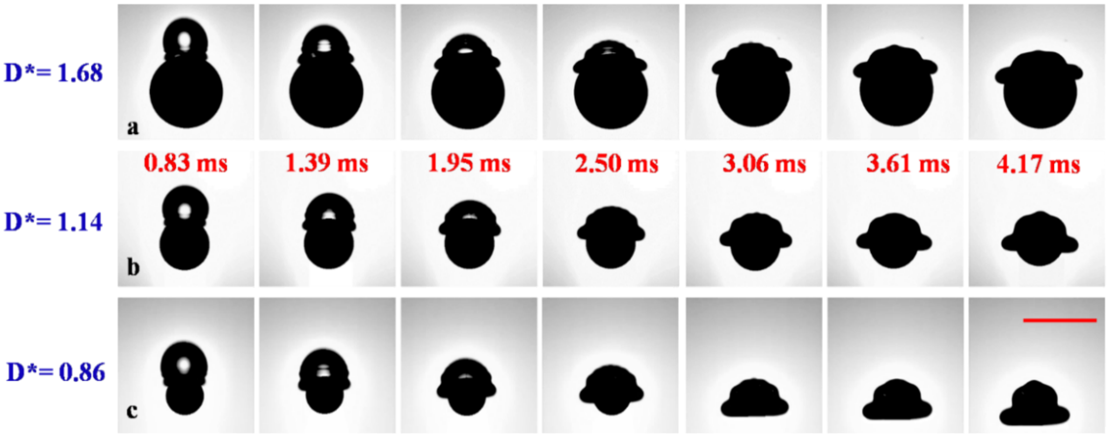

Figure 4.3 Postimpact deformation of droplet impacted at 0.94 m/s velocity (impact $We = 36$) on hydrophilic spheres of diameters (a) 4.7 mm (b) 3.2 mm and (c) 2.4 mm. The associated D^* and the time frames are mentioned. The scale bar is equal to 2.4 mm (in bottom right). Scale bar is same for all images. The array illustrates the role of D^*.

Fig 4.5 (A) illustrates the spread factor on hydrophilic spheres of different D^* against the non-dimensional time. The spread factor γ is expressed as $\gamma = \frac{s}{D_d}$, where s is the lateral post-impact spreading length (as marked in inset of figures 4.5 (A) and 4.5 (B)). It is observed that for the initial phases of spreading, the γ nearly similar for all D^* spheres, but after τ≅1, the curves diverge, with the low D^* showing increased spreading. Larger targets provide more viscous shear and obstruct the evolution of spreading. Insets (a)-(c) of figure 4.5 (A) illustrate the spreading event for substrates of D^* values 2.48, 1.68, and 0.86, respectively.

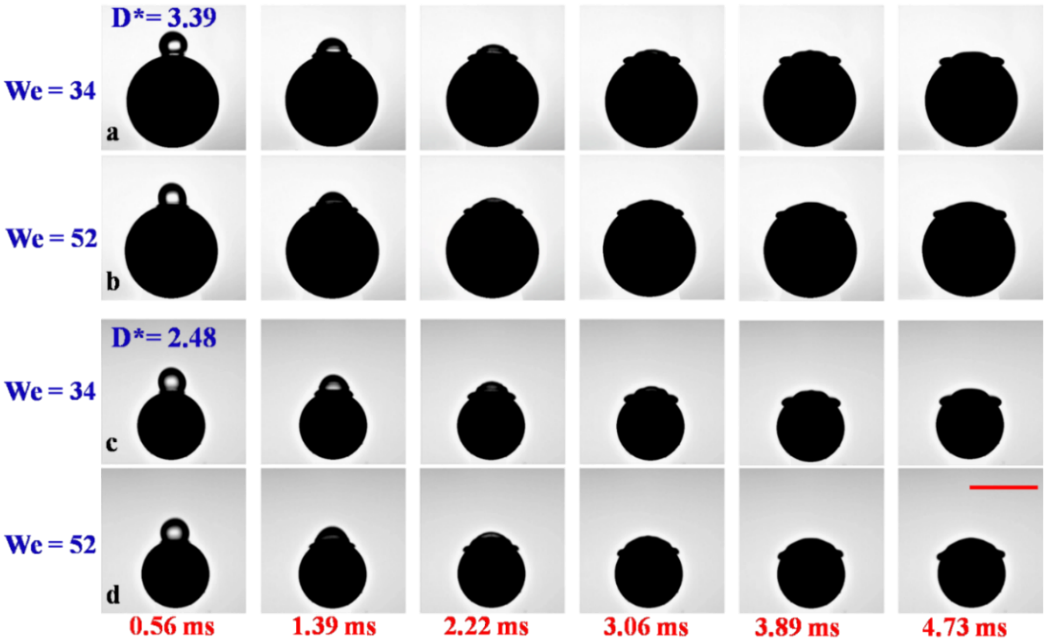

Figure 4.4 Postcollision behavior of droplets on different large hydrophilic spheres at different impact velocities (a) target diameter = 9.5 mm, impact velocity = 0.94 m/s; (b) target diameter = 9.5 mm, impact velocity = 1.17 m/s; (c) target diameter = 6.95 mm, impact velocity = 0.94 m/s; (d) target diameter = 6.95 mm, impact velocity = 1.17 m/s. The associated D^*, impact We and the time frames are mentioned. The scale bar is of 6.95 mm.

It is interesting to note that at $\tau \cong 1$, the spread factor is ~ 2 for all the spheres at $We = 36$, irrespective of the D^* values. During the initial inertial phase of spreading, film flow is opposed by the curvature of the target and the viscous forces. Thus, initially, similar spread factors are observed for all targets, irrespective of curvatures. However, in the later stages, the curvatures of the spheres promote gravity induced spreading, because of which there is significant increase in spread factor for smaller targets owing to the large curvatures. Also, the viscous resistance offered by target surfaces is proportional to their surface area, which is significantly less for smaller targets, therefore promoting more spreading. Figure 4.5 (B) shows a comparison of the spread factors for hydrophilic and superhydrophobic spheres. Similar to figure 4.5 (A), it presents a temporal variation of spread factors for different D^* spheres, but the role of wettability of the target is also included. It is found that although the spread factors for superhydrophobic surfaces is less than its hydrophilic counterparts, the differences are insignificant for lower D^* targets. Hydrophilic surfaces promote more spreading due to higher interfacial energies. However, for spheres of higher D^*, role of wettability is appreciable. This is due to more surface-liquid interaction on larger targets. Insets (a) and (b) of figure 4.5 (B) depict the spreading event on a sphere ($D^* = 0.86$) with hydrophilic and superhydrophobic surface, respectively.

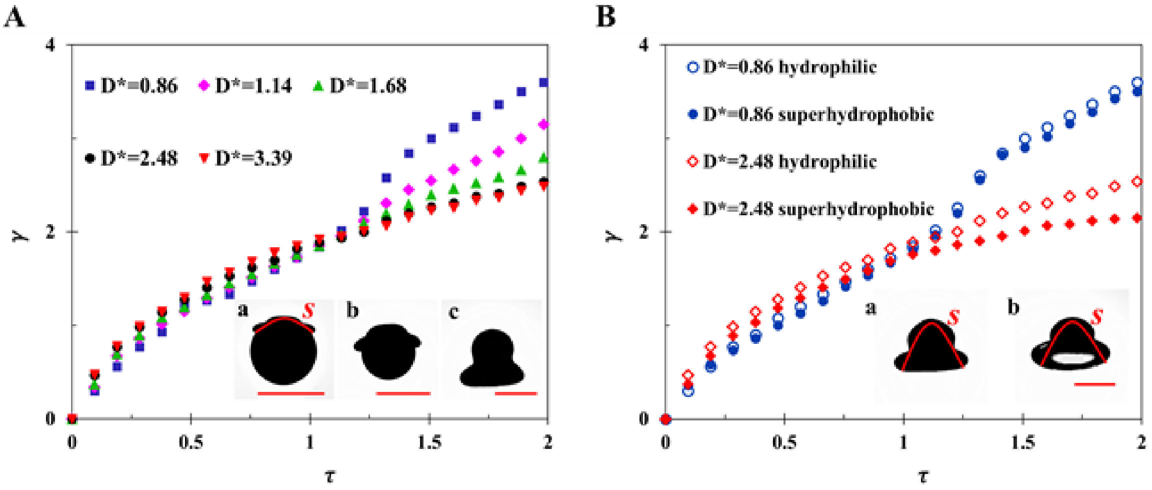

Figure 4.5 (A) Temporal variation of the spreading factor on hydrophilic spheres of different D^* at 0.94 m/s impact velocity ($We = 36$). Inset: Postimpact images at $\tau = 1.98$ for (a) $D^* = 2.48$ (b) $D^* = 1.68$ and (c) $D^* = 0.86$. The magnitude of scale bar is 6.95 mm, 4.7 mm and 2.4 mm, respectively for (a)-(c). (B) Temporal variation of the spreading on spheres of hydrophilic and superhydrophobic surfaces at 0.94 m/s impact velocity ($We = 36$). Inset: Postimpact images at $\tau = 1.603$ for 2.4 mm diameter sphere with (a) hydrophilic and (b) superhydrophobic surface. The magnitude of scale bar is 2.4 mm. The uncertainties associated are within ∓7%.

Figure 4.6 shows the temporal behaviour of another important parameter to quantify film flow dynamics, h^*, the nondimensionalized film thickness at the north-pole of the sphere. It is expressed as $h^* = \frac{h}{D_d}$, where h, is height of liquid column at the north-pole (as shown in the inset of figure 4.6 (A)). The values of h are measured by subtracting the target sphere from the post-impact images using image processing.

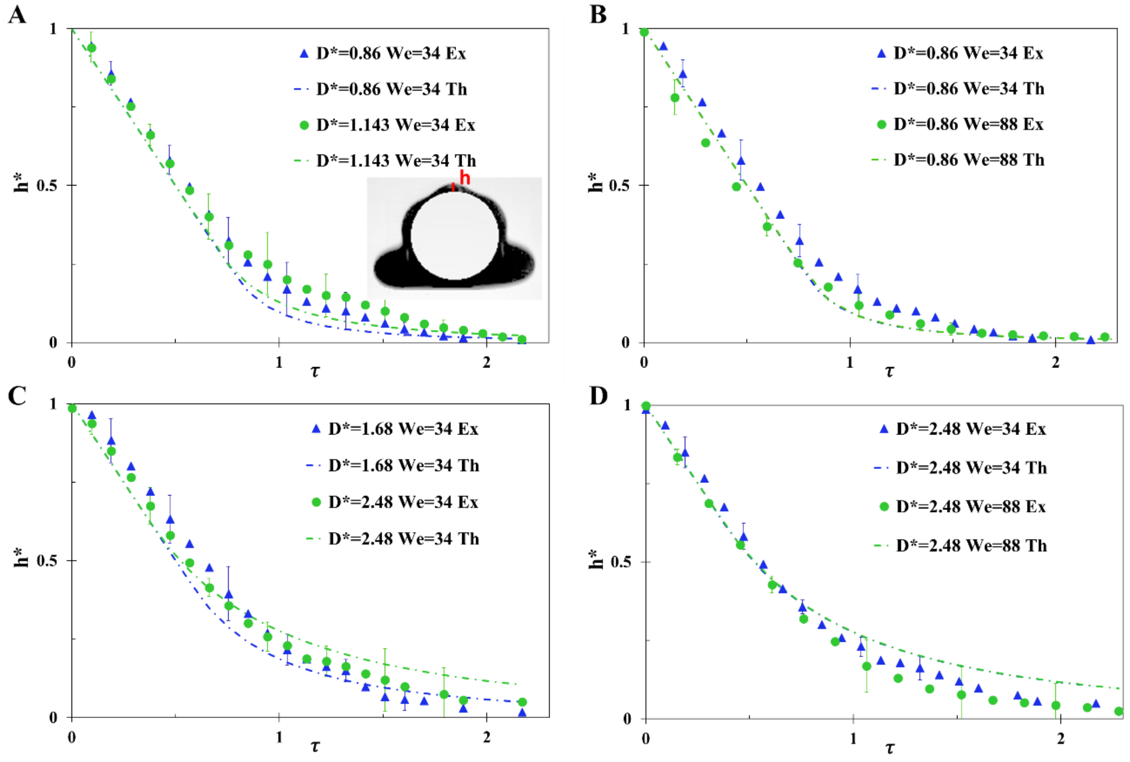

Figure 4.6 Comparison of the experimental data with proposed analytical model [95] for temporal variation of h^* on hydrophilic spheres under the following conditions (A) $D^* = 0.86, We = 34$ and $D^* = 1.143, We = 34$; (B) $D^* = 0.86, We = 34$ and $D^* = 0.86, We = 88$; (C) $D^* = 1.68, We = 34$ and $D^* = 2.48, We = 34$; and (D) $D^* = 2.48, We = 34$ and $D^* = 2.48, We = 88$. The inset shows the liquid film morphology at $\tau = 1.42$ on hydrophilic sphere of $D^* = 0.86$.

In figure 4.6, a sudden decrease in h^* is observed in the region $0 \le \tau \le 0.68$, approximately following the curve $h^* = 1 - \tau$ [95]. During this phase, even as one end of the droplet comes in contact with the sphere, the other end undergoes free fall, and is not influenced by the front end. As time progresses, i.e., during inertial phase of spreading ($0.68 \le \tau \le 2.1$), h^* continues to decrease, but the decrease is less rapid than that in the first stage. Also, dependence of the rate of change of h^* on the D^* is also observed. The experimental values are found in accordance to the analytical model described in literature [95]. Figure 4.6 (A) shows the temporal plots of h^* at $We = 34$ for the spherical targets which are nearly of the same size as the impacting droplet, i.e., D^* are close to 1. It is observed that for the same impact conditions, h^* is higher for larger D^* values. Figure 4.6 (B) shows the dependence of We on h^* for spherical targets which have D^* is close to 1. With increase in inertia of impact, more spreading is produced resulting in a thinner film. Hence, h^* values are lower for higher We. Figures 4.6 (C) and 4.6 (D) depicts similar plots as Fig 4.6 (A) and 4.6 (B), respectively, but for spherical targets having $D^* > 1$. It is also noteworthy to observe that the effect of We on h^* is more pronounced for larger spheres as compared to smaller ones (by comparing figure 4.6 (B) and fig 4.6 (D). Values of h for $\tau > 1.9$ are very small (comparable to size of pixel i.e., 0.26mm) making it difficult to take measurements clearly thereafter. Thus, the data is presented and processed till $\tau = 2$.

4.3.2 Superhydrophobic Surfaces

All the experimental cases have also been conducted on a similar set of SH spheres to understand the effect of wettability. Figure 4.7 shows the front view of postcollisional droplet deformation on SH spheres of $D^* = 0.86$ for three different impacts We. This array is analogous to the array presented in figure 4.2 for hydrophilic spheres with same impact conditions. Comparisons show that in case of SH targets, the droplet does not glide along the target as on hydrophilic surfaces, due to the non-wetting surface behaviour. Instead, the inertia causes the drop to envelope the sphere, and the formation of structures mimicking the Saturnine ring ($We = 34$) or resemblance to a ballerina's tutu ($We = 89$). Also, dark and light fringes are very prominently visible in the SH cases, which shows that capillary instabilities are dominant and the evolving droplet structure near the south-pole is in the form of a liquid sheet. These proto-lamellae structures (image at 3.89 ms in the arrays in figures 4.8 (b) and 4.7 (c)) are visible for spreading on SH targets because these surfaces repel the liquid film from developing along the surface. Figure 4.8 illustrates the top view images of the post-impingement process on hydrophilic and SH spheres of $D^* = 1.68$ at $We = 52$. In general, the top view structures are very similar for both surfaces. However, the rimmed edge formed in case of SH spheres are largely disrupted by visible capillary instabilities, which are generated due to the repulsion of the fluid from the surface.

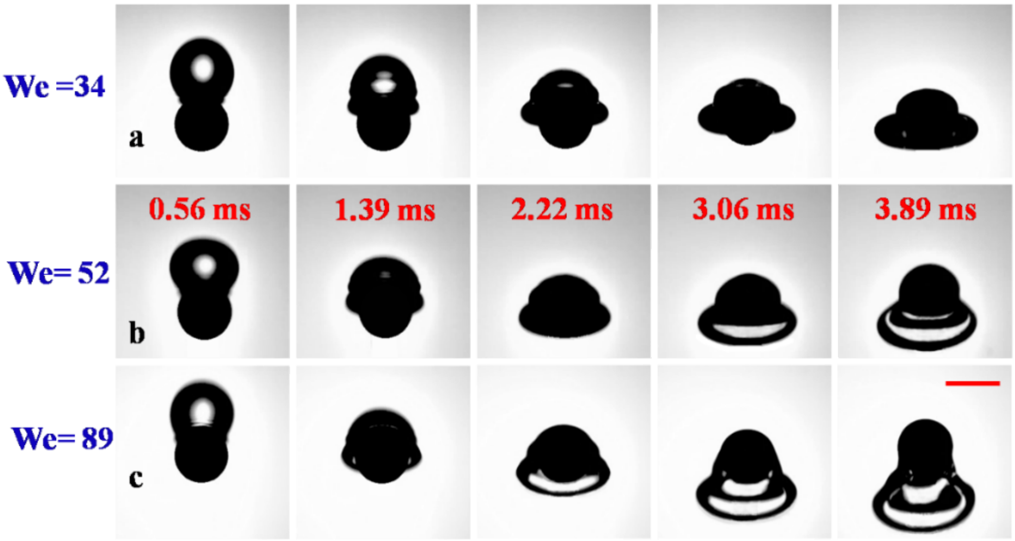
We =34
a
0.56 ms
1.39 ms
2.22 ms
3.06 ms
3.89 ms
We= 52
b
We= 89
c

Figure 4.7 Postcollision deformation (front view) on SH spheres (2.4 mm) at impact velocities (a) 0.94 m/s, (b) 1.17 m/s and (c) 1.5 m/s. The We and time frames have been mentioned. The scale bar (bottom right) is of 2.4 mm. The array illustrates the role of the We.

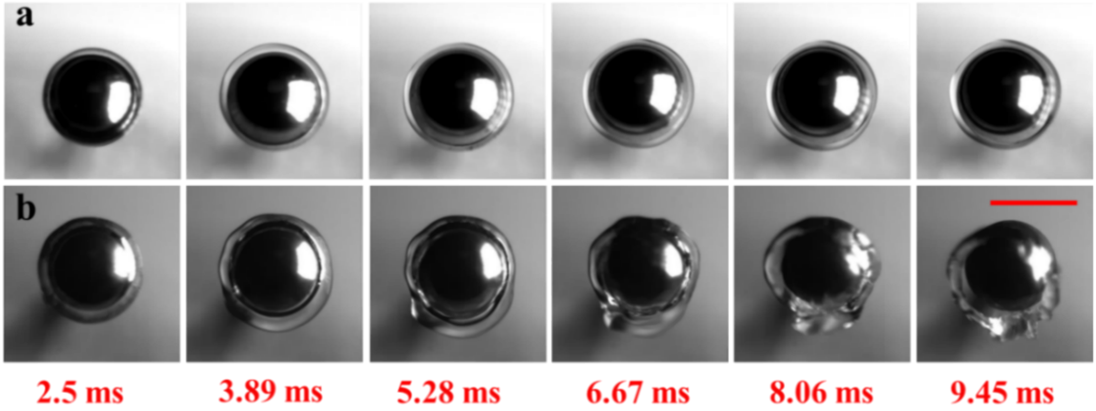
a
b
2.5 ms
3.89 ms
5.28 ms
6.67 ms
8.06 ms
9.45 ms

Figure 4.8 Top view postimpact images for impact velocity 1.17 m/s ($We = 52$) on 4.7 mm diameter spheres with (a) hydrophilic surface (b) SH surface. The scale bar is equal to 4.7 mm.

Figure 4.9 shows the temporal variation of film thickness at the north-pole on SH spheres of various D^* under different impact conditions. This set of plots is similar to those presented in figure 4.6 for hydrophilic surfaces. Figures 4.9 (A) and 4.9 (C) present the effect of D^* on h^* for SH targets for D^* close to 1 and significantly greater than 1, respectively. It is observed that with increasing D^*, the film thickness is slightly increased.

Figure 4.9 (B) presents the effect of the impact We on h^* for SH target having $D^* = 0.86$. With increase in the inertial force, the liquid film becomes thinner, which is similar to what was observed for hydrophilic targets earlier. However, the film does not wet the sphere and shrouds it till the point the wetting repulsion overcomes the inertia and the droplet shatters off the sphere due to capillary instabilities.

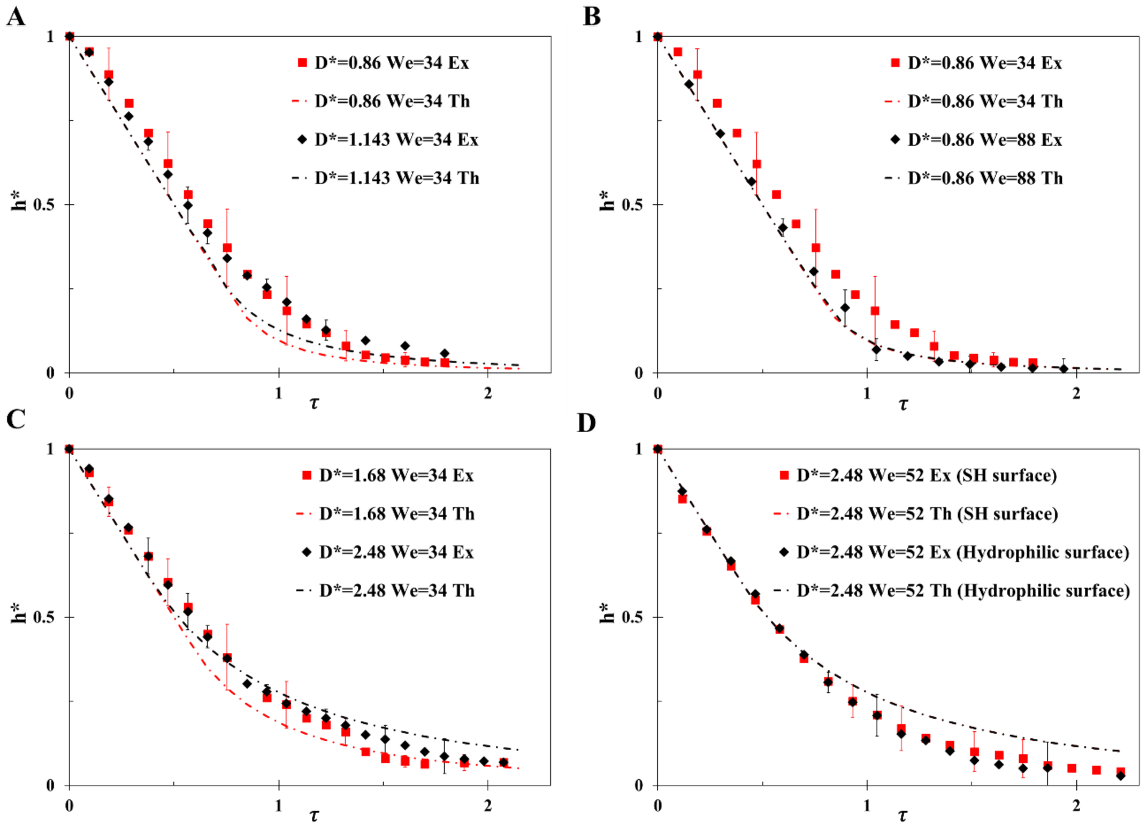

Figure 4.9 Comparison of the experimental data with available analytical model [95] for variation of h^* on spherical targets under the following conditions (A) $D^* = 0.86$, $We = 34$ (SH surface) and $D^* = 1.143$, $We = 34$ (SH surface); (B) $D^* = 0.86$, $We = 34$ (SH surface) and $D^* = 0.86$, $We = 88$ (SH surface); (C) $D^* = 1.68$, $We = 34$ (SH surface) and $D^* = 2.48$, $We = 34$ (SH surface); (D) $D^* = 2.48$, $We = 52$ (SH surface) and $D^* = 2.48$, $We = 52$ (Hydrophilic surface).

Figure 4.9 (D) depicts the wettability effect on h^*. It is noteworthy that h^* does not significantly change in the range $0 \leq \tau \leq 2$ with the wettability of the target, but minute increase is observed for SH targets. In addition, the air film kinetics on the superhydrophobic surface leads the observed hydrodynamics on the spheres. The antiwetting behaviour of the surface leads to entrapment of an air cushion between the droplet and the sphere. On the hydrophilic surface, the film is absent as the droplet wets the surface completely. The air cushion forms a lubricating regime between the droplet and sphere, which leads to the capillary instabilities of the droplet on the superhydrophobic surface (figure 4.8). This observation is in agreement with the slight decrease in the spread factor for SH targets (as seen in figure 4.5 (B)).

4.4 Mathematical Modelling

A model is proposed to determine the maximum spread angle ($2\theta_{inner}$) and ($2\theta_{outer}$) for spheres having D^* close to 1 and D^* significantly greater than 1, respectively. For simplicity, spheres of D^* close to 1 (0.86 and 1.143) are termed as small spheres, whereas, spheres of D^* significantly greater than 1 (1.68, 2.48 and 3.392) are termed as big spheres. The difference in definition of maximum spread angle for big and small spheres is essential as there are gross differences in the morphology of spreading for the two cases. The maximum spread angle has been defined as the angle corresponding to the maximum wetted perimeter of the front view projection of the droplet on the sphere. It is taken from the outer end of the rim for big spheres and from the inner end for the small spheres.

Figure 4.10 (a) depicts the schematic of the droplet on the spherical target, attained the maximum spreading state. $(2\theta_{inner})$ and $(2\theta_{outer})$ are indicated on the illustration. Figure 4.10 (b) and 4.10 (c) show the side and top view images at the maximum spread moment on hydrophilic sphere of $D^* = 1.68$ at $We = 34$. The diameter of the toroidal rim is represented as $2r$. Figure 4.10 (d) and 4.10 (e) are similar images on hydrophilic spheres of $D^* = 0.86$. The toroidal rim is thicker for small spheres than for larger ones. For small spheres the droplet fully engulfs the target sphere, whereas a hat structure is formed on big spheres, and hence the maximum spread angle is expressed differently for the two cases.

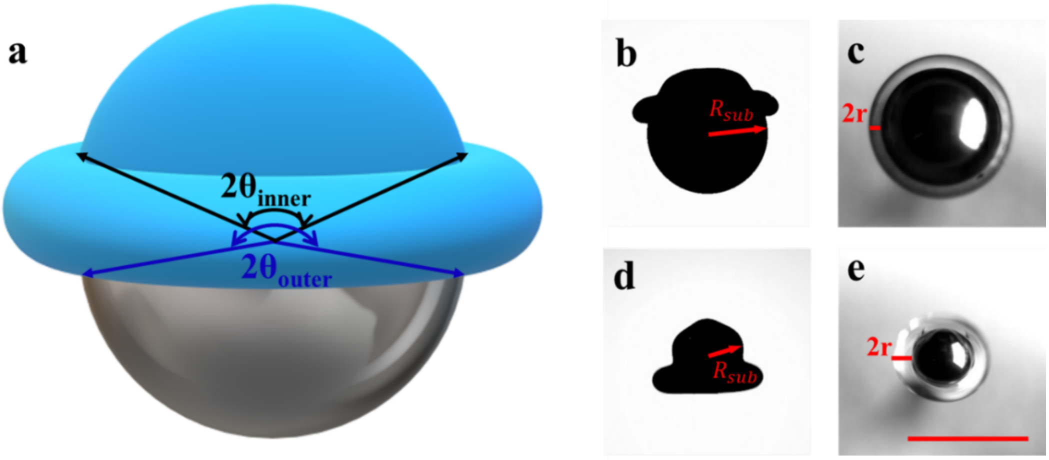

Figure 4.10 (a) Schematic depicting maximum spread angle ($2\theta_{outer}$ and $2\theta_{inner}$) for big and small spheres. (b) and (c) are the side and top view images for hydrophilic spheres ($D^* = 1.68$) at maximum spread ($We = 34$). (d) and (e) are same for $D^* = 0.86$ ($We = 34$). The magnitude of scale bar is 4.7 mm.

From energy balance principle, total energy before and after impact is conserved and is expressed as [60]

$$k.e_i + s.e_i = s.e_1 + s.e_2 + s.e_3 + s.e_4 + v_{dis} \tag{4.1}$$

The change in potential energy is neglected in equation (4.1) as it is small compared to other energy components during spreading on a millimeter scale sphere [113,118].

The kinetic energy before impact is expressed as [113]

$$k.e_i = \frac{1}{2}\left(\rho U^2\right)\left(\frac{\pi D_d^3}{6}\right) \tag{4.2}$$

The droplet is assumed to initially have a spherical shape (experiments show that this is true, however, small shape distortions are possible, which are neglected). The surface energy of the droplet before the impact is [113]

$$s.e_i = \pi D_d^2 \sigma_{lg} \tag{4.3}$$

After impact, at the maximum spread state, three interfacial areas are present: the bottom surface area (A_b), top surface area, and rim surface area (A_r). It is assumed that the bottom and top surface areas are almost equal as the film thickness is very less as compared to the radius of the spheres. The expressions of these interfacial areas are represented as [113]

$$A_b = 2\pi R_{sub}^2(1 - \cos cos\,\theta) \tag{4.4}$$

where θ represents half of the maximum spread angle ($2\theta_{outer}$ or $2\theta_{inner}$) [113]

$$A_r = 2\pi R_{sub} \sin sin\,\theta\, t_f \tag{4.5}$$

where the film thickness is deduced as follows

$$t_f = \frac{1}{A_b}\left(\frac{\pi D_d^3}{6}\right) \tag{4.6}$$

The net energy at maximum spread is a sum of the different surface energy components and the viscous dissipation work done by the droplet while spreading against the surface.

The viscous dissipation work is expressed as [61]

$$v_{dis} = \int_{0}^{t_c} \int_{V} \psi \, dV dt \tag{4.7}$$

The dissipation function ψ can be expressed as a function of the impact velocity and the boundary layer thickness δ during spreading can be expressed as [61]

$$\psi \approx \mu \left(\frac{U}{\delta} \right)^2 \tag{4.8}$$

The value of δ is estimated from the similarity solution for the boundary layer flow, assuming a case where the axial momentum is converted into a radial flow. δ is expressed as [113]

$$\delta = \frac{2D_d}{\sqrt{Re}} \tag{4.9}$$

The effective volume of the liquid under the action of the viscous dissipative work can be expressed as

$$V_{dis} = A_b \delta \tag{4.10}$$

The time required to reach the maximum spreading state is scaled as [113]

$$t_{spread} \sim \frac{R_{sub} 2\theta}{U} \tag{4.11}$$

Therefore, viscous dissipation work (from equation 4.7) is finally of the form

$$v_{dis} = \mu\left(\frac{U}{\delta}\right)A_b R_{sub} 2\theta \tag{4.12}$$

The postimpact surface energy component $s.e_{f1}$ is expressed as

$$s.e_{f1} = \left(A_b + A_r\right)\sigma_{lg} + A_b\sigma_{sl} - A_b\sigma_{sg} \tag{4.13}$$

The volume of the spherical cap is

$$V_{SphCap} = \pi R_{sub}^2 (2 + \cos cos\,\theta\,)(1 - \cos cos\,\theta)^2 t_f$$

(4.14)

The volume of the toroidal rim (refer figures 4.10 (c) and 4.10 (d)) is found by subtracting the spherical cap volume from the total droplet volume as

$$V_{toroid} = \frac{\pi}{6}D_d^3 - V_{SphCap} \tag{4.15}$$

Again, it can also be expressed as

$$V_{toroid} = 2\pi^2 r^2 [R_{sub} + 2r] \tag{4.16}$$

where r is the radius of the toroidal rim (refer figures 4.10 (c) and 4.10 (e)). Equations 4.15 and 4.16 are equated to determine the expression for r. The other component of postimpact surface energy, $s.e_{f2}$, is expressed as

$$s.e_{f2} = 4r\pi^2 (R_{sub} + 2r)\sigma_{lg} \tag{4.17}$$

Substituting all the energy components in equation 4.1, the net energy conservation equation at the moment of maximum spreading is of the form

$$\frac{1}{2}\left(\rho U^{2}\right)\left(\frac{\pi D_{d}^{3}}{6}\right)+\pi D_{d}^{2}\sigma_{lg}=\mu 4\pi\theta R_{sub}^{3}\left(\frac{U}{\delta}\right)(1-\cos cos\,\theta)+2\pi R_{sub}\left[R_{sub}(1-\cos cos\,\theta)+t_{f}\ s\right.$$

(4.18)

Nondimensionalizing by the initial surface energy of the droplet, the relationship between the half maximum spreading angle is obtained in terms of We, Re, and Ca as

$$\frac{We}{12}+1=Ca\sqrt{Re}\frac{D^{*3}}{4}\theta(1-\cos cos\,\theta)+\frac{(1-\cos cos\,\theta)D^{*2}}{2}+\frac{\sin sin\,\theta}{3D^{*}(1-\cos cos\,\theta)}-\frac{\cos cos\,\theta\,(1-\cos cos\,\theta)D^{*2}}{2}$$

(4.19)

where $d^{*}=\frac{2r}{D_{d}}$

The last term of equation 4.19 is neglected in case of big spheres as the value of r is very small in such cases, i.e., the radius of the circular section of torroid is negligible. It is only accounted for the small spheres. While calculating $2\theta_{outer}$, the term $\pi d^{*}(D^{*}+2d^{*})$ is not considered. Whereas, while calculating $2\theta_{inner}$, the solution is presented for small spheres and all the terms are considered. This is mainly due to the structural difference of the lamella formed on big and small spheres. Figure 4.11 (A) illustrates the comparison of experimental and theoretical values of maximum spread angle ($2\theta_{outer}$) for large spheres (D^{*} values of 1.68, 2.48 and 3.39) for three different impacts We. Fig 4.11 (B) presents the same ($2\theta_{inner}$) for small spheres (D^{*} values of 0.86, 1.14 and 1.68).

It is clearly presented by figure 4.11 (A) and (B) that by keeping the impact We value constant, an increase in target size leads to less spread angles. It is due to more shear provided by the bigger targets than smaller ones hence less energy left for spreading the droplet. Also, it is of notice that by keeping the target size constant, on increasing We, more kinetic energy is available for spreading therefore the spreading angles increase for each case. It is noteworthy that $D^{*}=1.68$ is presented for both $2\theta_{outer}$ and $2\theta_{inner}$ cases and is found to conform to both the model approaches. Hence this value of D^{*} has been considered as the transition value for the mathematical formulation, for which both the big and small spheres are in agreement, and the last term in equation 4.19 may and may not be neglected. It is observed that in general, the model performs better for SH surfaces than for hydrophilic surfaces. The SH surfaces impart less maximum spread angle than their hydrophilic counterparts due to higher σ_{sl} values. Also, frictional resistance to wetting on the hydrophilic surfaces lead to additional errors which are not captured by the present model. Also, for $D^* = 1.68$, the formulation for small spheres performs slightly better than for big spheres.

4.5 Closure

Postimpact hydrodynamics of water droplets on spherical targets of different sizes and wettability is investigated experimentally in this article. This chapter involves the discussion on droplet spreading and lamella formation on the spherical substrates under different impact conditions. These behaviors are analyzed in detail using high speed photography. Both the side and top views have been captured. Three geometric parameters namely, spread factor, liquid film thickness at the north pole and maximum spread angle are defined and examined. It is observed that spread factor is more for smaller spherical targets and it does not significantly change for different wettable surfaces. It is also observed that the liquid film thickness at the north pole is higher for bigger diameter spherical surfaces and decreases when the impact Weber number is increased. Similar to the spread factor, the wettability does not affect it significantly although a minute increase is seen for SH surfaces. Moreover, maximum spread angle values are higher for smaller spherical substrates. It is also found to increase with increasing wettability of the substrate. The study also proposes a theoretical model to predict the values of maximum spread angle. The model predictions are found to be in agreement with the experimental results. The findings may be of importance to spraying and coating technology of complicated curved surfaces and morphologies.

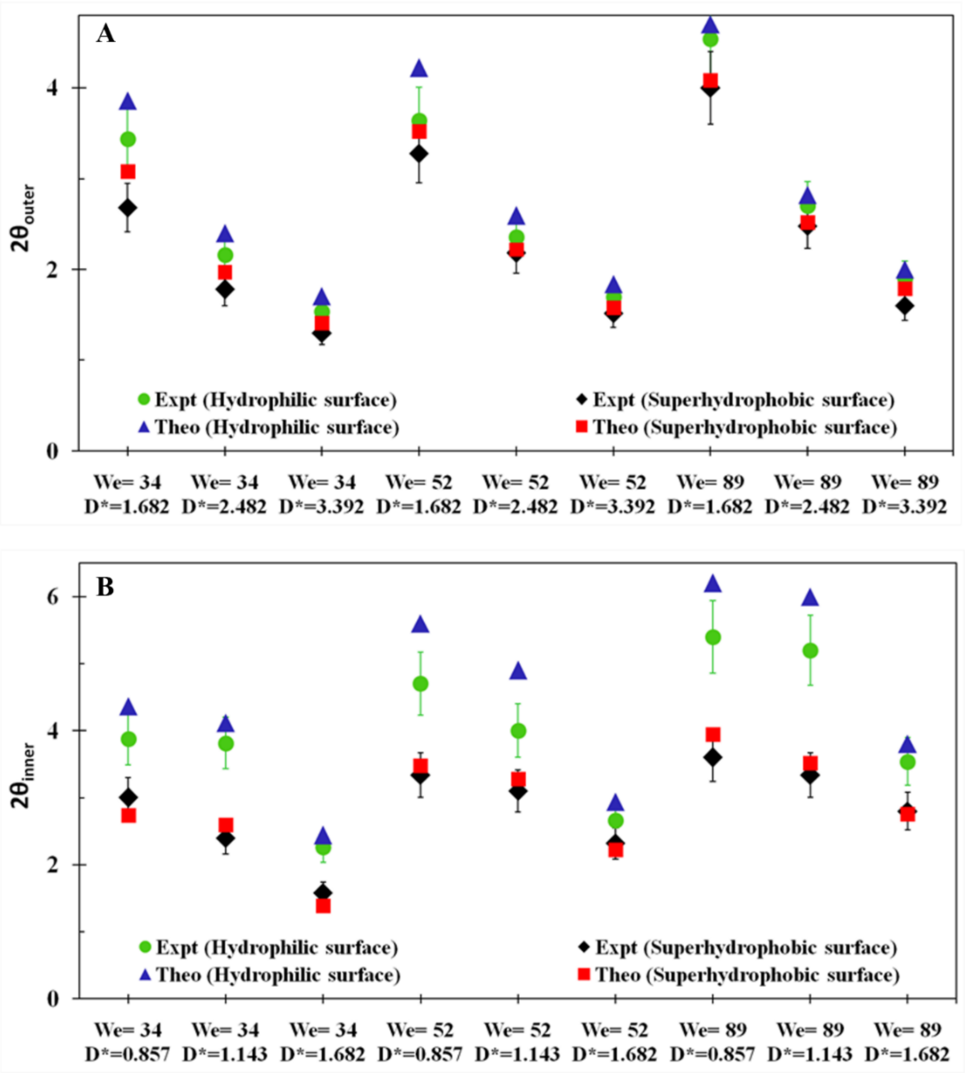

Figure 4.11 Comparison of experimental and theoretical values of maximum spread angle for various impact conditions on hydrophilic and SH (a) big spheres (b) small spheres

Chapter 5

Droplet Collision and Jet Evolution Hydrodynamics in Valley Configurations

---

5.1 Introduction

The hydrodynamics of droplet impact on a two-phase interface has caught the attention of many researchers over past few decades. Experimentally understanding the rich fluid dynamics of droplet impact on surfaces having complex geometrical shapes and topologies could have far-reaching implications in micro and macroscale systems [1-5]. In spite of its varied applications, very few studies are available on the topic of droplet impaction on concave surfaces [104,123]. The present chapter aims to unravel the interesting phenomenon of droplet impact hydrodynamics on "V" shaped grooves of variant wettability and geometric dimensions. The groove geometry makes the hydrodynamics three-dimensional, as in addition to the droplet dynamics in the lateral direction, liquid jets are generated from the postimpact droplet along the axial direction of the groove. The effect of impact Weber number on the jet velocity, the non-dimensional the spreading width and the non-dimensional south-pole liquid film thickness has been studied temporally and theoretically. Moreover, a semi-analytical formalism has been proposed to predict the jet velocity evolution in terms of governing Weber (We) and capillary (Ca) numbers.

5.2 Experimental Techniques

Schematic of the experimental setup has been shown in figure 5.1 (A). Droplets are generated using a 250-µl chromatography glass syringe (attached to a 22-gauge stainless steel needle). Droplet dispensing is achieved and controlled by a precision droplet dispenser mechanism, with a least count of 0.1 µl. Droplet diameter (~ 2.8 mm within ± 5% accuracy) is measured by dispensing a fixed liquid volume, and is later verified using image processing of the spherical droplet just before impact. Different impact velocities (~ 0.95 m/s, ~ 1.17 m/s, ~ 1.5 m/s, within ±5% accuracy) were obtained by adjusting the height of the dispensing unit and allowing the droplets to free-fall from the needle. The impact velocity is calculated by applying the energy balance principle between the point of release and the point of impact, neglecting the work done against the atmospheric air. A high-speed camera (Photon, UK), with a G-type AF-S constant focal length (105 mm) macro lens (Nikkor, Nikon) is used to capture the images during the experiments. The images are captured at 3600 frames per second, at 1024 x 1024 pixels resolution. Both the front and top views of the droplet impact dynamics is captured. For the front views (refer figure 5.1 (A)) the camera is placed coaxial to the groove, while for the top view it is placed vertically orthogonal to the plane of the groove. A brightness controlled white LED (light emitting diode) array (Holmarc Opto-Mechatronics, India) is used for backlight illumination.

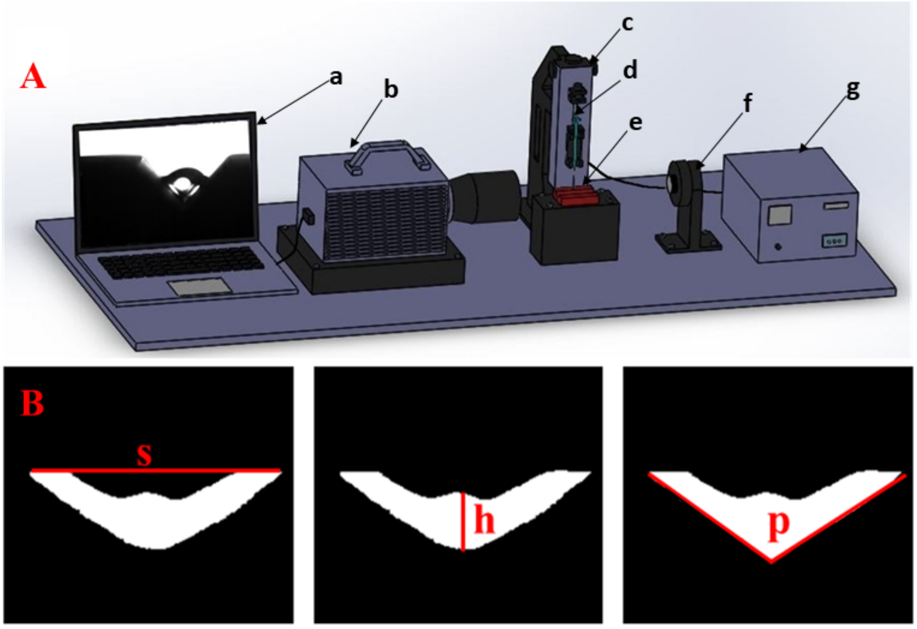

Figure 5.1 (A) Schematic of the experimental setup (a) data acquisition computer system, showing the front view of a typical "V" groove with droplet impact (b) high speed camera (c) precision droplet dispenser (d) chromatography glass micro-syringe with a stainless-steel needle (e) substrate ("V" groove or valley configuration) (f) backlight illumination source (g) droplet dispensing and backlight illuminating system controller. (B) Illustration of transient spreading parameters used in the analyses (white region represents the liquid droplet): (a) spreading width (b) south-pole height (c) wetting perimeter along the groove walls.

Deionized water droplets are used as test fluids, and are dropped vertically downward from the dispenser precisely on the axis of the stainless-steel "V" grooves of different width to depth ratios (refer table 5.1 for "V" groove dimensions and inset of figure 5.5 (a) for its schematic representation). Experiments are performed on both hydrophilic surfaces and SHS. The hydrophilic substrate is prepared by cleaning the stainless-steel grooves with acetone and then drying in hot air oven. The same set of substrates is coated with a commercial superhydrophobic chemical spray (Ultra Tech International, Inc., USA) for the SHS. Each experimental case has been repeated thrice and at randomly chosen axial position of the groove to check for replicability in the results. All experiments were done at temperature of $27^0 \pm 3^0$ and relative humidity (RH) of 55% ± 5%. The parameters that have been analyzed are presented in figure 5.1 (B). Evolution of the spreading width, south-pole height, and axial jet has been quantified using the open-source image processing software ImageJ. We have presented the images of the droplet hydrodynamics using inverted binary color scheme. The fluid region is represented by white pixels while the air and solid regions are represented by black pixels. A red line has been used to demarcate the side walls of the "V" grooves in all the figures. Table 5.2 shows the surface tension or surface energy per unit area for the solid-liquid (σ_{sl}) and liquid-gas (σ_{lg}) interfaces of the stainless steel (which is used as the hydrophilic substrate) and the SHS.

Table 5.1 Dimensions of the "V" grooves. '*D*' represents the width and '*H*' represents the depth of the groove (refer inset of figure 5.5 (a) for the schematic representation).

Sl. No.	***D* (mm)**	***H* (mm)**
1.	1	2
2.	1	4
3.	1.5	4
4.	2	4
5.	1	6
6.	2	6

Table 5.2 Surfaces tensions for the liquid-gas and solid-gas interfaces and static contact angle for the flat surfaces. [112]

Target Substrate	**σ_{sl} (J/m^2)**	**σ_{lg} (J/m^2)**	**Contact angle (θ_c)**
Stainless steel	0.18	0.0728	$45^o \pm 3^o$
SHS	0.2726	0.0728	$135^o \pm 3^o$

5.3 Results and Discussion

In the post-impact droplet hydrodynamics, spreading width, wetting perimeter and north-pole height of the liquid (as shown in the figure 5.1 (B)) are the considered parameters of interest. In addition, axial jetting of the liquid droplet (as visible from the top views presented in figure 5.7) becomes significant in the cases of droplet impact on such grooves or valleys. Parameters like spreading width, and north-pole height of the post-impact liquid droplet, and the groove dimensions are non-dimensionalized using the droplet diameter before impact. In the initial part of this section, experimental results for the variation of non-dimensional spreading width (γ), and non-dimensional north-pole height (h^*) is plotted against non-dimensional time ($\tau = \frac{tV}{D_d}$, where t = instantaneous time, V= droplet impact velocity, and D_d= droplet diameter before impact) for both hydrophilic surfaces and SHS. In the later part of the paper, we discuss the transient hydrodynamics of the jets formed along the length of the grooves. An analytical model relating the axial jet velocity to the transverse spreading parameters and the governing non-dimensional numbers, is proposed.

Non-dimensional numbers governing the post-impact dynamics are Weber number (We), Capillary number (Ca), and Reynolds number (Re) (expressed as $We = \frac{\rho V^2 D_d}{\sigma_{lg}}$, $Ca = \frac{\mu V}{\sigma_{lg}}$, and $Re = \frac{\rho V D_d}{\mu}$ where ρ = density of the liquid droplet, σ_{lg} = surface tension for the liquid-air interface, μ = dynamic viscosity of the liquid).

5.3.1 Hydrophilic Surfaces

The post-impact structural evolution of the droplets depends on the impact We and the morphology of the target groove [124]. Individual effects of each of these parameters on the post-impact hydrodynamics on the hydrophilic (HP) groove have been discussed. The temporal evolution of the droplet (as visible from the front view of the grooves) is illustrated in figure 5.2, for the same groove and three different We. The structure of the droplet changes from the initial spherical to a flying bird-like shape as time evolves. While the region of the spreading droplet outside the groove region spreads similar to that on a flat surface, but the dynamics of the liquid in the region of the groove is morphed. It is noted from figure 5.2 that with the increase in impact We, the extent of spreading increases, and the height of liquid layer at any position within the groove decreases. The reason for the same is attributed to the larger kinetic energy at the instants of impact for the higher We.

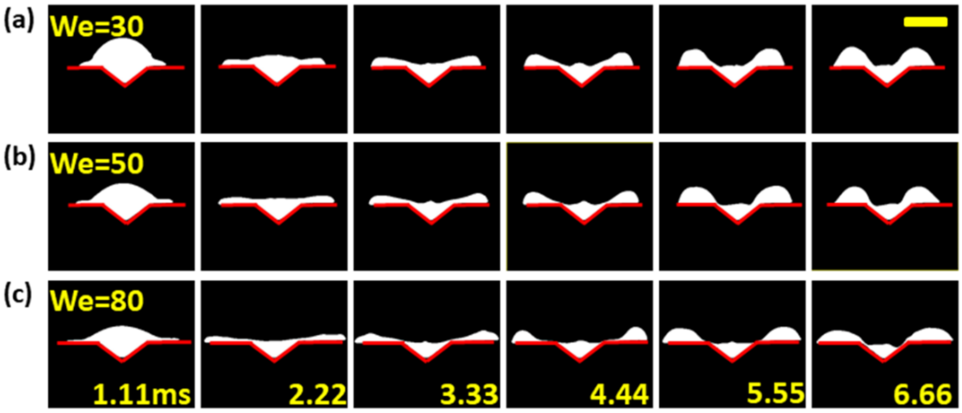

Figure 5.2 Temporal evolution of the post-impact droplet (front view) on the "V" groove with D^* = 0.8 and H^* = 0.4 for three different We, (a) We = 30, (b) = 50, and (c) = 80. Scale bar shown in the top right corner represents 1.85 mm and is same for all the images. The red line indicates the shape of the groove.

Also, the rate of spreading is higher for the impact with higher We due to the same reason. While the mass of liquid outside the groove is pinned during the end of the spreading phase, the mass of liquid within the groove is still spreading. The recoiling fluid outside the groove interacts with the still-spreading fluid within the groove zone. This leads to the formation of a distinct fluid ridge at the liquid-air interface, located vertically above the apex of the groove (figure 5.2 (a)-5.2 (c), at 4.44 ms). In addition, the recoiling fluid from outside the groove, and the spreading fluid from within the groove region led to the formation of unnaturally large liquid rims on either side of the groove (figure 5.2 (a)- 5.2 (c) at 6.66 ms).

Figure 5.3 and 5.4 illustrates the influence of the geometry of the "V" groves or valleys on the post-impact behavior. Three grooves of different depth (H^*) but same width (D^*) has been considered for figure 5.3, and the effect of different groove width keeping the groove depth fixed has been presented in figure 5.4.

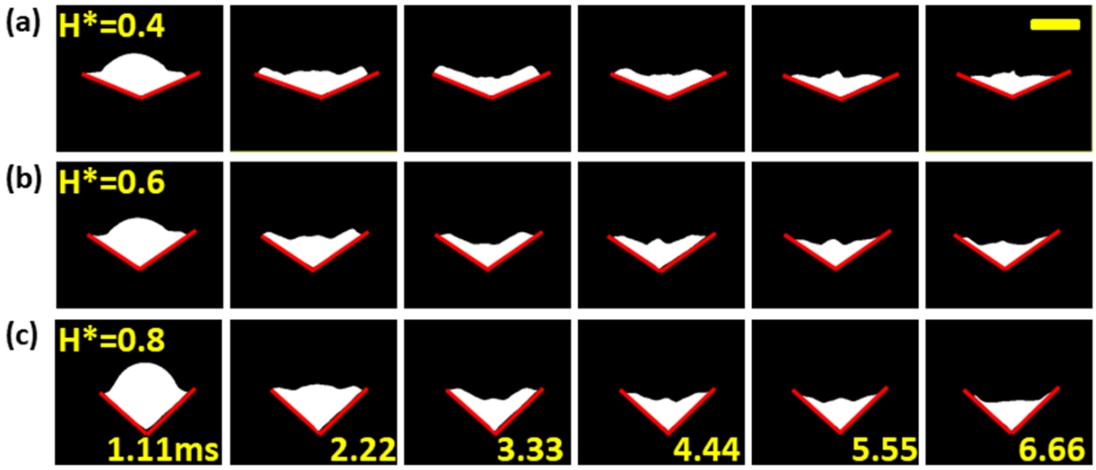

Figure 5.3 Temporal evolution of the post-impact droplet (front view) for We = 30 on grooves with fixed D^* = 1.6 and three different H^*, (a) H^* = 0.4, (b) H^* = 0.6, and (c) H^* = 0.8. The scale bar shown in the top right corner represents 1.7 mm length and is same for all the images.

As the depth of the groove increases at same width, the steepness of the inclined walls increases. Consequently, despite impact at same We, the droplet is unable to spread outwards in deeper grooves. The retraction due to the inclined walls leads to inertia-capillary instabilities on the liquid-air interface, with distinct wave patterns visible. It is noteworthy that the volume of the droplet reduces in each case as the hydrodynamics is also associated with jetting along the groove length (axial spreading). Additionally, due to higher resistance to the flow in the transverse direction for the steeper grooves, the spreading width of the liquid layer decreases with the increase in the steepness of the groove. As seen in figure 5.2 and figure 5.4 (a), owing to the smaller dimensions of the groove, the liquid droplet spreads outside the groove region, forming a bird-like structure a typical to droplets spreading on flat surfaces.

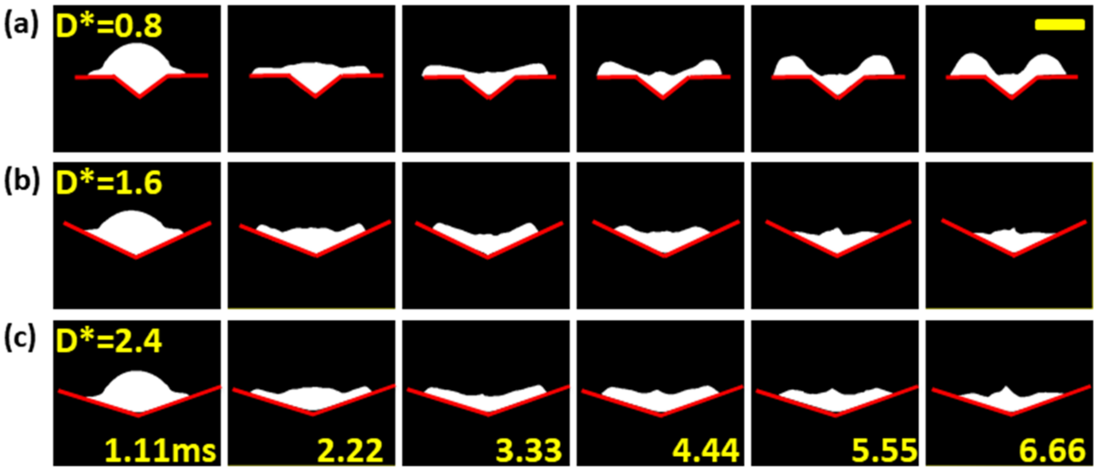

Figure 5.4 Temporal evolution of the post-impact droplet (front view) for $We = 30$ on grooves with fixed $H^{*} = 0.4$, and three different D^{*}, (a) $D^{*} = 0.8$, (b) $D^{*} = 1.6$, and (c) $D^{*} = 2.4$. The scale bar shown in the top right corner represents 1.85 mm length and is same for all the images.

Evolution of the non-dimensional height at south-pole and the spreading width with the non-dimensional time is shown for different combinations of impact Weber number and groove dimensions in figure 5.5 (wettability is same for all the cases). It is evident from figure 5.5 (a) that the height of the liquid layer at the south-pole (for all the cases) first decreases to a minimum value (due to lateral spreading), then increases by a small margin (due to contact line retraction induced backflow) and finally saturates.

It is also noted from the plot that the non-dimensional south-pole film thickness steeps and saturates at lower values for higher impact Weber number cases. For the same groove, the south-pole height of the liquid layer reaches its minima earlier for the lower impact Weber number, as due to the lower initial kinetic energy, the surface tension forces balance the inertial forces in comparatively lesser time.

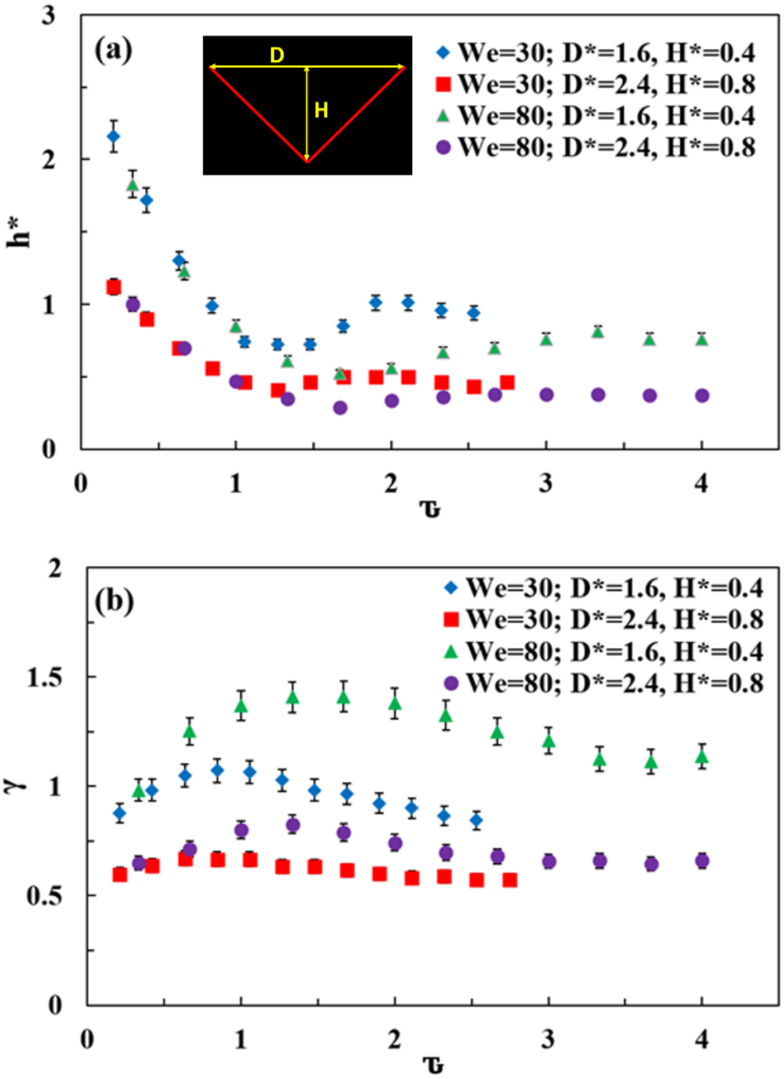

Figure 5.5 Variation of (a) non-dimensional south-pole height (h^*) and (b) non-dimensional spreading width (γ) with non-dimensional time (τ) for different grooves and impact We for same hydrophilic substrates.

Interestingly, even during the very initial phase of contact ($\tau < 1$), the surface geometry influences the spreading characteristics profoundly. Such trend is as the steepness of the groove (i.e., the relative magnitude of depth with respect to width of the groove) increases, the resistance to the lateral spreading also increases due to the wall reaction forces. For the same impact Weber number, the spreading width of the post-impingement liquid droplet is observed to be lower for the steeper groove (groove with $D^* = 2.4$ and $H^* = 0.8$ is steeper than groove with $D^* = 1.6$ and $H^* = 0.4$). It is interesting to observe that the point of maxima for the spreading width (figure 5.5 (b)) is attained earlier than the point of minima for the north-pole height of the liquid layer. Also, the rate of reduction of the south-pole height before reaching its minimum value is far more than the rate of increment of the spreading width before reaching its maximum value (figure 5.5 (b)). The reason behind these apparent anomalous observations is the formation of liquid jets in the axial direction of the groove (discussed in details in section 5.3.3).

5.3.2 Superhydrophobic Surfaces

In the previous segment, the analysis was based on the effect of the Weber number and the groove dimensions. In addition, the wettability of the groove surface is also noted to be a governing parameter, and we discuss this in this segment. Figure 5.6 compares the post-impact droplet dynamics on the hydrophilic and the superhydrophobic grooves at two different impact Weber numbers. At the lower impact Weber number, the liquid droplet partially de-wets off the surface for the superhydrophobic substrate (figure 5.6 (b), last column). At higher impact Weber numbers, the high inertia causes higher spreading; which is followed by rapid recoil due to the non-wetting surface behavior. Consequently, the spread region of the droplet breaks off due to capillary instability, and breaks up into daughter droplets ejecting away from the regions outside the groove (figure 5.6 (d), last column). Thus, unlike a flat SH surface (where rebound is vertical with droplet intact), the groove SH surface induces break-up and diverted rebound of the droplet.

Variation of the non-dimensional south-pole height of the liquid layer with the non-dimensional time for two different grooves at two different impact Weber number has been compared for the hydrophilic and the superhydrophobic surfaces in figure 5.7. Before reaching its minimum value, variation of h^* follows similar trends for both the wettability conditions and at both the impact Weber numbers. But for the superhydrophobic surfaces, there is a retraction in the curve of h^*, whereas the curve for the hydrophilic surfaces remains unchanged after reaching their minimum values.

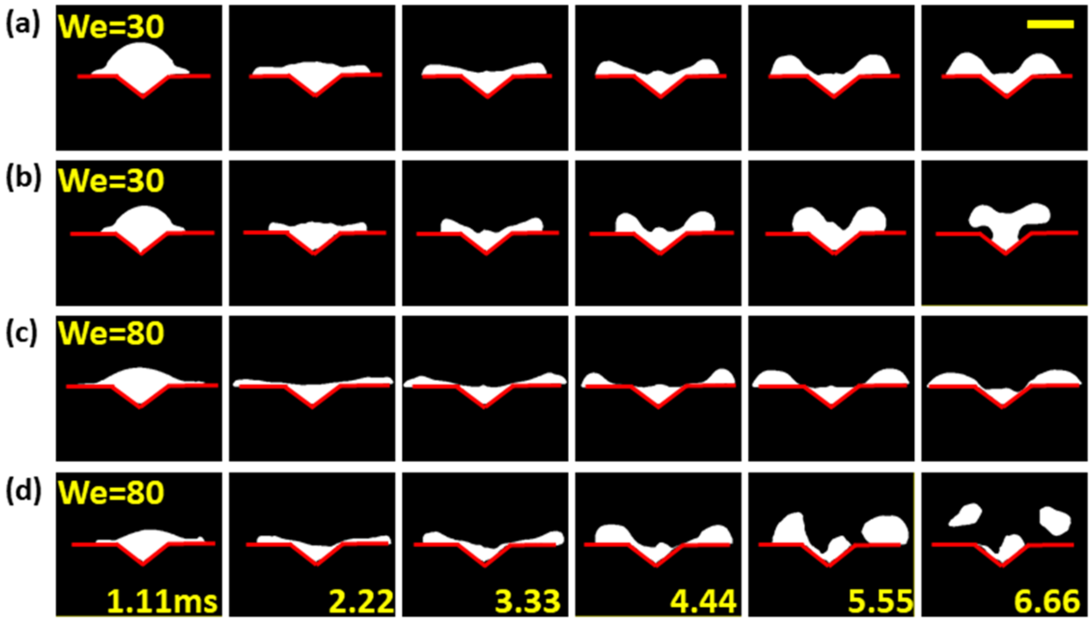

Figure 5.6 Temporal evolution of the post-impact droplet (front view) on a groove ($D^* = 0.8$ and $H^* = 0.4$) for two different combinations of impact We and wettability. (a) We =30; hydrophilic (HP) surface (b) We = 30; SHS (c) We = 80; HP surface (d) We = 80; SHS. The scale bar at the top right corner represents 1.85 mm and is same for all the images.

The extent of the retraction of the south-pole height of the liquid layer is more for the lower impact Weber number as at the higher impact Weber number, post-impact dynamics of the droplet is dominated by the inertial forces. The higher surface energy of the solid-liquid interface for the superhydrophobic surfaces leads to the breakage of the liquid droplet into the daughter droplets at the higher impact Weber number (figure 5.6 (d)), leading to reduction in liquid mass available for increase in the central bulge.

Figure 5.8 highlights the effect of the wettability on the temporal evolution of the non-dimensional spreading width of the liquid layer (for two different grooves at two different impact conditions). The trends of the spreading width (γ) for both the grooves at lower impact Weber number ($We=30$) coincides before attaining maxima irrespective of the wettability of the surfaces. But post-maxima, a strong recoiling is observed for the SH substrate while there is no significant reduction in the spreading width (γ) for the HP substrate. Contrary to this, at higher impact Weber number ($We = 80$) spreading width (γ) for the SH substrate is slightly higher than the HP substrate before attaining maxima, but afterwards the effect of wettability is not at all significant. Before attaining the maxima, the tendency of the droplet is to spread due to the inertial energy and lower wettability of the SH surface provides lesser resistance to the flow. Therefore, for the higher impact Weber number droplets spread more smoothly on the SH surfaces due to the dominancy of the inertial forces. After maximum spreading, recoiling forces due to wettability on the SH substrate is not able to overcome the inertial forces at higher impact Weber number and trends for both the HP and the SH substrates coincides.

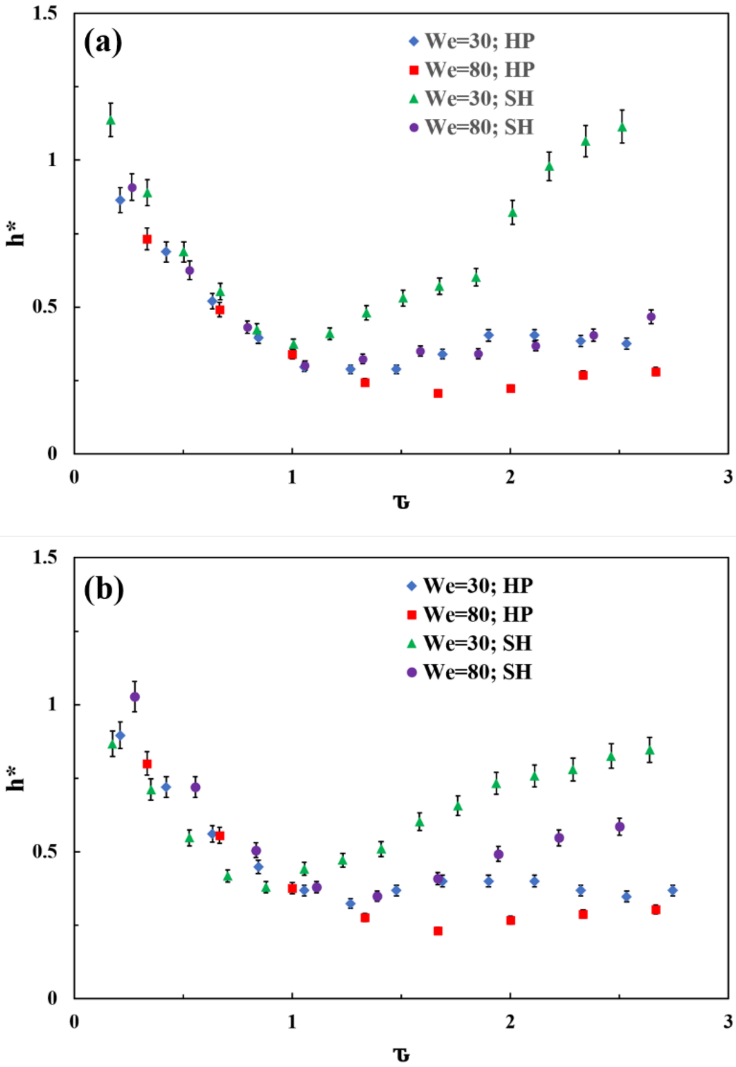

Figure 5.7 Variation of the non-dimensional height of post-impact droplet at the north-pole with the non-dimensional time on the both HP and SH grooves with dimensions (a) $D^* = 1.6$; $H^* = 0.4$ (b) $D^* = 2.4$; $H^* = 0.8$.

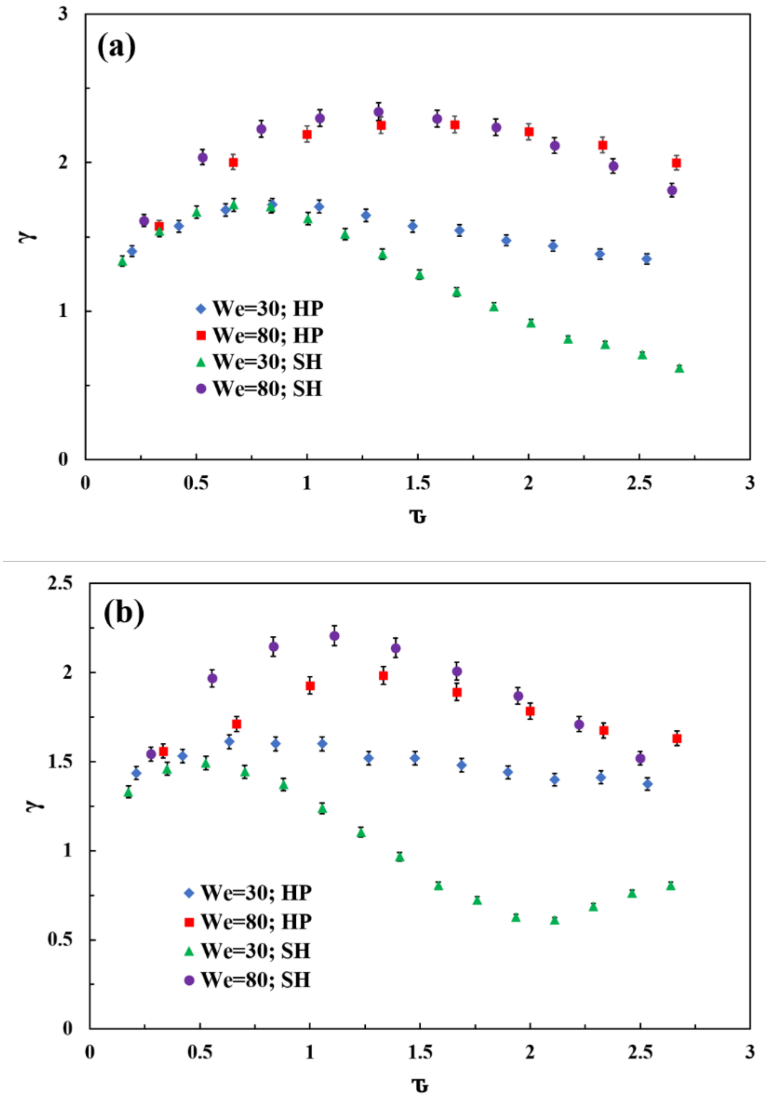

Figure 5.8 Variation of the non-dimensional spreading width of the post-impact droplet with the non-dimensional time on both HP and SHS grooves with dimensions (a) $D^* = 1.6$; $H^* = 0.4$ (b) $D^* = 2.4$; $H^* = 0.8$.

5.3.3 Post-Impact Jetting Along the Axis of "V" Grooves

We note a very interesting feature in the post impact hydrodynamics. In the grooves or valleys, the flow of the liquid layer is not restricted to the two dimensions. The inclined side walls of the groove exert resistance to spreading and subsequent recoil kinetics of the deforming droplet after impact. This leads to redirection of the impact kinetic energy to form jets issuing from the droplet mass along the groove length. While the droplet assumes an elliptical shape during spreading (due to the resistance by the inclided side walls), unhindered spreading along the groove leads to jetting from the two extremes of the droplet.

The axial flow or jetting from the droplet is noted to be symmetric about the centre line of the droplet perperdicular to the groove axis. One half of the symmetric axial jet flow and its temporal evolution has been shown in figure 5.9. For the higher impact We, the rim of the droplet issuing the jet is noted to be wavy in nature (figure 5.9 (c) and 5.9 (d), 1.67 and 2.23 ms), which is caused by the competing intertio-capillary forces at the interface. At lower We, the inertia is low, and hence the interface instabilities are not triggered.

On SHS, the capillary instabilities on the droplet-substrate interface is large, due to the non-wetting nature of the surface. Consequently, we have noted that on the SHS, the tip of the jet eventually decomposes to yield daughter droplets (figure 5.9 (d), 3.35 ms).

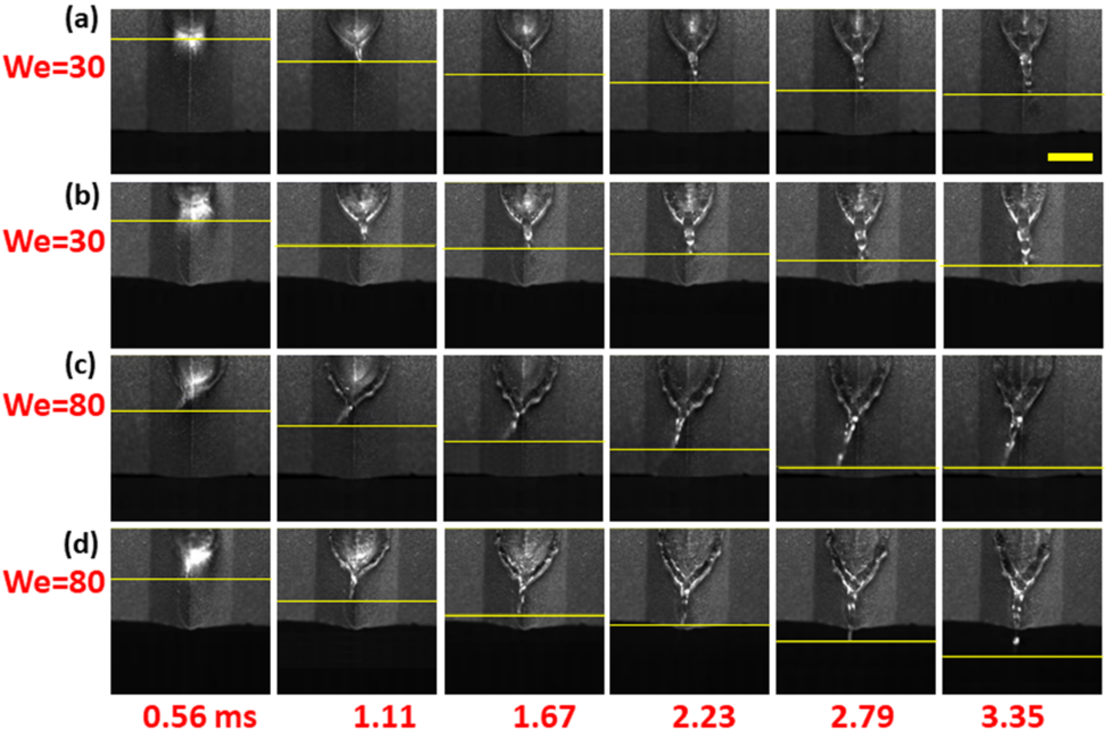

Figure 5.9 Evolution of the jet flow from the post-impact droplet (top view) along the groove (D^{*} = 2.4 and H^{*} = 0.8) at two different We and wettability. (a) We = 30; HP surface (b) We = 30; SH surface (c) We = 80; HP surface (d) We = 80; SH surface. The scale bar shown in the top right corner represents 3.24 mm length and is same for all the images. The yellow thin lines indicate the position of the tip of the evolving jet.

The temporal variation of the velocity of the tip of the jet is illustrated in figure 5.10. During the initial stages of post-impact hydrodynamics, the high inertia of the droplet spreading along the inclined groove walls is arrested by the geometry of the walls. Thereby, majority of this kinetic energy component is also available for spreading unrestricted along the groove length. The added energy leads to the jetting hydrodynamics observed on such valleys or “V” grooves. Consequently, the initial jet velocity, which starts abruptly from the droplet, is very high.

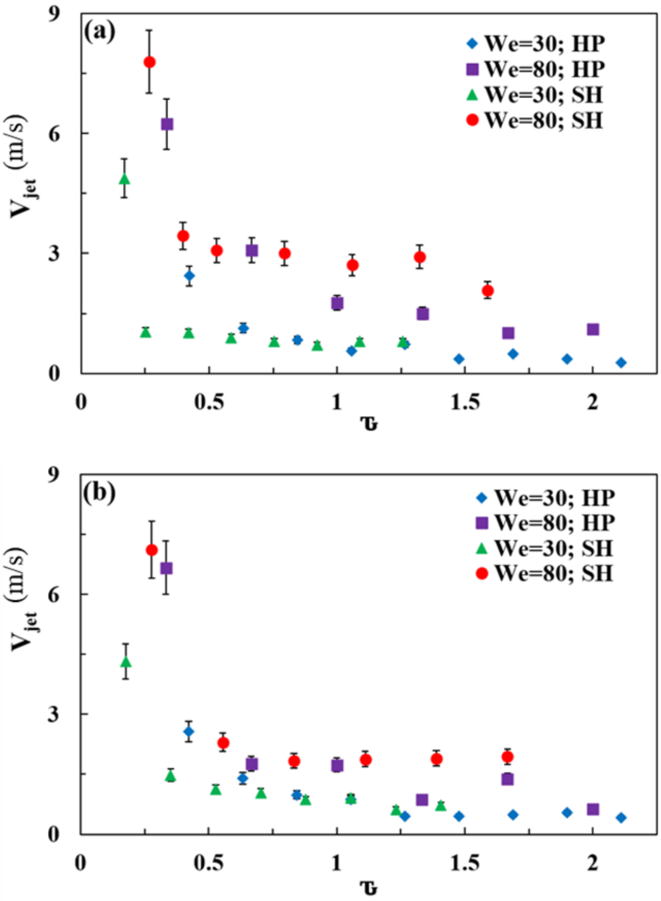

Figure 5.10 Variation of the velocity of the tip of the jet with the non-dimensional time for two different impact *We* on the both HP and SHS grooves with dimensions (a) $D^* = 1.6$; $H^* = 0.4$ (b) $D^* = 2.4$; $H^* = 0.8$.

As the central region of the droplet interacts with the groove surface, the visco-capillary forces dampen out the inertial force, leading to a reduction in the jet velocity. As time progresses, the jet velocity attains a steady value, before decaying out to zero at sufficiently longer times. We also note that for the same groove dimensions, the variation in temporal evolution of the jet velocity (at later stages) on the hydrophilic and the SHS are similar, both qualitatively and in magnitude. This observation shows that the axial jet flows along the groove length, without making much contact with the surface, and thereby leading to the wettability-independent kinetics.

Further, we propose an analytical formulation based on energy conservation principal [60,96] to predict the axial jet velocity from the other governing parameters. The different characteristic and geometric dimensions involved in the model derivation are illustrated in figure 5.11. Appealing to the fact that the nature of the impact and jetting phenomena is symmetric in nature along the groove length (about the center line perpendicular to the groove axis), the model derivation has been done for only one half of the droplet.

The kinetic energy of the droplet (assumed as a sphere) just before the impact is expressed as [96]

$$KE_i = \frac{1}{2}(\rho V^2)(\frac{\pi D_d^3}{6})$$

(5.1)

The initial surface energy of the droplet before impact is [96]

$$SE_i = \pi D_d^2 \sigma_{lg} \quad (5.2)$$

After impact, the motion of the liquid layer becomes three dimensional in nature. Both the spreading velocity of the liquid layer along the inclined walls of the valley, and the jet velocity in the axial direction contribute to the kinetic energy of the post-impact liquid mass (figure 5.11). In the model, the kinetic energy due to jetting is expressed by initially assuming that the total mass of the droplet moves in the axial direction with the tip velocity of the jet. Next, the expression is multiplied with a correction factor to consider the non-uniformity in the velocity at different positions and to account for the non-motile mass of fluid which is not involved in the jetting phase. The jet kinetic energy for the symmetrical half portion of the droplet is expressed as

$$KE_{jet} = \alpha[\frac{1}{2}(\frac{\pi D_d^3}{12})(\rho V_{jet}^2)] \quad (5.3)$$

Where, V_{jet} represents the instantaneous jet velocity and α is the correction factor which accounts for the frictional effects between the jet and the groove surface.

In figure 5.11, the jet is assumed to move along the groove without making any surface contact. Therefore, the contribution of the jet to the spreading kinetic energy (which is directed along the inclined groove walls) is zero. The expression for the spreading kinetic energy of the symmetrical half portion of the droplet is as

$$KE_{spread} = \beta[\frac{1}{2}(\rho V_{spread}^{2})(\frac{\pi D_{d}^{3}}{12} - \frac{\pi d_{jet}^{2} l_{jet}}{4})] \qquad (5.4)$$

V_{spread} in equation (5.4) is the instantaneous spreading velocity of the right (or left) triple contact point of the droplet along the groove walls, as visible from the front view (figure 5.11). Here, l_{jet} and d_{jet} are the instantaneous length and diameter of the jet, respectively. β is the correction factor used to accommodate for the temporal non-uniformity of the spreading velocity, and the fact that the jet shown in figure 5.11 is not a perfect cylinder. The surface energy of the liquid-air interface (for the symmetrical half of the jetting droplet) is expressed as

$$SE_{lg} = [A_{1}\left(\frac{l}{d}\right) + \pi d_{jet} l_{jet} + \pi d_{jet}^{2} + A_{2}]\sigma_{lg} \qquad (5.5)$$

In the above expression, A_1 is the projected area of the top surface of the deformed droplet which is spreading along the inclined walls of the groove (figure 5.11). This projected area has been multiplied by a factor $\frac{l}{d}$ to account for the curvature of the liquid-air interface. Here, l is the total length of liquid-air interface of the droplet spreading along the inclined walls of the groove (taken from the front view, figure 5.11) and d is the separation between the left and right three phase contact lines (taken from the front view, figure 5.11). Here, $\pi d_{jet} l_{jet}$ and πd_{jet}^2 represent the curved surface area, and the cross-section area, respectively, of the jet (assumed as an evolving cylindrical mass). A_2 is the projected cross-sectional area of the spreading droplet as seen from the front view. The surface energy of the liquid-solid interface for the symmetrical half of the droplet is expressed as

$$SE_{ls} = \frac{A_{1}}{\sin sin\,\theta}\sigma_{ls} \qquad (5.6)$$

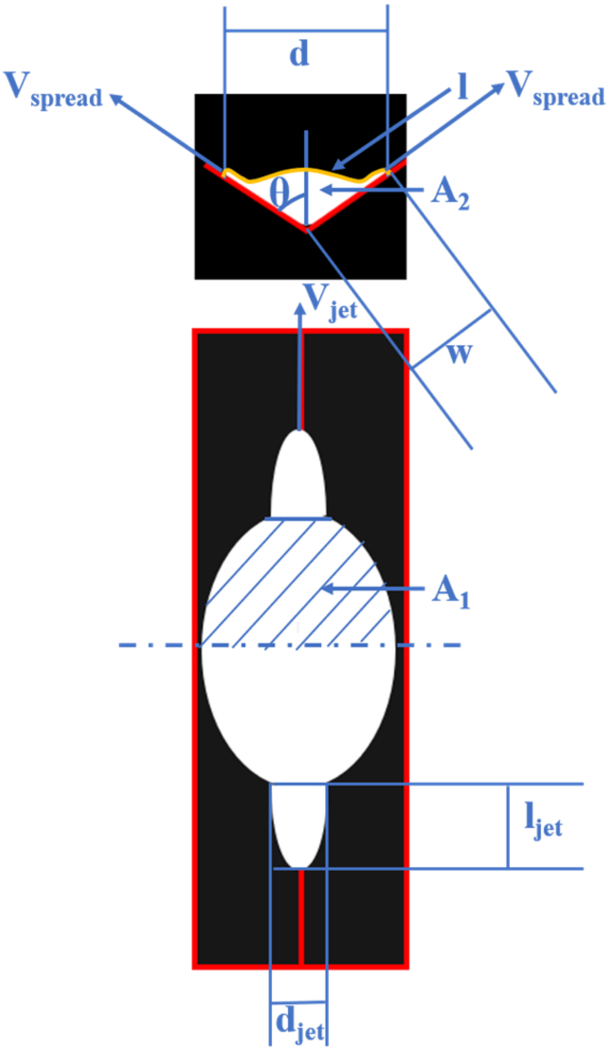

Figure 5.11 Schematic (front view and top view) of the post-impact droplet during jetting phase. The characteristic and geometric parameters considered in the model have been illustrated with proper labels. The dashed-dotted line represents the line of symmetry for the jetting behavior.

While spreading along the inclined walls, work is done by the droplet against the viscous resistance between the liquid layers. This is then dissipated in the form of the viscous dissipation which is expressed as [125]

$$E_{vis} = \int_0^{t_c} \int_v \psi dV dt \tag{5.7}$$

Here, t_c is the characteristic time scale and can be scaled as the ratio of the spreading length along the inclined wall (w) and the spreading velocity (V_{spread}) [56,126]

$$t_c \sim \frac{w}{V_{spread}} \tag{5.8}$$

In equation 5.7, v is the effective volume of the liquid experiencing the viscous effect under the effect of the boundary layer, and can be expressed (for the symmetrical half of the droplet) as

$$v = \frac{A_1}{\text{sinsin}\, \theta}\delta$$

(5.9)

ψ is termed as the dissipation function and can be scaled in terms of the spreading velocity and the boundary later thickness (δ) over the inclined walls as [60]

$$\psi \sim \mu\left(\frac{V_{spread}}{\delta}\right)^2 \tag{5.10}$$

δ is further written in terms of the characteristic spreading length (w) and spreading Reynolds number (Re_w) as

$$\delta \sim \frac{5w}{\sqrt{Re_w}} \tag{5.11}$$

Using $Re_w = \frac{\rho V_{spread} w}{\mu}$, equation (5.10) can be expanded as [61]

$$\delta \sim 5\sqrt{\frac{\mu w}{\rho V_{spread}}} \tag{5.12}$$

Next, integrating equation (5.7) using equations (5.8) – (5.11), final form of the expression for the viscous dissipation (for the symmetrical half of the droplet) is obtained as

$$E_{vis} = \frac{\rho}{5}\left(\frac{A_1}{\sin sin\,\theta}\right)\sqrt{\nu w}(V_{spread})^{\frac{3}{2}} \tag{5.13}$$

Where, ν is the kinematic viscosity ($\nu = \frac{\mu}{\rho}$) of the liquid.

From the principle of energy conservation, we get

$$KE_i + SE_i = 2(KE_{jet} + KE_{spread} + SE_{lg} + SE_{ls} + E_{vis}) \tag{5.14}$$

The factor "2" is multiplied in the RHS of equation (5.14) to accommodate for the fact that the energies calculated for the post-impact droplet is for the symmetrical half.

Using the expressions for all the components, equation (5.14) can be expressed as

$$\frac{1}{2}(\rho V^2)\left(\frac{\pi D_d^3}{6}\right) + \pi D_d^2\sigma_{lg} = 2[\alpha\frac{1}{2}\left(\frac{\pi D_d^3}{12}\right)\left(\rho V_{jet}^2\right) + \beta\frac{1}{2}\left(\rho V_{spread}^2\right)\left(\frac{\pi D_d^3}{12} - \frac{\pi d_{jet}^2 l_{jet}}{4}\right) +$$

(5.15)

Non-dimensionalizing equation (5.15) using the pre-impact surface energy, the relationship can be expressed in terms of the governing Weber number (We) and Capilliary number (Ca) as

$$\frac{We}{12} + 1 = \frac{1}{12}\alpha We\left(\frac{V_{jet}}{V}\right)^2 + \beta\left(\frac{1}{12}We - \frac{1}{4}We\frac{d_{jet}^2 l_{jet}}{D_d^3}\right)\left(\frac{V_{spread}}{V}\right)^2 + 2\left(\frac{A_1}{\pi D_d^2}\frac{l}{d} + \frac{d_{jet} l_{jet}}{D_d^2} +\right.$$

(5.16)

Equation (5.16) can be further rearranged to obtain the expression for V_{jet} in the following form

$$\frac{1}{12}\alpha We\left(\frac{V_{jet}}{V}\right)^2 = \frac{We}{12} + 1 - \beta\left(\frac{1}{12}We - \frac{1}{4}We\frac{d_{jet} l_{jet}}{D_d^2}\right)\left(\frac{V_{spread}}{V}\right)^2 - 2\left(\frac{A_1}{\pi D_d^2}\frac{l}{d} + \frac{d_{jet} l_{jet}}{D_d^2} +\right.$$

(5.17)

The transient jet velocity of the post-impact droplet is calculated using equation 5.17. We note that values of the factors α and β were found to be 0.25 and 0.2 respectively from the experimental data analysis, and the values were observed to be valid for the whole range of experiments. Experimental values have been used for the transient parameters appearing on the RHS of equation 5.17 required to predict the jet velocity mathematically. We have considered all the instantaneous experimental parameters for the model from image processing. The experimental jet velocities have been illustrated against the model predictions in figure 5.12 for different impact conditions and groove geometries.

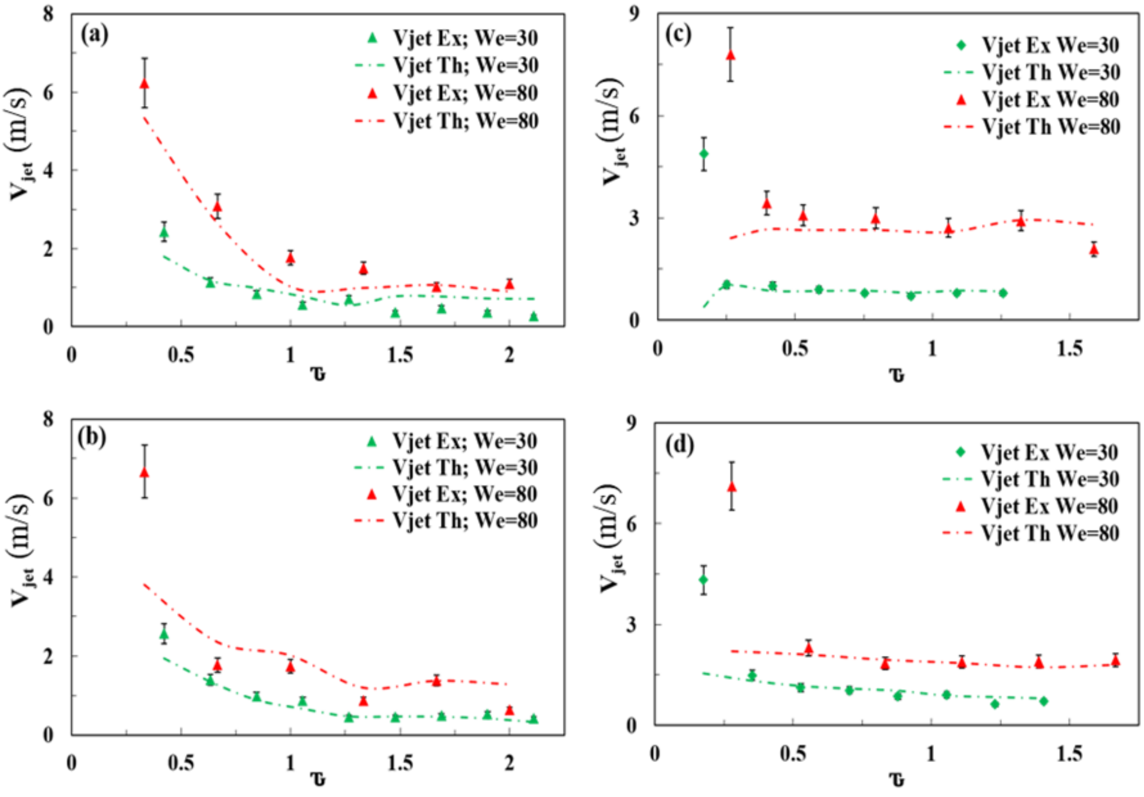

Figure 5.12 Comparison of the experimental (*Ex*) jet velocity against the theoretical (*Th*) predictions for different combinations of the "V" groove and wettability, for (a) $D^*=1.6$; $H^*=0.4$; HP (b) $D^*=2.4$; $H^*=0.8$; HP (c) $D^*=1.6$; $H^*=0.4$; SH (d) $D^*=2.4$; $H^*=0.8$; SH.

We note that the proposed model is able to predict the jet velocity of the post-impact droplet, except during the initial phase of the jetting dynamics. During the initial phase of the dynamics, the surface energy of the solid-liquid interface is overestimated in the mathematical analysis as the actual solid-liquid contact area is less than $\left(\frac{A_1}{\sin sin\,\theta}\right)$, which is used for the calculation of the jet velocity. Due to the water repellency behavior, the discrepancy is more apparent for the superhydrophobic surfaces which are visible in figure 5.12.

5.4 Closure

In the present chapter, post-impact droplet hydrodynamics on a “V” shaped groove is studied. Droplets are made to fall freely under gravity over the substrate surface and temporal images are captured using high speed camera. On impact, the droplets tend to spread over the surface to attain the lowest potential energy configuration. Impact Weber (We) and Capillary (Ca) numbers along with the wettability and groove geometrical dimensions govern the dynamics involved. It is observed that initially the spreading width of the droplets increases; attains its maximum value and then decreases with time. The north-pole height of the droplets first decreases up to its minimum value and then again increases. The spreading width of the post-impingement droplet decreases with an increase in groove-steepness as the wall reaction forces tend to restrain the motion. The effect of wettability is not observed for higher impact We due to the dominance of the inertial forces over the surface forces, but wettability plays a significant role in the dynamics for lower impact We as recoiling after attaining maximum spreading is clearly observed on the SH substrate in this case.

Presence of an axial passage along the groove axis leads to the generation of axial jets and makes the dynamics three-dimensional. Such hydrodynamics is absent on flat surfaces and convex contours. Axial jets gain a high impact velocity at the moment of its generation as a large fraction of the impact kinetic energy gets converted into the jet kinetic energy, but the velocity quickly reduces to a steady value due to the liquid-liquid cohesive forces and viscous resistance. Jet velocity is observed to increase with an increase in the impact We due to higher inertial energy. It is also observed that the jet velocity is more on the SH substrate in comparison to the HP substrate because of the lesser surface resistance to the flow, owing to the water repelling nature of the SH substrate. It is hence concluded that, a theoretical analysis has also been proposed to relate the transient evolution of jet velocity to the governing non-dimensional Weber (We) and Capillary (Ca) numbers based on the energy conservation principle. The model predictions are observed to be in good agreement with the experimental results.

Chapter 6

Droplet Post-Impact Regimes on Curved Concave Contours

6.1 Introduction

The present chapter explores the post-impact deformational morphology of droplet on curved concave contours. Spreading mechanisms on such asymmetrical target surfaces are complex and may lead to non-trivial outcomes and regimes based on the curvature and impact conditions [99,100,127]. The better understanding of the underlying process of droplet impact hydrodynamics on such geometries is vital in increasing the efficiencies of cooling, coating, spray painting and wetting of intricate concave structures and complexly designed components [6,128,129]. The present chapter investigated the hydrodynamics of water droplet impact on concave profile grooves of different concavity and wettability. The dynamic wetting behaviour after impact on concave surfaces having dimensions comparable to that of the droplet is less studied in literature and need detail investigation [104,123]. The transient spreading dynamics is therefore probed in azimuthal and axial directions, and interesting outcomes are revealed. Further, a theoretical model based on energy conservation principle [60] is proposed to predict the time evolution of the jet velocity along the axis of the grooves.

6.2 Materials and Methodologies

The experimental setup is similar to the one used in the previous chapter 5. Figure 6.1(A) illustrates the schematic of the experimental setup. Droplets of diameter approximately 2.8 mm are generated using a 250 µl chromatography glass syringe which is attached to a 22-gauge stainless steel needle. Droplet dispensing is controlled by a digitized droplet dispenser mechanism (least count 0.1 µl). Diameter of the droplet is calculated by dispensing a fixed volume of liquid using the dispenser and is also verified from the image post processing. The droplet is allowed to fall freely from different heights under the influence of gravity to achieve the desired impact velocities (~0.95, ~1.17 and ~1.5m/s, within ± 5% accuracy). The impact phenomenon is captured at 3600 frames/s (at 1024×1024 pixels resolution) by a high-speed camera (Photron, UK), with a constant focal length (105 mm) macro lens (Nikkor, Nikon). To capture the front view, the camera is placed along the groove axis as shown in Figure 6.1. For the top view images, a camera is placed vertically, orthogonal to the front view position. A white light emitting diode array with brightness controller system (DPLED, China) is used for backlight illumination.

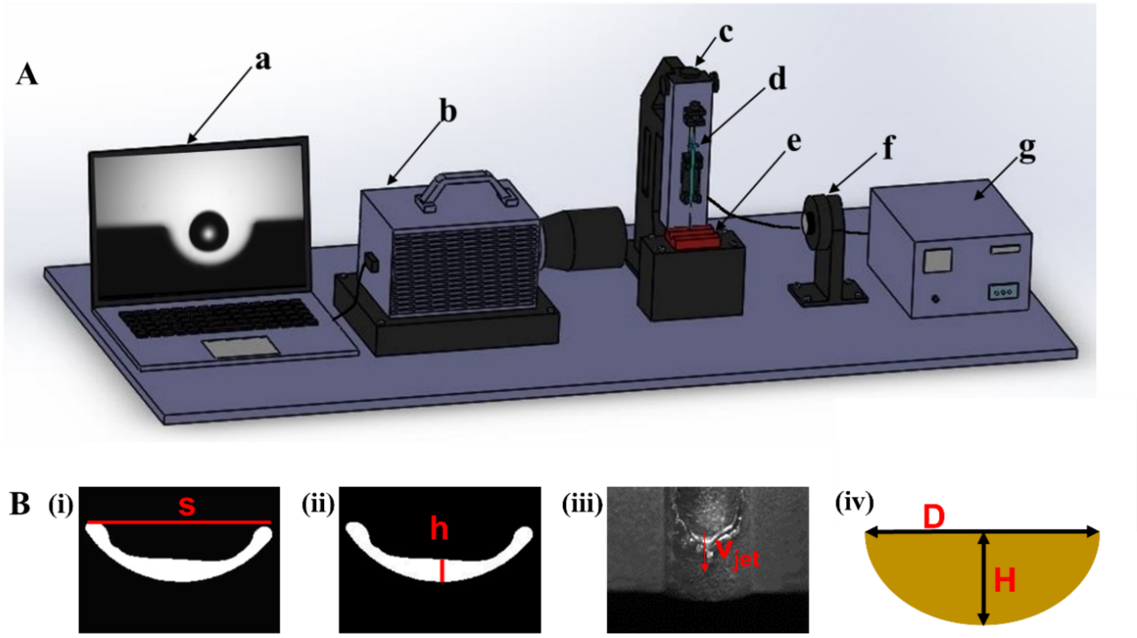

Figure 6.1 (A) Schematic of the experimental setup (a) data acquisition computer system, showing the front view just before the impact of the droplet on the substrate (b) high speed camera (c) precision droplet dispenser mechanism (d) chromatography glass micro-syringe with a stainless-steel needle (e) substrate (concave groove) (f) backlight illumination source (g) droplet dispensing and backlight illuminating system controller. (B) Illustration of transient spreading parameters and representative of the target surface (concave groove): (i) spreading width, s (ii) south-pole film thickness, h (iii) jet velocity, V_{jet} (iv) schematic representing groove dimensions.

The fluid used in the study is deionized water. The target surfaces employed are concave profile grooves of different widths and depths (refer Table 6.1 for groove dimensions) machined in steel blocks using electro-discharge machining. Experiments are performed on both hydrophilic surfaces and SHS. The hydrophilic substrates are prepared by cleaning the concave grooves with acetone. A set of replica substrates are coated with a commercial superhydrophobic spray (Never wet, USA) to produce SH substrates. Several trials are performed to ensure that the water droplets are precisely impacted on the axis of the grooves. Each case was repeated twice on three different sample targets for repeatability. The temperature of 25° ± 3° and relative humidity (RH) of 50% ± 5% are maintained throughout the experiments. The experimental images are post-processed using the open-source code ImageJ to quantify and analyze the key parameters (referred in Figure 6.1(B)). The images of the droplet hydrodynamics are presented using the inverted binary color scheme. The fluid is represented in white pixels while the solid and air regions are presented in black pixels. The groove profiles are demarcated by a red curve in all the figures. Table 6.2 presents the values of surface energy per unit area for the solid-liquid (σ_{sl}) and liquid-gas (σ_{lg}) interfaces present.

Table 6.1 Dimensions of the concave grooves. 'D' represents the width and 'H' represents the depth of the groove (refer figure 6.1 B (iv) for schematic).

Sl. No.	**D (mm)**	**H (mm)**
1.	6	3
2.	4.4	2
3.	6	2
4.	2.5	2
5.	6	1.2

6.3 Results and Discussions

Experimental images (both front and top views) are used to understand the distribution of liquid film flow in the grooves at different instants of time after impact. The temporal evolution of the following parameters, i.e., non-dimensional spreading width (γ), non-dimensional south pole film thickness (h^*) and axial jetting velocity (V_{jet}) are shown. The spreading width (s) and south-pole film thickness (h) are non-dimensionalized using the pre-impact droplet diameter (D_d). The width (D) and depth (H) of the concave groove are also non-dimensionalized similarly (expressed as $D^* = \frac{D}{D_d}$ and $H^* = \frac{H}{D_d}$). We have used the non-dimensional time ($\tau = \frac{tV}{D_d}$, where t is the instantaneous time after impact, V is the droplet impact velocity, and D_d is the pre-impact droplet diameter) for all analysis. Non-dimensional numbers used to discuss the post-collision dynamics are Weber number (We), Capillary number (Ca), and Reynolds number (Re) (expressed as $We = \frac{\rho V^2 D_d}{\sigma_{lg}}$, $Ca = \frac{\mu V}{\sigma_{lg}}$, and $Re = \frac{\rho V D_d}{\mu}$ where ρ = density of the liquid droplet, σ_{lg} = surface tension for the liquid-air interface, μ = dynamic viscosity of the liquid).

Table 6.2 Interfacial tensions for the liquid-gas and solid-gas interfaces and static contact angle for the flat surfaces [112].

Target surface	σ_{sl} **(J/m²)**	σ_{lg} **(J/m²)**	**Contact angle (θ_c)**
Stainless steel	0.18	0.0728	45° ± 3°
SHS	0.2726	0.0728	135° ± 3°

6.3.1 Dynamics in Hydrophilic Grooves

The post-collision dynamics have been quantitatively presented in the form of time series arrays. Figure 6.2 illustrates a sequence of front view images at different time instants for droplet impact on hydrophilic concave groove ($D^* = 2.14$ and $H^* = 1.07$) with different impact We. As observed, post-impact droplet spreads along the curvature of the groove and forms a thin film at around 3.06 ms. Next the fluid film is observed to recoil along the azimuthal direction (curvature of the groove). While this recoil phenomenon has begun along the azimuthal direction, the fluid is still in the spreading stage along the axis of the groove, which leads to the formation of a distinct fluid ridge at the liquid–air interface, located vertically above the apex of the groove (Figures 6.2 (a)-(c) at 4.17 ms onwards).

This fluid ridge apex increases in height with continuation of the azimuthal recoiling stage. The effect of the impact We is evident from this array in Figure 6.2. With increase in the impact We, more kinetic energy is imparted to the spreading regime, therefore the extent of spreading increases but the thickness of liquid film decreases at all the positions at any time instant inside the groove. On hydrophilic surface, the higher spreading leads to more wetting, which in turn reduces the kinetic energy available for the recoil regime. Thereby the fluid bulge formed due to recoil is less prominent at high We as compared to low We cases.

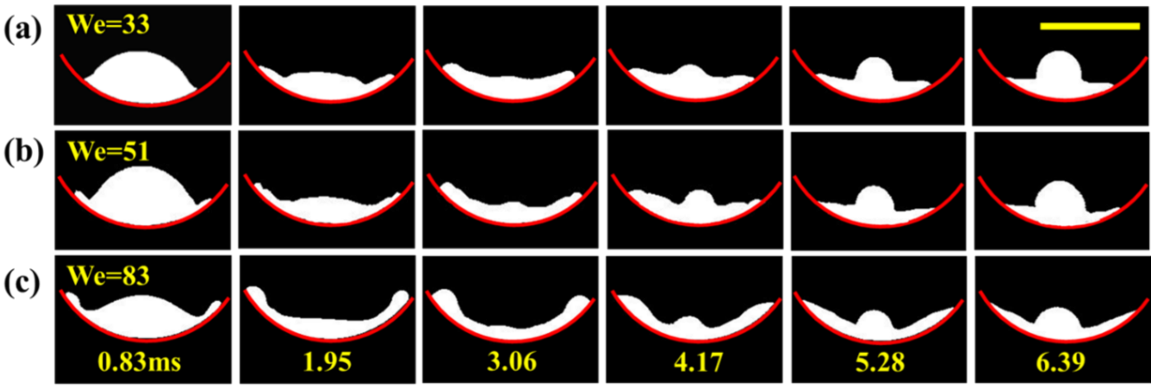

Figure 6.2 Temporal evolution of the post-impact droplet (front view) on the concave grooves having dimensions $D^* = 2.14$ and $H^* = 1.07$, for three different We: (a) $We = 33$ (b) $We = 51$ and (c) $We = 83$. The scale bar shown in the top right corner represents 3 mm and is same for all the images. The red curve indicates the profile of the groove.

Figures 6.3 and 6.4 illustrate the influence of the geometry of the concave grooves on the post-collision behavior. Three grooves with same width (fixed D^*) and different depths (different H^*) have been shown in Figure 6.3. As the depth of the groove increases, the curvature of the groove profile tends to increase. Therefore, the curved profile provides additional resistance to spreading (by disrupting the flow of the film radially), which leads to less spreading for deeper grooves. On the contrary, the recoiling phase is more significant in such grooves due to the same reason. For $H^* = 0.43$ (Figure 6.3 (c)), spreading regimes are very similar to that on the flat surfaces, as the curvature is very low. It is important to note that the apparent volume of the droplet (as viewed from the front) reduces in each case as the droplet is also spreading along the axis of the groove (discussed in the following section.).

Fig. 6.4 illustrates the post-impact droplet regimes on three grooves with same depth (fixed H^*) and different widths (different D^*). The resistance to the liquid flow is the highest for least width case ($D^* = 0.89$). Inertia-capillary instabilities at the liquid–air interface is evident for this particular case due to the interplay of inertia and wetting forces in the high curvature groove. Moreover, owing to the smaller dimension of the groove, the liquid droplet also spreads outside the groove region.

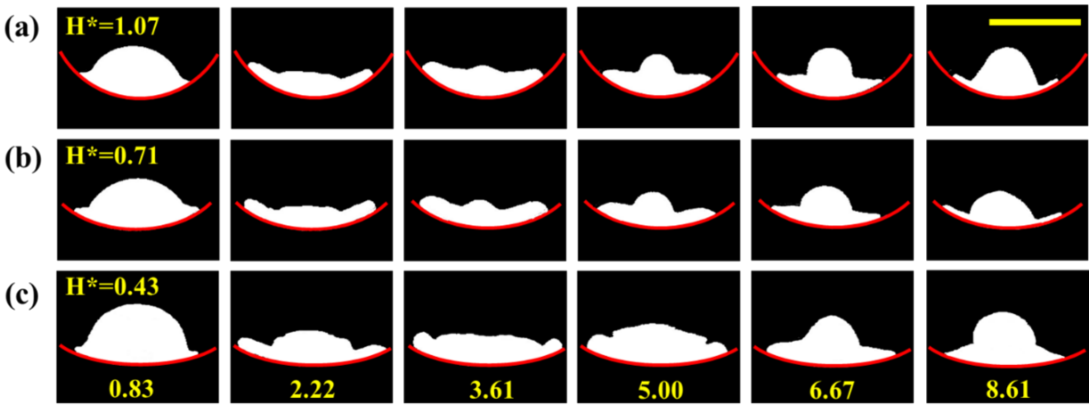

Figure 6.3 Temporal evolution of the post-impact droplet (front view) for $We = 33$ on concave grooves with fixed $D^* = 2.14$ and three different H^*: (a) $H^* = 1.07$ (b) = 0.71 and (c) = 0.43. The scale bar shown in the top right corner represents 3 mm length and is same for all the images.

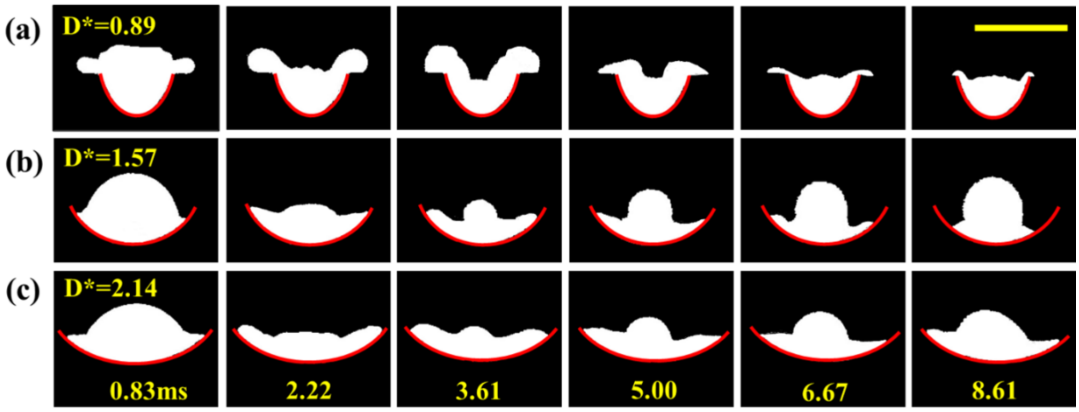

Figure 6.4 Temporal evolution of the post-impact droplet (front view) for $We = 33$ on concave grooves with fixed $H^* = 0.71$, and three different D^*: (a) $D^* = 0.89$, (b) = 1.57 and (c) = 2.14. The scale bar shown in the top right corner represents 3mm length.

Figure 6.5 shows the evolution of the non-dimensional film thickness at south-pole of the target and the spreading width with the non-dimensional time for different combinations of impact We and groove dimensions (hydrophilic surface). It is evident from figures 6.5 (a) and (c) that qualitatively, the non-dimensional film thickness at south-pole (for each case) first decreases rapidly to attain minima (due to lateral spreading), and then increases in the recoiling phase. Interestingly the recoil occurs earlier for lower impact velocity cases because less initial kinetic energy is balanced much quicker which results in attainment of minima earlier than high impact velocity cases.

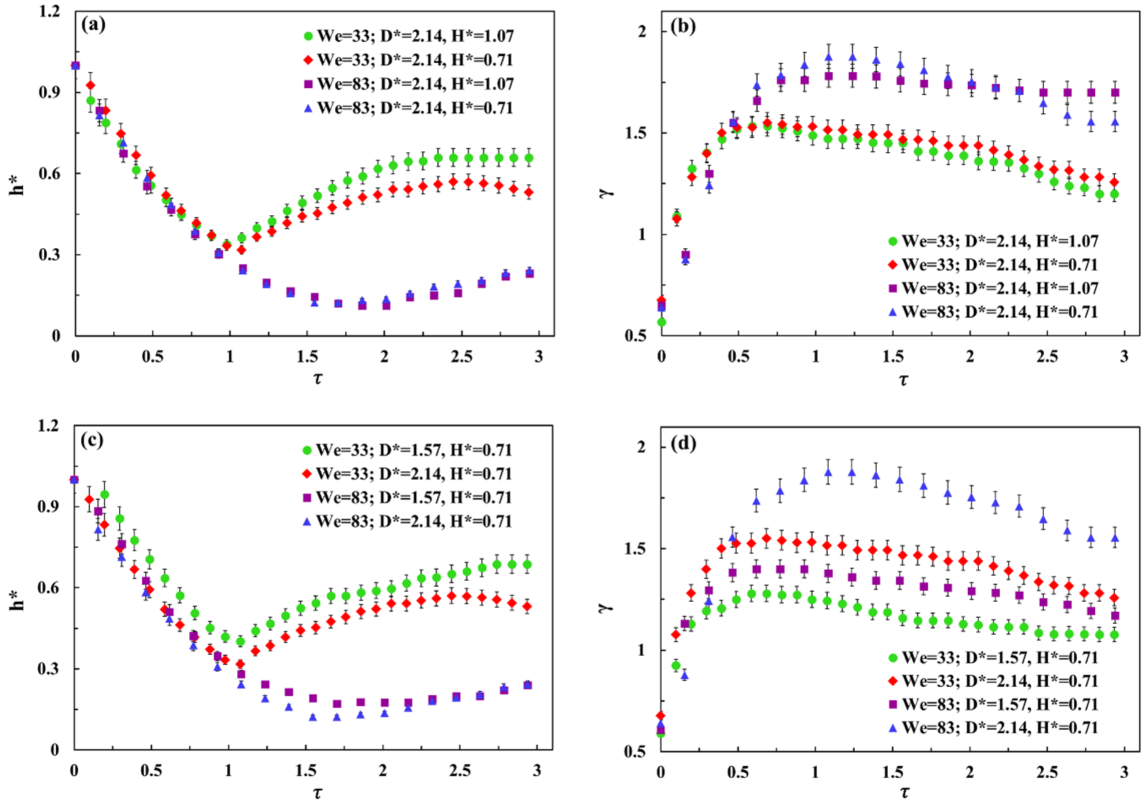

Figure 6.5 Temporal variations of (a) and (c) non-dimensional south-pole film thickness (h^*) and (b) and (d) non-dimensional spreading width (γ), for different hydrophilic grooves at different impact We.

Moreover, the effect of curvature of the groove by changing only one dimension of the groove is also noted from Figure 6.5 (a) and (c) on south-pole film thickness. For higher curvature of the groove, rate of reduction of film thickness is more before attaining the minima and recoil is also more significant (groove D^*=2.14 and H^*=1.07 has higher curvature than groove D^*=2.14 and H^*=0.71). Non-dimensional spreading width increases rapidly after the impact, attains point of maxima, then reduces slowly (Figure 6.5 (b) and (d)). Also, for the same impact We, the spreading width of the droplet is observed to be lower on grooves with higher curvature. This is because more resistance to lateral spread is provided by the surface curvature for more curved grooves (curvature only increased by changing one dimension of the groove).

6.3.2 Dynamics in Superhydrophobic Grooves

Figure 6.6 compares the post-collisional droplet deformation on the hydrophilic and the superhydrophobic grooves at two different impacts We. During the spreading phase, the hydrodynamics on both the surfaces look quite similar, but significantly greater and quicker recoil is observed for SH grooves than its hydrophilic counterparts. More capillary instabilities are evident in the film structures on non-wetting grooves (Figure 6.6 (b) and (d) at 3.89 ms). For higher impact We, rebound effect is observed on the SH grooves (Figure 6.6 (d) at 9.17 ms), whereas the recoil effect is negligible on hydrophilic target grooves.

In Figure 6.7, temporal evolution of non-dimensional south-pole film thickness for three different grooves at two different impacts We has been compared for the hydrophilic and the superhydrophobic surfaces. For the superhydrophobic surfaces, variation of h^* follows a similar trend as on hydrophilic surfaces during the initial phase of spreading, because inertial forces are more prominent than surface forces. This initial phase has been referred as inertial phase of spreading in the literature by researchers [28,55]. When the velocity slows down further with time, more surface effects come into play and the variation of h^* for SHS deviates from that of the hydrophilic behavior (generally after $\tau = 1$). Therefore, the trend of h^* observed on SH surfaces shows that it acquires a minimum point value further from which spreading of the impacted droplet stops and recoiling begins. Due to the non-wetting nature of SHS (high energy surfaces), a sharp recoil is thus observed. It is noteworthy that, surface wettability effect on h^* is more pronounced for high impact We.

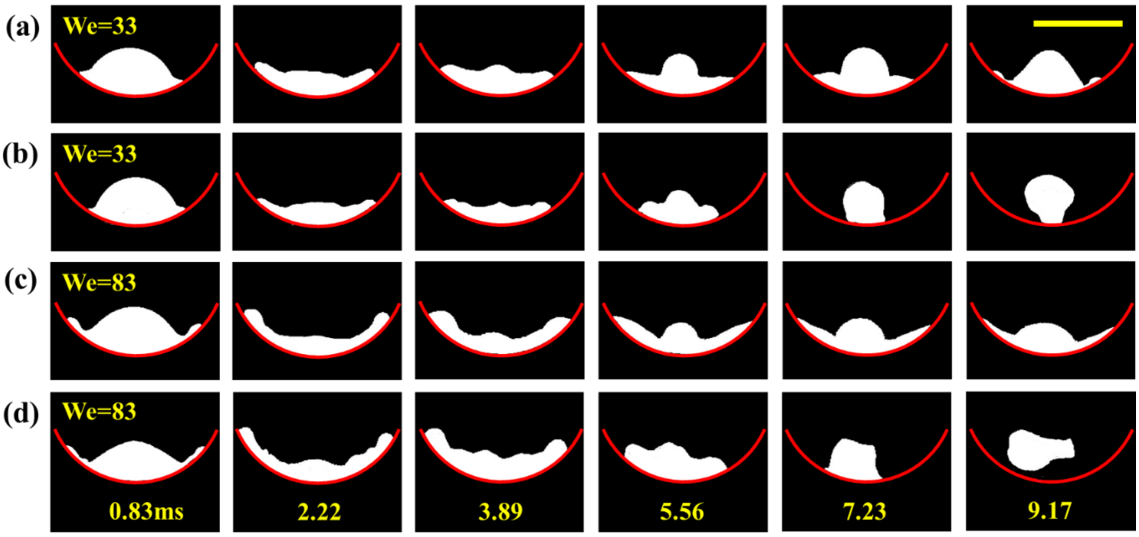

Figure 6.6 Temporal evolution of the post-impact droplet (front view) on a concave groove (D^* = 2.14 and H^* = 1.07) for two different combinations of impact We and wettability. (a) We = 33, hydrophilic surface (HP) (b) We = 33, superhydrophobic surface SHS (c) We = 83, HP surface (d) We = 83, SHS. The scale bar at the top right corner represents 3mm.

Figure 6.8 highlights the effect of the surface wettability on the temporal evolution of the non-dimensional spreading width of the liquid film (for three different grooves at two different impact conditions). Just like for h^*, the trend for non-dimension spreading width (γ) during the initial spreading phase is almost independent of the surface wettability. After attaining the maximum value, a sharp decrease is observed in γ values for the superhydrophobic targets whereas this decrease is very less and at low rates for the hydrophilic targets.

It is also noteworthy that, the maximum value of non-dimensional spreading width (γ) is higher for SH surfaces than HP surfaces for higher impact We cases (for all three grooves). This is because, before attaining the maxima, the tendency of the impacted droplet is to spread due to the inertial energy and lower wettability of SH surface provides lesser resistance to the flow.

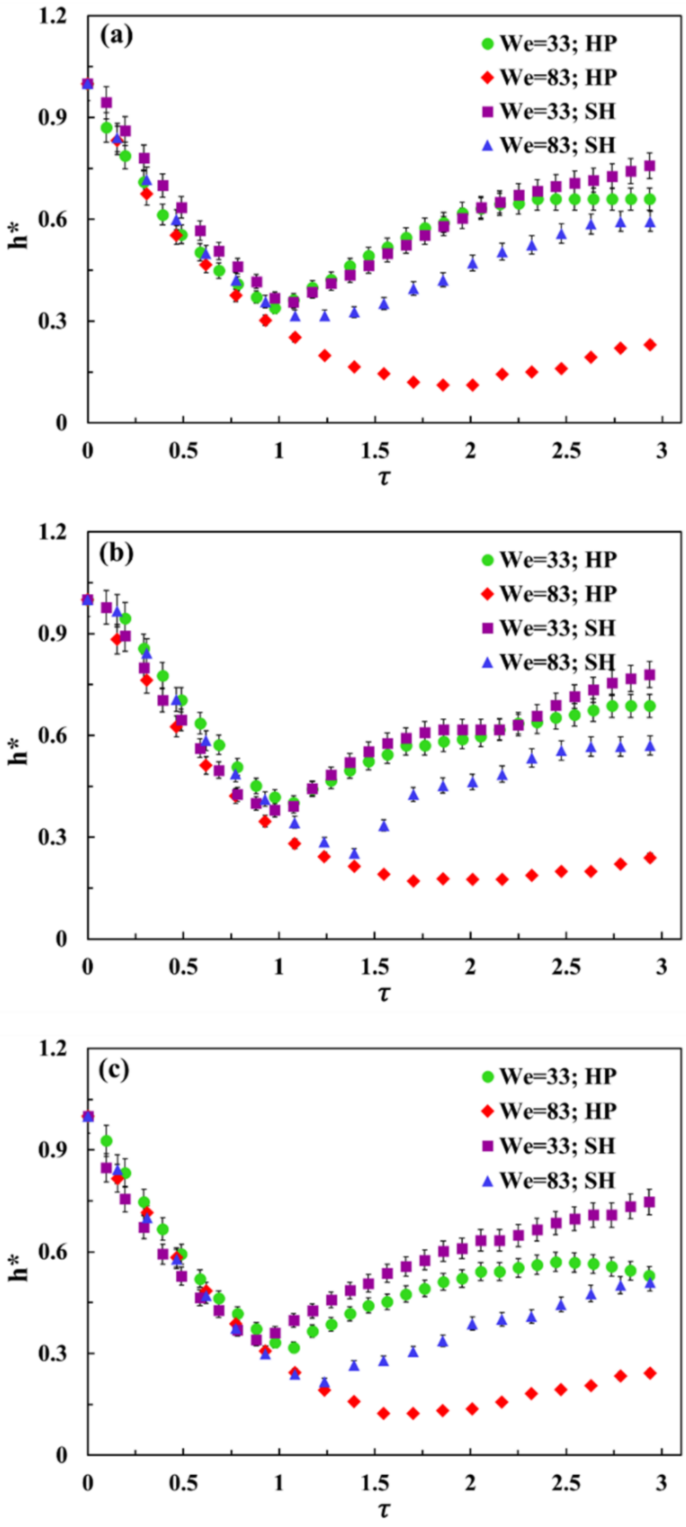

Figure 6.7 Temporal variation of the non-dimensional south-pole film thickness of post-impact droplet on both hydrophilic (HP) and superhydrophobic (SH) concave grooves with dimensions (a) $D^* = 2.14$, $H^* = 1.07$ (b) $D^* = 1.57$, $H^* = 0.71$ (c) $D^* = 2.14$, $H^* = 0.71$.

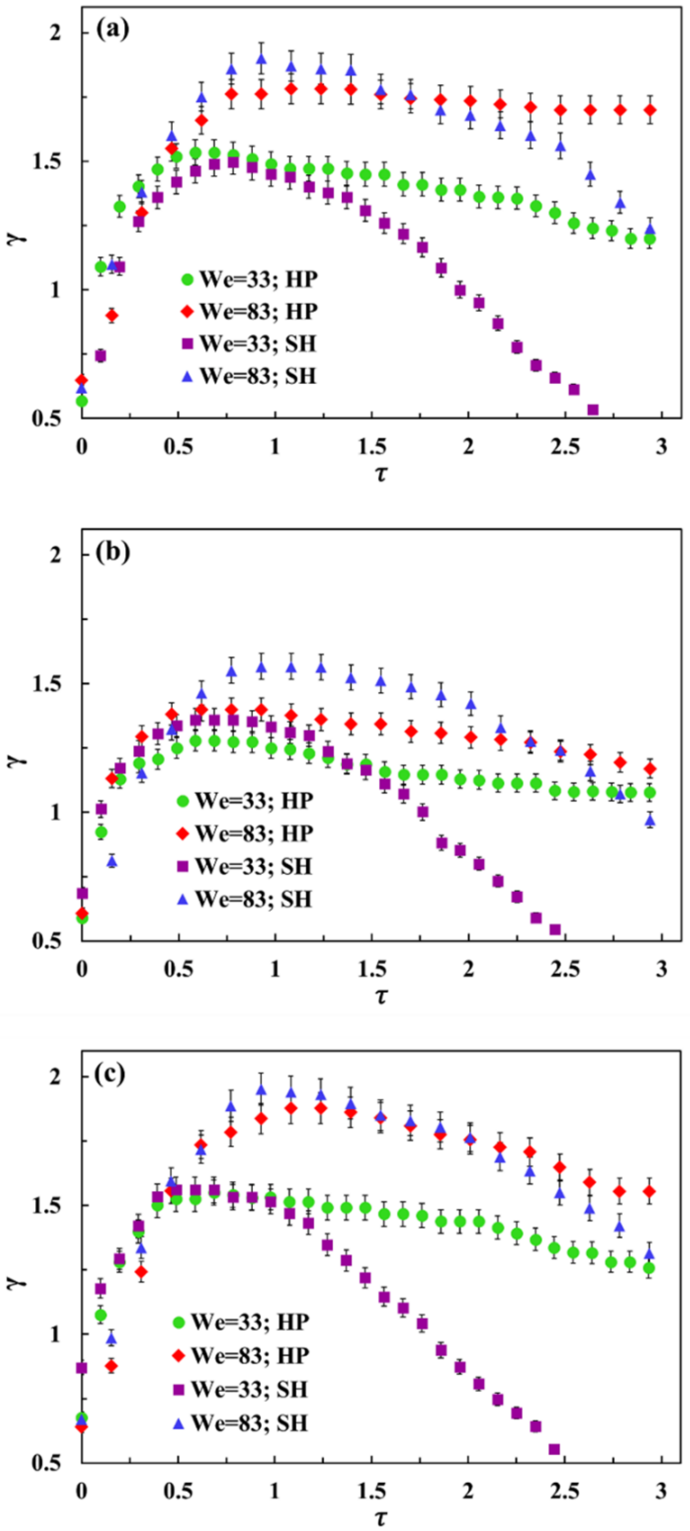
(a)
γ
τ
2
1.5
1
0.5
0
0.5
1
1.5
2
2.5
3
● We=33; HP
◆ We=83; HP
■ We=33; SH
▲ We=83; SH
(b)
γ
τ
● We=33; HP
◆ We=83; HP
■ We=33; SH
▲ We=83; SH
(c)
γ
τ
● We=33; HP
◆ We=83; HP
■ We=33; SH
▲ We=83; SH

Figure 6.8 Temporal variation of the non-dimensional spreading width of post-impact droplet on both hydrophilic (HP) and superhydrophobic (SH) concave grooves with dimensions (a) $D^{*} = 2.14$; $H^{*} = 1.07$ (b) $D^{*} = 1.57$; $H^{*} = 0.71$ (c) $D^{*} = 2.14$; $H^{*} = 0.71$.

6.3.3 Post-Impact Axial Jetting Phenomenon

When droplet is impacted on the asymmetrical structures like concave grooves, the resulting hydrodynamics is three dimensional (azimuthal and axial direction) and cannot be inferred from front view images only. Therefore, top view images captured are used to probe the hydrodynamic phenomenon along the axis of the groove. In grooves (concave surfaces), the gravity forces adversely affect the extension of droplet along the azimuthal direction due to which, kinetic energy is redirected along the axial direction. The spreading velocity thus generated along the axial direction is termed as the jetting velocity. The axial flow is noted to be symmetric about the centerline of the droplet perpendicular to the groove axis. Figure 6.9 presents the temporal evolution of one half of the symmetric axial jet flow.

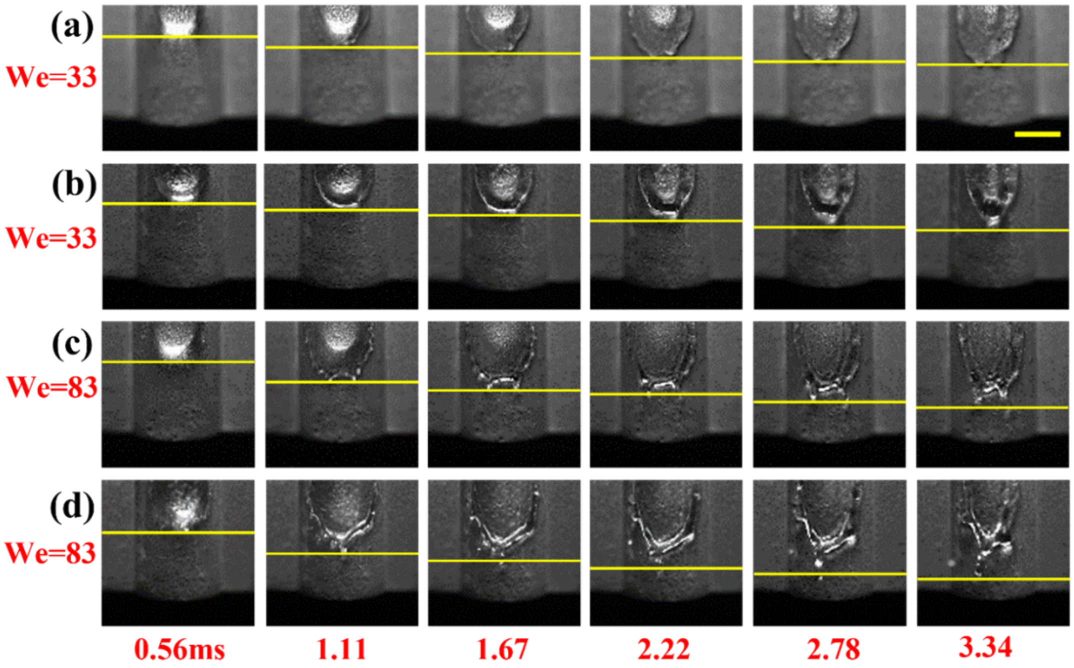

Figure 6.9 Top view images taken at different time instants for the impact of a water droplet onto a concave groove ($D^{*} = 2.14$ and $H^{*} = 1.07$) for two different combinations of

impact We and wettability. (a) We = 33, hydrophilic (HP) surface (b) We = 33, SHS (c) We = 83, HP surface (d) We = 83, SHS. The scale bar at the top right corner represents 3 mm and is same for all the images. The yellow lines indicate the tip of the axial jet.

It is observed that with the increase in the impact We, spreading along the axial direction is enhanced. It is also important to note that due to capillary instabilities on the droplet-substrate interface for SHS, the tip of the jet breaks to yield daughter droplets (refer Figure 6.9 (d) at 3.34 ms). Comparative study of the arrays in figures 6.10 and 6.11 illustrates the liquid film evolution along the axis of the groove on changing the just one dimension of the groove. Interestingly, by decreasing the depth of the groove for the same width, the curvature of the groove decreases. Similar effect is observed on increasing the width of the groove for same depth. Spreading morphology of the impacted droplet represented in figure 6.10 (c) at 2.78 ms is tending to that on flat surfaces owing to less curvature of the groove. In figure 6.11, it is evident that, there is more axial spreading for groove having higher curvature (see figure 6.11 (a) at 3.34 ms).

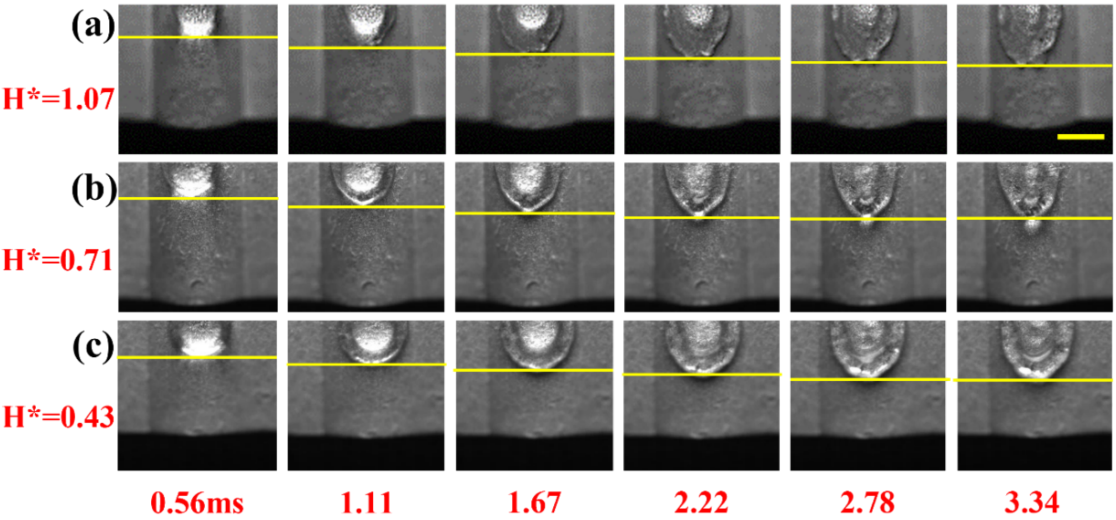

Figure 6.10 Top view images taken at different time instants for the impact of a water droplet on concave grooves with fixed D^* = 2.14 and three different H^*: (a) H^* = 1.07 (b) H^* = 0.71 and (c) H^* = 0.43. The scale bar shown represents 3 mm length and is same for all the images. The yellow lines indicate the tip of the axial jet.

Figure 6.12 depicts the plot of jetting velocity with non-dimensional time (τ) for three different grooves. The jetting velocity starts abruptly high after the impact. As the time progresses, the central region of the droplet interacts with the groove surface, thus the viscous-capillary forces dampen out the inertial force and decreases the jetting velocity. The effects of impact We and wettability are illustrated in Figure 6.12. It is noted that, on increasing the impact We, the jetting velocity increases, as more initial kinetic energy is available. Moreover, the jetting velocity is also found to be higher for SH substrates for higher We cases and is measured till the jet disintegrates to form daughter droplets. The reason is attributed to air pockets and non-penetration of liquid during jetting phenomenon on SH surfaces (high energy surfaces).

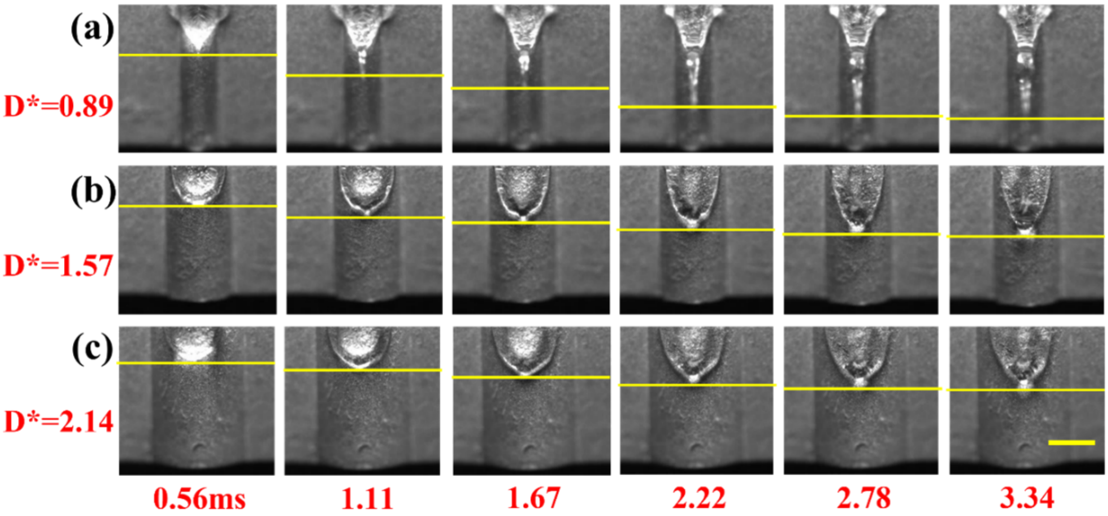

Figure 6.11 Top view images taken at different time instants for the impact of a water droplet on concave grooves with fixed $H^{*} = 0.71$, and three different D^{*}: (a) $D^{*} = 0.89$, (b) = 1.57 and (c) = 2.14. The scale bar shown in the bottom right corner represents 3mm length and is same for all the images. The yellow lines indicate the tip of the axial jet.

Further, an approximate-analytical formulation is hereby proposed next, based on the energy conservation principle to predict the axial jetting velocity at various time instants, from the other governing parameters. Figure 6.13 is a schematic illustrating different characteristics and geometrical dimensions involved in the following derivation.

6.3 Results and Discussions

The schematic figure indicates various variables used in the derivation. The nature of droplet hydrodynamics and the jetting phenomenon is symmetric along the groove length for the considered surfaces. Therefore, for simplicity the model derivation has been done for only one half of the droplet.

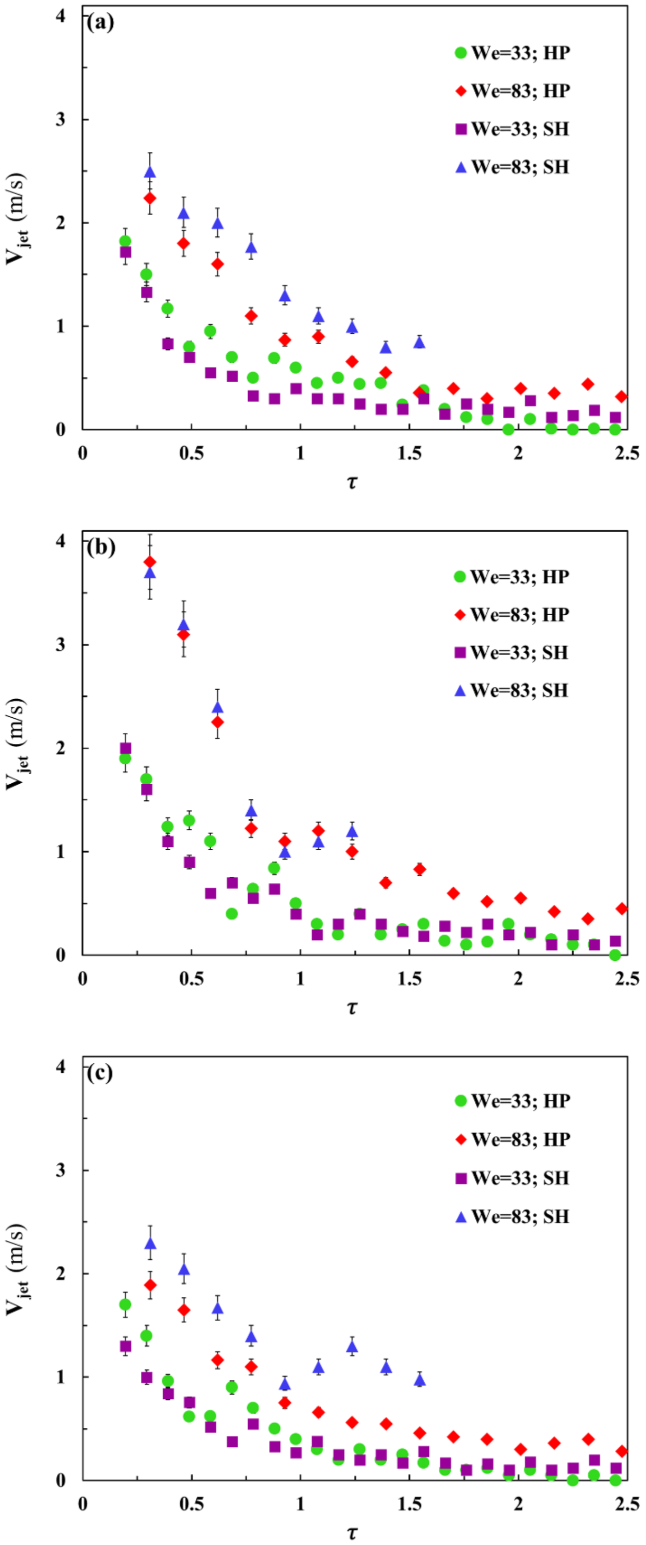

Figure 6.12 Temporal variation of the jet velocity for two different impacts We on the both HP and SHS concave grooves with dimensions (a) $D^* = 2.14$, $H^* = 1.07$ (b) $D^* = 1.57$, $H^* = 0.71$ (c) $D^* = 2.14$, $H^* = 0.71$.

The kinetic energy of the droplet (assumed perfectly spherical in shape) just before the impact is expressed as [113]

$$KE_i = \frac{1}{2}(\rho V^2)(\frac{\pi D_d^3}{6})$$

(6.1)

The initial surface energy of the droplet before impact is [113]

$$SE_i = \pi D_d^2 \sigma_{lg} \tag{6.2}$$

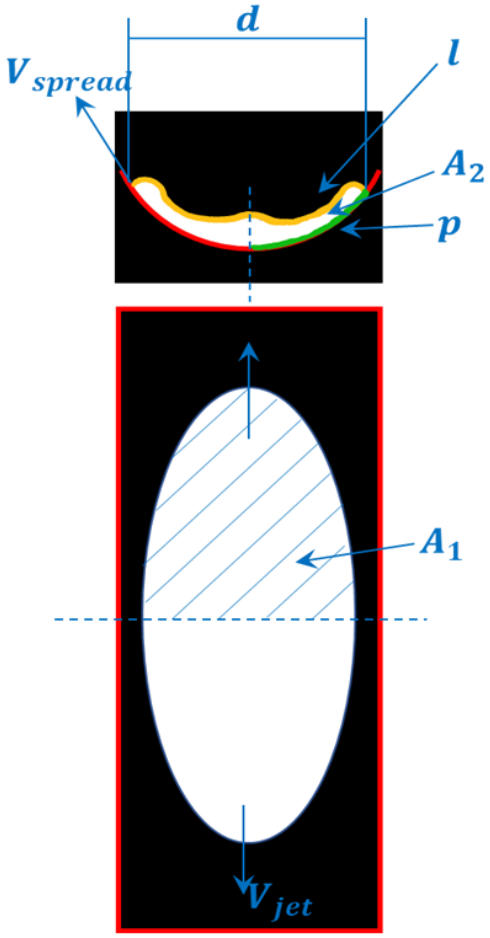

Figure 6.13 Schematic (front view and top view) of the post-impact droplet during the jetting phase. The characteristic and geometric parameters considered in the model have been illustrated with proper labels. The dashed-dotted line represents the line of symmetry.

After impact, the motion of liquid layer is observed in azimuthal and axial directions. Both the spreading velocity of the liquid layer along the curvature of the groove, and the jetting velocity in the axial direction contribute to the kinetic energy of the post-impact liquid mass (Figure 6.13).

Post-impact, the jet kinetic energy is expressed by initially assuming that the total mass of the droplet moves in the axial direction with the tip velocity of the jet. Next, the expression is multiplied with a correction factor to consider the non-uniformity in the velocity at different positions. The jet kinetic energy for the symmetrical half portion of the droplet is therefore expressed as

$$KE_{jet} = \alpha[\frac{1}{2}(\frac{\pi D_d^3}{12})(\rho V_{jet}^2)] \qquad (6.3)$$

Where, V_{jet} represents the instantaneous jetting velocity at the tip and α is the correction factor which accounts for the non-uniformity in the velocity at different positions.

The expression for the spreading kinetic energy of the symmetrical half portion of the droplet is as

$$KE_{spread} = \beta[\frac{1}{2}(\rho V_{spread}^2)(\frac{\pi D_d^3}{12})] \qquad (6.4)$$

V_{spread} in equation (6.4) is the instantaneous spreading velocity of the right (or left) triple contact point of the droplet along the groove walls, as visible from the front view in Figure 6.13. Here, β represents the correction factor to accommodate for the non-uniformity of the spreading velocity at different positions. The surface energy of the liquid-air interface (for the symmetrical half of the jetting droplet) is expressed as

$$SE_{lg} = [A_1\left(\frac{l}{d}\right) + A_2]\sigma_{lg} \qquad (6.5)$$

In the above expression, A_1 is the projected area of the top surface of the deformed droplet which is spreading along the curvature of the groove (Figure 6.13). This projected area has been multiplied by a factor $\frac{l}{d}$ to account for the curvature of the liquid-air interface. Here, l is the total length of liquid-air interface of the droplet spreading along the curve of the groove (measured from the front view, figure 6.13) and d is the separation between the left and right three phase contact lines (measured from the front view, figure 6.13). A_2 is the projected cross-sectional area of the spreading droplet as seen from the front view. Therefore, the surface energy of the liquid-solid interface (for the symmetrical half of the droplet) is expressed as

$$SE_{ls} = [A_1\left(\frac{l}{d}\right)]\sigma_{ls} \qquad (6.6)$$

While spreading along curve of the groove, work is done by the droplet against the viscous resistance between the liquid layers. This is then dissipated in the form of the viscous dissipation which is expressed as [124]

$$E_{vis} = \int_{0}^{t_c} \int_{v} \psi dV dt \tag{6.7}$$

Here, t_c is the characteristic time scale and can be scaled as the ratio of the spreading length along the curvature of the groove (p) and the spreading velocity (V_{spread}) [56,125]

$$t_c \sim \frac{p}{V_{spread}} \tag{6.8}$$

In equation 6.7, v is the effective volume of the liquid experiencing the viscous effect under the effect of the boundary layer, and can be expressed as

$$v = [A_1\left(\frac{l}{d}\right)]\delta \tag{6.9}$$

ψ is termed as the dissipation function and can be scaled in terms of the spreading velocity and the boundary later thickness (δ) over the curvature as [60]

$$\psi \sim \mu\left(\frac{V_{spread}}{\delta}\right)^2 \tag{6.10}$$

δ is further written in terms of the characteristic spreading length (p) and spreading Reynolds number (Re_p) as

$$\delta \sim \frac{5p}{\sqrt{Re_p}} \tag{6.11}$$

Using $Re_p = \frac{\rho p V_{spread}}{\mu}$, equation (6.10) can be expanded as [128]

$$\delta \sim 5\sqrt{\frac{\mu p}{\rho V_{spread}}} \tag{6.12}$$

Next, integrating equation (6.7) using equations (6.8) – (6.11), final form of the expression for the viscous dissipation (for the symmetrical half of the droplet) is obtained as

$$E_{vis} = \frac{\rho}{5}\left(A_1\left(\frac{l}{d}\right)\right)\sqrt{\nu p}\left(V_{spread}\right)^{\frac{3}{2}} \tag{6.13}$$

Where, ν is the kinematic viscosity ($\nu = \frac{\mu}{\rho}$) of the liquid.

From the energy conservation principle, we get

$$KE_i + SE_i = 2\left(KE_{jet} + KE_{spread} + SE_{lg} + SE_{ls} + E_{vis}\right) \tag{6.14}$$

The factor "2" is multiplied in the RHS of equation (6.14) to accommodate for the fact that the energies calculated for the post-impact droplet is for the symmetrical half. Using the expressions for all the components, equation (6.14) can be expressed as

$$\frac{1}{2}\left(\rho V^2\right)\left(\frac{\pi D_d^3}{6}\right) + \pi D_d^2\sigma_{lg} = 2[\alpha\frac{1}{2}\left(\frac{\pi D_d^3}{12}\right)\left(\rho V_{jet}^2\right) + \beta\frac{1}{2}\left(\frac{\pi D_d^3}{12}\right)\left(\rho V_{spread}^2\right) + \left(A_1\left(\frac{l}{d}\right) + A_2\right)\sigma_{lg}$$

$$+ A_1\left(\frac{l}{d}\right)\sigma_{ls} + \frac{\rho}{5}\left(A_1\left(\frac{l}{d}\right)\right)\sqrt{\nu p}\left(V_{spread}\right)^{\frac{3}{2}}] \tag{6.15}$$

Non-dimensionalizing by the initial surface energy, the relationship between the jetting velocity and other parametrs in terms of We, Re, and Ca is obtained as

$$\frac{We}{12} + 1 = \frac{1}{12}\alpha We\left(\frac{V_{jet}}{V}\right)^2 + \beta\frac{1}{12}We\left(\frac{V_{spread}}{V}\right)^2 + 2\left(\frac{A_1}{\pi D_d^2}\frac{l}{d} + \frac{A_2}{\pi D_d^2}\right) + 2\left(\frac{A_1}{\pi D_d^2}\frac{l}{d}\right)\frac{\sigma_{ls}}{\sigma_{lg}} + \frac{2}{5}\left(\frac{A_1}{\pi D_d^2}\frac{l}{d}\right. \tag{6.16}$$

Equation (6.16) can be further rearranged to obtain the expression for V_{jet} as

$$\frac{1}{12}\alpha We\left(\frac{V_{jet}}{V}\right)^2 = \frac{We}{12} + 1 - \beta\left(\frac{1}{12}We\right)\left(\frac{V_{spread}}{V}\right)^2 - 2\left(\frac{A_1}{\pi D_d^2}\frac{l}{d} + \frac{A_2}{\pi D_d^2}\right) - 2\left(\frac{A_1}{\pi D_d^2}\frac{l}{d}\right)\frac{\sigma_{ls}}{\sigma_{lg}} - \frac{2}{5}\left(\frac{A_1}{\pi D_d^2}\right.$$

(6.17)

The transient jetting velocity of the impacted droplet is calculated at various time instants using equation (6.17). We note that values of the correction factors α=0.25 and β =0.2 consistently predict the velocities of all the cases with good accuracy. The instantaneous experimental parameters considered in the model are quantified from image processesing. Experimental values have been used for the transient parameters appearing on the RHS of equation (6.17) required to predict the jet velocity mathematically. Figure 6.14 illustrates the the experimental jet velocities against the model predictions for different impact conditions and groove geometries. It is noted that the proposed analytical model is able to predict the jet velocity of the impacted droplet, except during the initial phase of the jetting dynamics. During the initial phase of droplet impact, the spreading and jetting dynamics is mainly inertia dominated. Whereas, the presented model is based for near equillibrium of forces (inertia, surface and other forces).

6.4 Closure

Experimental post-impact hydrodynamics of water droplets on concave grooves is investigated experimentally in this article. The target grooves have been varied in sizes and surface wettability. The study theoretically discusses the droplet spreading and jetting dynamics in azimuthal and axial directions respectively under different impact conditions. Both the side and top views of the impaction phenomenon have been captured using the high-speed photography. Temporal variation of non-dimensional spreading width, non-dimensional south-pole film thickness and jet velocity are plotted. The findings suggest that, non-dimensional spreading width increases, attains the maximum value, and then decreases with time. The south-pole film thickness of the impacted droplet first decreases up to its minimum value and then again increases due to the recoiling effect. On increasing the curvature of the groove, by changing only one dimension of the groove, the spreading width is found to decrease whereas the opposite is true for film thickness at south-pole. It is because gravity force adversely affects the extension of post-impact droplet on concave surface as the curvature increases. The effect of wettability is also inferred from the morphology of the post-impact droplet. It is observed that trends of spreading width and south pole film thickness coincide for both hydrophilic and superhydrophobic surfaces in the initial phase of spreading but deviate later as strong recoiling effect is the characteristic of non-wetting surfaces (SHS).

Moreover, the present chapter sheds a good insight on jetting hydrodynamics along the axial passage. Such phenomenon is absent on flat surfaces and convex contours. Axial jets gain a high impact velocity at the moment of its generation, but its velocity reduces as the time progresses due to the liquid–liquid cohesive forces and viscous resistance. The jetting velocity is found to increase with the impact We, because a large fraction of the impact kinetic energy gets converted into the jet kinetic energy. It is also observed that, this effect is more prominent in SHS surfaces because these surfaces provide less resistance to the flow of liquid film. Having discussed the impacted droplet morphology and film flow, a theoretical analysis has also been proposed to relate the transient evolution of jet velocity to the governing non-dimensional Weber (We) and capillary (Ca) numbers based on the energy conservation principle. The model predictions are observed to be in good agreement with the experimental data.

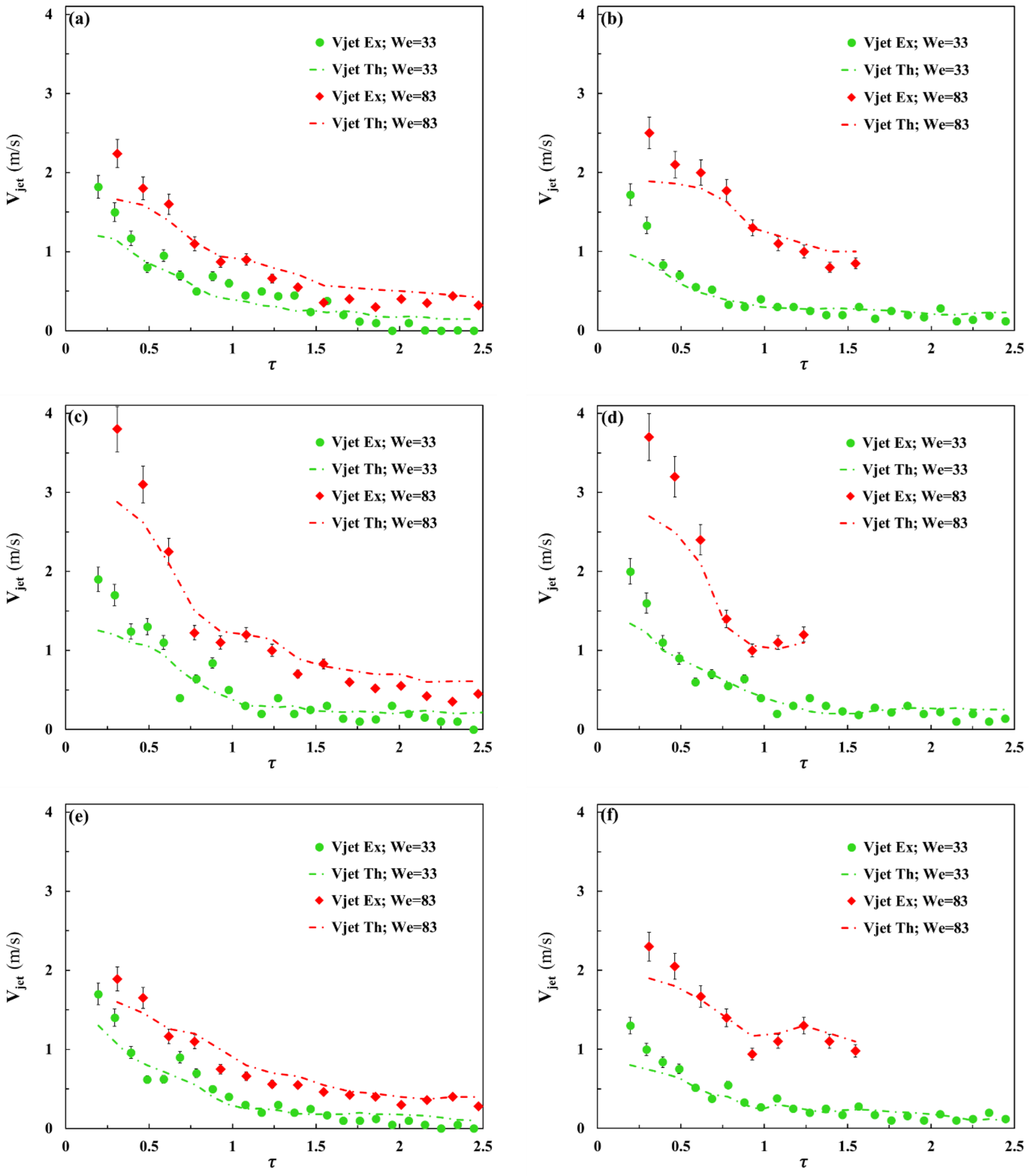

Figure 6.14 Comparison of the experimental (*Ex*) jet velocity against the theoretical (*Th*) predictions for different combinations of the concave grooves and wettability, for (a) $D^* = 2.14$, $H^* = 1.07$, HP (b) $D^* = 2.14$, $H^* =1.07$, SHS (c) $D^* = 1.57$, $H^* = 0.71$, HP (d) $D^* = 1.57$, $H^* = 0.71$, SHS (e) $D^* = 2.14$, $H^* = 0.71$, HP (f) $D^* = 2.14$, $H^* = 0.71$, SHS.

Chapter 7

Conclusions and Scope

7.1 Conclusions

This chapter presents the summary of the studies performed for the present thesis. To conclude the work on spreading and wetting dynamics of droplets on varied non-planar surfaces, all the objectives are discussed as follows. The primary objective of the thesis is covered in the third chapter. To achieve the first objective, numerous experimentations have been performed to find out various dynamical impact outcomes of droplet on cylindrical target surfaces. The impact speed, dimension and wettability of cylindrical surfaces employed are varied. The post-impingement morphology of the droplet has been discussed using dedicated non-dimensional variables, such as the wetting fraction, the spread factor, and the non-dimensional film thickness at the north pole of the target. Experimental observations revel that the wetting fraction and spread factor increase with an increase in the impact Weber number and a decrease in the target-to-drop diameter ratio. An opposite trend is noted for the non-dimensional liquid film thickness at the cylindrical surface's north pole. It is also noted that the spread factor is independent of the target wettability, whereas the wetting fraction is remarkably low for superhydrophobic targets. The post-spreading lamella dynamics has also been observed to be a strong function of the wettability, the impact Weber number, and the diameter ratio, and the same has been explained based on wetting and inertial principles. An analytical expression for temporal evolution of film thickness at the north pole of the cylindrical target is derived from first principles. Moreover, a theoretical model for predicting the maximum wetting fraction for different cylindrical targets in terms of the governing Weber and Capillary number is also proposed.

The next objective of the thesis is covered in chapter four. The second objective focuses on the spreading dynamics of water droplet impinging on spherical target surfaces having dimensions ranging from smaller to larger than the droplet diameter. The post-impact feature study has been conducted on hydrophilic and superhydrophobic spherical surfaces. Effects of the impact Weber number and target-to-drop diameter ratio on the spreading hydrodynamics have been discussed. Post collision dynamics are explored with side and top views of impaction phenomenon using a high-speed imaging technique. The morphological outcome of this impingement process has been quantitatively discussed employing three geometric parameters, namely, liquid film thickness at the north-pole of the target surface, spread factor, and the maximum spread angle. Observations of this chapter revel that, spread factor and the maximum spread angle increases with the decrease in the size of the spherical target, whereas opposite of this is noted for liquid film thickness at the north-pole of the target surface. Temporal variations of liquid film thickness at the north pole of the target have been plotted for numerous cases and found in agreement with the theoretical predictions available in literature. Finally, a mathematical model has been proposed to predict the maximum spread angle on spherical targets.

In the first two objectives, hydrodynamics of droplet impact on two different types of convex surfaces are probed. The focus for further studies is directed towards post-impact hydrodynamics on concave surfaces. In the third objective of the thesis, various impact experiments are conducted and analysed on “V” shaped grooves. The target grooves range in different dimensions and surface wettablities. The groove geometry results in very interesting jetting process along the axial direction. The effect of the impact Weber number on the jet velocity, spreading width, and south-pole liquid film thickness has been studied. Observations suggest that the inertial forces dominate over the surface forces for higher impact Weber number and hence, the effect of wettability is not important. However, the wettability of the substrate plays a significant role for lower Weber number cases, as recoiling phenomenon is observed for the impact on the superhydrophobic substrates. Observations in the relevant chapter (chapter 5) also indicate that the spreading width of the post-impact droplet decreases with the increase in groove steepness. The jetting hydrodynamics has also been probed and instantaneously after the impact, the generated jets travel at high velocity, but quickly reduce to a steady value. Jet velocity is found to increase with an increase in the hydrophobicity of the substrate as well as the impact Weber number. Furthermore, a theoretical formalism has been proposed which predicts the jet velocity at various time instants in terms of the governing Weber and Capillary numbers.

Finally, the last objective of the present thesis is presented in chapter 6. In order to achieve the fourth objective numerous droplet impact experiments have been performed on curved concave surfaces of varying dimensions and surface wettabilities. Post-impact regimes on such concave contours result in very interesting and insightful hydrodynamics. The temporal variations of spreading width, south-pole film thickness and jet velocity have been plotted and probed post-impact. The resulting morphological outcomes of the impingement process on such target surfaces have been discussed along with their effect on various impact conditions. The observations reveal that the role of the wettability of the substrate is more profound in the recoiling stage than in the spreading stage, because inertial forces dominate in the latter. It is also noted that the spreading width increases and south-pole height decreases with increasing the impact Weber number. The opposite trend is noted upon increasing the groove concavity by altering only one dimension of the groove. The jet velocity is found to be the highest immediately after the impact and eventually decreases in a non-linear fashion. Further, it has been noted that the jet velocity increases with increasing the impact Weber number and that its effect is more prominent for superhydrophobic surfaces. Lastly, a semi-analytical frame work has been proposed to predict the jet velocity evolution in terms of governing Weber and capillary numbers.

7.2 Future Scope of the Work

There are some recommendations for the future studies as the following:

- The hydrodynamics of droplet impact on deformable and resilient surfaces is an interesting area of investigation.
- The studies in the thesis shall be performed through simulations in order to investigate the accurate velocity field at various time instants post impact. The computational results shall match and to the experimental results.
- The coalescence of droplets with and without offset on surfaces having different topological features shall be studied in detail to revel interesting outcomes.

7.2 Future Scope of the Work

- The studies in the present thesis shall be extended using other liquid droplets having different thermodynamic properties.

- Droplet impact hydrodynamics shall be probed experimentally and theoretically at the interface point of hydrophilic and superhydrophobic substrates
.

BIBLIOGRAPHY

1. Josserand, C., & Thoroddsen, S. T. (2016). Drop impact on a solid surface. Annual review of fluid mechanics, 48, 365-391.
2. van Dam, D. B., & Le Clerc, C. (2004). Experimental study of the impact of an ink-jet printed droplet on a solid substrate. Physics of Fluids, 16(9), 3403-3414.
3. Haskal, E. I., Buechel, M., Dijksman, J. F., Duineveld, P. C., Meulenkamp, E. A., Mutsaers, C. A. H. A., ... & De Winter, S. H. P. M. (2002, May). 21.1: Ink Jet Printing of Passive‐Matrix Polymer Light Emitting Displays. In SID Symposium Digest of Technical Papers (Vol. 33, No. 1, pp. 776-779). Oxford, UK: Blackwell Publishing Ltd.
4. Li, J., Rossignol, F., & Macdonald, J. (2015). Inkjet printing for biosensor fabrication: combining chemistry and technology for advanced manufacturing. Lab on a Chip, 15(12), 2538-2558.
5. Bolle, L., & Moureau, J. C. (1982). Spray cooling of hot surfaces. Multiphase science and technology, 1(1-4).
6. Wachters, L. H. J., & Westerling, N. A. J. (1966). The heat transfer from a hot wall to impinging water drops in the spheroidal state. Chemical engineering science, 21(11), 1047-1056.
7. Zhao, Z., Poulikakos, D., & Fukai, J. (1996). Heat transfer and fluid dynamics during the collision of a liquid droplet on a substrate—I. Modeling. International Journal of Heat and Mass Transfer, 39(13), 2771-2789.
8. Lan, M., Wang, X., Zhu, P., & Chen, P. (2015). Experimental study on the dynamic process of a water drop with additives impact upon hot liquid fuel surfaces. Energy Procedia, 66, 173-176.
9. Moita, A. S., & Moreira, A. L. N. (2007). Drop impacts onto cold and heated rigid surfaces: morphological comparisons, disintegration limits and secondary atomization. International journal of heat and fluid flow, 28(4), 735-752.
10. Dong, X., Zhu, H., & Yang, X. (2015). Characterization of droplet impact and deposit formation on leaf surfaces. Pest management science, 71(2), 302-308.

11. Massinon, M., De Cock, N., Forster, W. A., Nairn, J. J., McCue, S. W., Zabkiewicz, J. A., & Lebeau, F. (2017). Spray droplet impaction outcomes for different plant species and spray formulations. Crop protection, 99, 65-75.
12. Forster, W. A., Mercer, G. N., & Schou, W. C. (2012). Spray droplet impaction models and their use within AGDISP software to predict retention. New Zealand Plant Protection, 65, 85-92.
13. Wang, D. M., & Watkins, A. P. (1993). Numerical modeling of diesel spray wall impaction phenomena. International Journal of Heat and Fluid Flow, 14(3), 301-312.
14. Ahmadi-Befrui, B., Uchil, N., Gosman, A. D., & Issa, R. I. (1996). Modeling and simulation of thin liquid films formed by spray-wall interaction. SAE transactions, 797-807.
15. Abdulrahman, S. A., Chetehouna, K., Cablé, A., Skreiberg, Ø., & Kadoche, M. (2021). A review on fire suppression by fire sprinklers. Journal of Fire Sciences, 39(6), 512-551.
16. Pan, S., Wang, N., Xiong, D., Deng, Y., & Shi, Y. (2016). Fabrication of superhydrophobic coating via spraying method and its applications in anti-icing and anti-corrosion. Applied Surface Science, 389, 547-553.
17. Lafuma, A., & Quéré, D. (2003). Superhydrophobic states. Nature materials, 2(7), 457-460.
18. Cohen, N., Dotan, A., Dodiuk, H., & Kenig, S. (2016). Superhydrophobic coatings and their durability. Materials and Manufacturing Processes, 31(9), 1143-1155.
19. Bayer, I. S. (2020). Superhydrophobic coatings from ecofriendly materials and processes: a review. Advanced Materials Interfaces, 7(13), 2000095.
20. Yuan, Y., & Lee, T. R. (2013). Contact angle and wetting properties. In Surface science techniques (pp. 3-34). Springer, Berlin, Heidelberg.
21. Snoeijer, J. H., & Andreotti, B. (2008). A microscopic view on contact angle selection. Physics of Fluids, 20(5), 057101.
22. Young, T. (1805). III. An essay on the cohesion of fluids. Philosophical transactions of the royal society of London, (95), 65-87.
23. Li, D., & Neumann, A. W. (1992). Contact angles on hydrophobic solid surfaces and their interpretation. Journal of colloid and interface science, 148(1), 190-200.
24. Gao, L., & McCarthy, T. J. (2006). Contact angle hysteresis explained. Langmuir, 22(14), 6234-6237.

25. Krumpfer, J. W., & McCarthy, T. J. (2010). Contact angle hysteresis: a different view and a trivial recipe for low hysteresis hydrophobic surfaces. Faraday discussions, 146, 103-111.
26. Meiron, T. S., Marmur, A., & Saguy, I. S. (2004). Contact angle measurement on rough surfaces. Journal of colloid and interface science, 274(2), 637-644.
27. Pease, D. C. (1945). The significance of the contact angle in relation to the solid surface. The Journal of Physical Chemistry, 49(2), 107-110.
28. Rioboo, R., Marengo, M., & Tropea, C. (2002). Time evolution of liquid drop impact onto solid, dry surfaces. Experiments in fluids, 33(1), 112-124.
29. Fuller, P. W. W. (2009). An introduction to high speed photography and photonics. The Imaging Science Journal, 57(6), 293-302.
30. Rein, M. (1995). Wave phenomena during droplet impact. In IUTAM symposium on waves in liquid/gas and liquid/vapour two-phase systems (pp. 171-190). Springer, Dordrecht.
31. Crooks, R., Cooper-White, J., & Boger, D. V. (2001). The role of dynamic surface tension and elasticity on the dynamics of drop impact. Chemical Engineering Science, 56(19), 5575-5592.
32. Chandra Park, H., Carr, W. W., Zhu, J., & Morris, J. F. (2003). Single drop impaction on a solid surface. AIChE journal, 49(10), 2461-2471.
33. Marengo, M., Antonini, C., Roisman, I. V., & Tropea, C. (2011). Drop collisions with simple and complex surfaces. Current Opinion in Colloid & Interface Science, 16(4), 292-302.
34. Kim, J. (2007). Spray cooling heat transfer: The state of the art. International Journal of Heat and Fluid Flow, 28(4), 753-767.
35. Wang, Z., Lopez, C., Hirsa, A., & Koratkar, N. (2007). Impact dynamics and rebound of water droplets on superhydrophobic carbon nanotube arrays. Applied physics letters, 91(2), 023105.
36. Jung, Y. C., & Bhushan, B. (2008). Dynamic effects of bouncing water droplets on superhydrophobic surfaces. Langmuir, 24(12), 6262-6269.
37. Khojasteh, D., Kazerooni, M., Salarian, S., & Kamali, R. (2016). Droplet impact on superhydrophobic surfaces: A review of recent developments. Journal of industrial and engineering chemistry, 42, 1-14.
38. Antonini, C., Amirfazli, A., & Marengo, M. (2012). Drop impact and wettability: From hydrophilic to superhydrophobic surfaces. Physics of fluids, 24(10), 102104.

39. Yarin, A. L. (2006). Drop impact dynamics: splashing, spreading, receding, bouncing…. Annu. Rev. Fluid Mech., 38, 159-192.
40. Werner, S. R., Jones, J. R., Paterson, A. H., Archer, R. H., & Pearce, D. L. (2007). Droplet impact and spreading: Droplet formulation effects. Chemical Engineering Science, 62(9), 2336-2345.
41. Rein, M. (1993). Phenomena of liquid drop impact on solid and liquid surfaces. Fluid dynamics research, 12(2), 61-93.
42. Heidari, E., Daeichian, A., Sobati, M. A., & Movahedirad, S. (2020). Prediction of the droplet spreading dynamics on a solid substrate at irregular sampling intervals: Nonlinear Auto-Regressive exogenous Artificial Neural Network approach (NARX-ANN). Chemical Engineering Research and Design, 156, 263-272.
43. Cecchetto, B. T. (2010). Nonlinear blood pattern reconstruction (Doctoral dissertation, University of British Columbia).
44. Pawar, S. K., Henrikson, F., Finotello, G., Padding, J. T., Deen, N. G., Jongsma, A., ... & Kuipers, J. H. (2016). An experimental study of droplet-particle collisions. Powder Technology, 300, 157-163.
45. Roux, D. C. D., & Cooper-White, J. J. (2004). Dynamics of water spreading on a glass surface. Journal of colloid and interface science, 277(2), 424-436.
46. Clanet, C., Béguin, C., Richard, D., & Quéré, D. (2004). Maximal deformation of an impacting drop. Journal of Fluid Mechanics, 517, 199-208.
47. Worthington, A. M. (1877). XXVIII. On the forms assumed by drops of liquids falling vertically on a horizontal plate. Proceedings of the royal society of London, 25(171-178), 261-272.
48. Ueda, T., Enomoto, T., & Kanetsuki, M. (1979). Heat transfer characteristics and dynamic behavior of saturated droplets impinging on a heated vertical surface. Bulletin of JSME, 22(167), 724-732.
49. Fujimoto, H., & Hatta, N. (1996). Deformation and rebounding processes of a water droplet impinging on a flat surface above Leidenfrost temperature.
50. Strotos, G., Gavaises, M., Theodorakakos, A., & Bergeles, G. (2008). Numerical investigation of the cooling effectiveness of a droplet impinging on a heated surface. International Journal of Heat and Mass Transfer, 51(19-20), 4728-4742.
51. Ma, T., Feng, L., Wang, H., Liu, H., & Yao, M. (2017). A numerical study of spray/wall impingement based on droplet impact phenomenon. International Journal of Heat and Mass Transfer, 112, 401-412.

52. Kim, H. Y., & Chun, J. H. (2001). The recoiling of liquid droplets upon collision with solid surfaces. Physics of fluids, 13(3), 643-659.
53. Aziz, S. D., & Chandra, S. (2000). Impact, recoil and splashing of molten metal droplets. International journal of heat and mass transfer, 43(16), 2841-2857.
54. Bejan, A., & Gobin, D. (2006). Constructal theory of droplet impact geometry. International journal of heat and mass transfer, 49(15-16), 2412-2419.
55. Roisman, I. V., Rioboo, R., & Tropea, C. (2002). Normal impact of a liquid drop on a dry surface: model for spreading and receding. Proceedings of the Royal Society of London. Series A: Mathematical, Physical and Engineering Sciences, 458(2022), 1411-1430.
56. Ukiwe, C., & Kwok, D. Y. (2005). On the maximum spreading diameter of impacting droplets on well-prepared solid surfaces. Langmuir, 21(2), 666-673.
57. Scheller, B. L., & Bousfield, D. W. (1995). Newtonian drop impact with a solid surface. AIChE Journal, 41(6), 1357-1367.
58. Cui, J., Chen, X., Wang, F., Gong, X., & Yu, Z. (2009). Study of liquid droplets impact on dry inclined surface. Asia‐Pacific Journal of Chemical Engineering, 4(5), 643-648.
59. Fukai, J., Shiiba, Y., Yamamoto, T., Miyatake, O., Poulikakos, D., Megaridis, C. M., & Zhao, Z. (1995). Wetting effects on the spreading of a liquid droplet colliding with a flat surface: experiment and modeling. Physics of fluids, 7(2), 236-247.
60. Chandra, S., & Avedisian, C. T. (1991). On the collision of a droplet with a solid surface. Proceedings of the Royal Society of London. Series A: Mathematical and Physical Sciences, 432(1884), 13-41.
61. Pasandideh‐Fard, M., Qiao, Y. M., Chandra, S., & Mostaghimi, J. (1996). Capillary effects during droplet impact on a solid surface. Physics of fluids, 8(3), 650-659.
62. Mao, T., Kuhn, D. C., & Tran, H. (1997). Spread and rebound of liquid droplets upon impact on flat surfaces. AIChE Journal, 43(9), 2169-2179.
63. Richard, D., Clanet, C., & Quéré, D. (2002). Contact time of a bouncing drop. Nature, 417(6891), 811-811.
64. Bartolo, D., Josserand, C., & Bonn, D. (2005). Retraction dynamics of aqueous drops upon impact on non-wetting surfaces. Journal of Fluid Mechanics, 545, 329-338.
65. Gatne, K. P., Jog, M. A., & Manglik, R. M. (2009). Surfactant-induced modification of low Weber number droplet impact dynamics. Langmuir, 25(14), 8122-8130.

66. Wang, X., Chen, L., & Bonaccurso, E. (2015). Comparison of spontaneous wetting and drop impact dynamics of aqueous surfactant solutions on hydrophobic polypropylene surfaces: scaling of the contact radius. Colloid and Polymer Science, 293(1), 257-265.
67. Lin, S., Zhao, B., Zou, S., Guo, J., Wei, Z., & Chen, L. (2018). Impact of viscous droplets on different wettable surfaces: Impact phenomena, the maximum spreading factor, spreading time and post-impact oscillation. Journal of colloid and interface science, 516, 86-97.
68. Latka, A., Boelens, A. M., Nagel, S. R., & de Pablo, J. J. (2018). Drop splashing is independent of substrate wetting. Physics of Fluids, 30(2), 022105.
69. Riboux, G., & Gordillo, J. M. (2014). Experiments of drops impacting a smooth solid surface: a model of the critical impact speed for drop splashing. Physical review letters, 113(2), 024507.
70. Murshed, S. M., & Nieto de Castro, C. A. (2011). Spreading characteristics of nanofluid droplets impacting onto a solid surface. Journal of Nanoscience and Nanotechnology, 11(4), 3427-3433.
71. Prasad, G. V. V., Dhar, P., & Samanta, D. (2022). Postponement of dynamic Leidenfrost phenomenon during droplet impact of surfactant solutions. International Journal of Heat and Mass Transfer, 189, 122675.
72. Dhar, P., Mishra, S. R., Gairola, A., & Samanta, D. (2020). Delayed Leidenfrost phenomenon during impact of elastic fluid droplets. Proceedings of the Royal Society A, 476(2243), 20200556.
73. Sarojini KG, Kalpana, Purbarun Dhar, Susy Varughese, and Sarit K. Das. "Coalescence dynamics of PEDOT: PSS droplets impacting at offset on substrates for inkjet printing." Langmuir 32, no. 23 (2016): 5838-5851.
74. Lafuma, A., & Quéré, D. (2003). Superhydrophobic states. Nature materials, 2(7), 457-460.
75. Latorrata, S., Stampino, P. G., Cristiani, C., & Dotelli, G. (2014). Novel superhydrophobic microporous layers for enhanced performance and efficient water management in PEM fuel cells. International journal of hydrogen energy, 39(10), 5350-5357.
76. Zhang, F., Zhao, L., Chen, H., Xu, S., Evans, D. G., & Duan, X. (2008). Corrosion resistance of superhydrophobic layered double hydroxide films on aluminum. Angewandte Chemie, 120(13), 2500-2503.

77. Hooda, A., Goyat, M. S., Pandey, J. K., Kumar, A., & Gupta, R. (2020). A review on fundamentals, constraints and fabrication techniques of superhydrophobic coatings. Progress in Organic Coatings, 142, 105557.
78. Vazirinasab, E., Jafari, R., & Momen, G. (2018). Application of superhydrophobic coatings as a corrosion barrier: A review. Surface and Coatings Technology, 341, 40-56.
79. Lin, Y., Chen, H., Wang, G., & Liu, A. (2018). Recent progress in preparation and anti-icing applications of superhydrophobic coatings. Coatings, 8(6), 208.
80. Wenzel, R. N. (1936). Resistance of solid surfaces to wetting by water. Industrial & Engineering Chemistry, 28(8), 988-994.
81. Cassie, A. B. D., & Baxter, S. (1944). Wettability of porous surfaces. Transactions of the Faraday society, 40, 546-551.
82. Zhang, P., & Lv, F. Y. (2015). A review of the recent advances in superhydrophobic surfaces and the emerging energy-related applications. Energy, 82, 1068-1087.
83. Li, X., Ma, X., & Lan, Z. (2010). Dynamic behavior of the water droplet impact on a textured hydrophobic/superhydrophobic surface: The effect of the remaining liquid film arising on the pillars' tops on the contact time. Langmuir, 26(7), 4831-4838.
84. LeClear, S., LeClear, J., Park, K. C., & Choi, W. (2016). Drop impact on inclined superhydrophobic surfaces. Journal of colloid and interface science, 461, 114-121.
85. Liu, Y., Whyman, G., Bormashenko, E., Hao, C., & Wang, Z. (2015). Controlling drop bouncing using surfaces with gradient features. Applied Physics Letters, 107(5), 051604.
86. Sung, Y. H., Kim, Y. D., Choi, H. J., Shin, R., Kang, S., & Lee, H. (2015). Fabrication of superhydrophobic surfaces with nano-in-micro structures using UV-nanoimprint lithography and thermal shrinkage films. Applied Surface Science, 349, 169-173.
87. Kim, H., Lee, C., Kim, M. H., & Kim, J. (2012). Drop impact characteristics and structure effects of hydrophobic surfaces with micro-and/or nanoscaled structures. Langmuir, 28(30), 11250-11257.
88. Richard, D., & Quéré, D. (2000). Bouncing water drops. EPL (Europhysics Letters), 50(6), 769.
89. Yun, S. (2017). Bouncing of an ellipsoidal drop on a superhydrophobic surface. Scientific reports, 7(1), 1-9.

90. Murugadoss, K., Dhar, P., & Das, S. K. (2017). Role and significance of wetting pressures during droplet impact on structured superhydrophobic surfaces. The European Physical Journal E, 40(1), 1-10.
91. Chen, Y., & Lian, Y. (2018). Numerical investigation of coalescence-induced self-propelled behavior of droplets on non-wetting surfaces. Physics of Fluids, 30(11), 112102.
92. Sahoo, N., Khurana, G., Harikrishnan, A. R., Samanta, D., & Dhar, P. (2020). Post impact droplet hydrodynamics on inclined planes of variant wettabilities. European Journal of Mechanics-B/Fluids, 79, 27-37.
93. Pasandideh-Fard, M., Bussmann, M., & Chandra, S. (2001). Simulating droplet impact on a substrate of arbitrary shape. Atomization and sprays, 11(4).
94. Hardalupas, Y., Taylor, A. M. K. P., & Wilkins, J. H. (1999). Experimental investigation of sub-millimetre droplet impingement on to spherical surfaces. International journal of heat and fluid flow, 20(5), 477-485.
95. Bakshi, S., Roisman, I. V., & Tropea, C. (2007). Investigations on the impact of a drop onto a small spherical target. Physics of fluids, 19(3), 032102.
96. Mitra, S., Sathe, M. J., Doroodchi, E., Utikar, R., Shah, M. K., Pareek, V., ... & Evans, G. M. (2013). Droplet impact dynamics on a spherical particle. Chemical Engineering Science, 100, 105-119.
97. Banitabaei, S. A., & Amirfazli, A. (2017). Droplet impact onto a solid sphere: Effect of wettability and impact velocity. Physics of Fluids, 29(6), 062111.
98. Dalgamoni, H. N., & Yong, X. (2021). Numerical and theoretical modeling of droplet impact on spherical surfaces. Physics of Fluids, 33(5), 052112.
99. Hung, L. S., & Yao, S. C. (1999). Experimental investigation of the impaction of water droplets on cylindrical objects. International journal of multiphase flow, 25(8), 1545-1559.
100. Sher, E., Haim, L. F., & Sher, I. (2013). Off-centered impact of water droplets on a thin horizontal wire. International Journal of Multiphase Flow, 54, 55-60.
101. Jin, Z., Zhang, H., & Yang, Z. (2017). The impact and freezing processes of a water droplet on different cold cylindrical surfaces. International Journal of Heat and Mass Transfer, 113, 318-323.

102. Liu, X., Zhao, Y., Chen, S., Shen, S., & Zhao, X. (2017). Numerical research on the dynamic characteristics of a droplet impacting a hydrophobic tube. Physics of fluids, 29(6), 062105.

103. Lorenceau, E., & Quéré, D. (2004). Drops on a conical wire. Journal of Fluid Mechanics, 510, 29-45.

104. Rajesh, R. S., Naveen, P. T., Krishnakumar, K., & Ranjith, S. K. (2019). Dynamics of single droplet impact on cylindrically-curved superheated surfaces. Experimental Thermal and Fluid Science, 101, 251-262.

105. Mishra, S. R., Samanta, D., & Dhar, P. (2021). Elasto-hydrodynamics of non-Newtonian droplet collision with convex substrates. Physics of Fluids, 33(8), 082106.

106. Duursma, G., Sefiane, K., & Kennedy, A. (2009). Experimental studies of nanofluid droplets in spray cooling. Heat Transfer Engineering, 30(13), 1108-1120.

107. Fathi, S., Dickens, P., & Fouchal, F. (2010). Regimes of droplet train impact on a moving surface in an additive manufacturing process. Journal of Materials Processing Technology, 210(3), 550-559.

108. Rashid, T., Khawaja, H. A., & Edvardsen, K. (2016). Review of marine icing and anti-/de-icing systems. Journal of marine engineering & technology, 15(2), 79-87.

109. Li, Q., Chai, Z., Shi, B., & Liang, H. (2014). Deformation and breakup of a liquid droplet past a solid circular cylinder: A lattice Boltzmann study. Physical Review E, 90(4), 043015.

110. Shen, S., Bi, F., & Guo, Y. (2012). Simulation of droplets impact on curved surfaces with lattice Boltzmann method. International journal of heat and mass transfer, 55(23-24), 6938-6943.

111. Harikrishnan, A. R., Dhar, P., Agnihotri, P. K., Gedupudi, S., & Das, S. K. (2018). Correlating contact line capillarity and dynamic contact angle hysteresis in surfactant-nanoparticle based complex fluids. Physics of Fluids, 30(4), 042006.

112. Rubio, C., Costa, D., Bellon-Fontaine, M. N., Relkin, P., Pradier, C. M., & Marcus, P. (2002). Characterization of bovine serum albumin adsorption on chromium and AISI 304 stainless steel, consequences for the Pseudomonas fragi K1 adhesion. Colloids and Surfaces B: Biointerfaces, 24(3-4), 193-205.

113. Mitra, S., Nguyen, T. B. T., Doroodchi, E., Pareek, V., Joshi, J. B., & Evans, G. M. (2016). On wetting characteristics of droplet on a spherical particle in film boiling regime. Chemical Engineering Science, 149, 181-203.

114. Ku Shaari, K. Z. (2007). Coating uniformity on a pharmaceutical tablet: An experimental study and finite volume modeling of droplet impact behavior.

115. Christodoulou, C., Sorensen, E., García-Muñoz, S., & Mazzei, L. (2020). Mathematical modeling of spray impingement and film formation on pharmaceutical tablets during coating. Chemical Engineering Research and Design, 153, 768-788.

116. Link, K. C., & Schlünder, E. U. (1997). Fluidized bed spray granulation: Investigation of the coating process on a single sphere. Chemical Engineering and Processing: Process Intensification, 36(6), 443-457.

117. El-Kader, A., & Abu Hashish, H. (2020). Encapsulation techniques of food bioproduct. Egyptian Journal of Chemistry, 63(5), 1881-1909.

118. Chen, S., & Bertola, V. (2017). Drop impact on spherical soft surfaces. Physics of Fluids, 29(8), 082106.

119. Wohlfarth, C. (2008). Surface tension of butyl acetate. Landolt Börnstein, 24, 177.

120. https://www.dow.com/assets/attachments/business/pcm/solvents/methyl_isobutyl_ketone/tds/methyl_isobutyl_ketone.pdf

121. https://www.technibond.co.uk/Portals/0/blog-img/surface-energy-chart.pdf

122. Bolle, L., & Moureau, J. C. (1982). Spray cooling of hot surfaces. Multiphase science and technology, 1(1-4).

123. Jowkar, S., & Morad, M. R. (2019). Rebounding suppression of droplet impact on hot surfaces: effect of surface temperature and concaveness. Soft Matter, 15(5), 1017-1026.

124. Lad, V. N. (2017). Dynamics of spreading of impinged droplets on the curved-grooved surface. Journal of the Brazilian Society of Mechanical Sciences and Engineering, 39(10), 3911-3918.

125. Attané, P., Girard, F., & Morin, V. (2007). An energy balance approach of the dynamics of drop impact on a solid surface. Physics of Fluids, 19(1), 012101.

126. Akao, F., Araki, K., Mori, S., & Moriyama, A. (1980). Deformation behaviors of a liquid droplet impinging onto hot metal surface. Transactions of the Iron and Steel Institute of Japan, 20(11), 737-743.

127. Guo, C., Sun, Y., & Zhao, D. (2021). Experimental study of droplet impact on superheated cylindrical surfaces. Experimental Thermal and Fluid Science, 121, 110263.

128. Moreira, A. L. N., Moita, A. S., & Panao, M. R. (2010). Advances and challenges in explaining fuel spray impingement: How much of single droplet impact research is useful?. Progress in energy and combustion science, 36(5), 554-580.

129. Bolleddula, D. A., Berchielli, A., & Aliseda, A. (2010). Impact of a heterogeneous liquid droplet on a dry surface: Application to the pharmaceutical industry. Advances in colloid and interface science, 159(2), 144-159.

Biodata

BIODATA

- **Name:** **Gargi Khurana**

- **Date of Birth:** **18th June 1994**

- **Education:**
  - **Direct PhD** **2022**
    Indian Institute of Technology Ropar, Punjab, India
  - **B. Tech Honours (Mechanical Engineering)** **2016**
    UIET, Panjab University, Chandigarh, India

- **PhD Dissertation:** Droplet Impact Hydrodynamics on Curved Surfaces
  Advisors: **Dr. Purbarun Dhar and Dr. Devranjan Samanta**

DOCTORAL COMMITTEE

Chairman: **Dr. Navin Kumar**

Professor, Department of Mechanical Engineering, IIT Ropar

Supervisor(s): **Dr. Purbarun Dhar**

Assistant Professor, Department of Mechanical Engineering, IIT Kharagpur

Dr. Devranjan Samanta

Assistant Professor, Department of Mechanical Engineering, IIT Ropar

Member(s): **Dr. Himanshu Tyagi**

Associate Professor, Department of Mechanical Engineering, IIT Ropar

Dr. Rakesh Kumar Maurya

Associate Professor, Department of Mechanical Engineering, IIT Ropar

Dr. Subash Chandra Martha

Associate Professor, Department of Mathematics, IIT Ropar